Reversibly Reconfigurable Plasmonic Nanomaterials

Soumyadyuti Samai

A dissertation

submitted in partial fulfillment of the

requirements for the degree of

Doctor of Philosophy

University of Washington

2017

Reading Committee:

David S. Ginger, Chair
David J. Masiello
Lutz Maibaum

Program Authorized to Offer Degree:

Chemistry

University of Washington

Abstract

Reversibly Reconfigurable Plasmonic Nanomaterials

Soumyadyuti Samai

Chair of the Supervisory Committee:
Professor David S. Ginger
Department of Chemistry

Plasmonic nanoparticles have been extensively investigated in various fields, ranging from biosensing to nanophotonics, due to their characteristic optical features arising from localized surface plasmon resonance. A number of efforts have been made to tailor the optical properties of the nanoparticles by controlling their shape, size and chemical compositions that have advanced their applications in catalysis, molecular diagnostics, therapeutics, and designing electronic devices. Optical signatures of plasmonic nanoparticle assemblies depend on the near field coupling between the plasmon modes of the constituent particles that can be modulated by the distance and orientation between the particles. While the first-generation of plasmonic nanomaterials attempts to control the distance and directionality of the interparticle coupling by employing chemical reagents, recent developments to introduce stimulus-responsivity in the nanomaterials provide us opportunities to control the functional and optical properties of the such materials with external reagents such as light, heat, pH, electric field etc. These emerging plasmonic nanomaterials allow reversible reconfiguration of the structure that can be manipulated remotely, in a reagent-free manner, allowing reusability of the materials in all the applications.

Such reconfigurable nanomaterials are obtained by combining the plasmonic nanoparticles with stimulus-sensitive materials. In this dissertation, I explore the use of photo-

responsive DNA and thermo-responsive polymer poly(N-isopropylacrylamide) (PNIPAM) hydrogels, to construct reconfigurable assembly of plasmonic nanoparticles and characterize the reversible change in their optical properties in response to external stimuli.

DNA has been a powerful material in nanotechnology for engineering 3D plasmonic structures, plasmon rulers and chiral nanophotonic elements. Not only the length and structural conformations of the DNA allow a precise tuning of interparticle distance and geometry of the nanostructures, but also it matches with the decay length of the near-field plasmon coupling. Recent advents of the azobenzene-phosphoramidite chemistry have facilitated the design of photo-responsive nanomaterials assembly, where the structural reconfiguration and the optical properties are controlled by the reversible *trans*-to-*cis* azobenzene photoisomerization. Such nanomaterials have found potential applications in low-cost, remote plasmonic biosensing, and optically active nanodevices.

The functionality of such optically reconfigurable nanomaterials is extremely sensitive to efficiency of azobenzene photoisomerization in the DNA sequences. So, in chapter 3, we study the *trans*-to-*cis* photoisomerization of azobenzene-modified DNAs by measuring the photoisomerization quantum yields in different DNA sequences at various temperatures. Notably we provide the first report that the quantum yields of photoisomerization of azobenzene incorporated to a DNA phosphate backbone is temperature-sensitive and the temperature-dependent behavior is related to the host DNA sequence and its melting temperature. This result is unique in the sense that this behavior is distinct from the photoisomerization of free azobenzene in solution, which is independent of temperature. We also examined the effect of DNA sequences on the *cis*-to-*trans* reverse thermal isomerization of azobenzene. Our results indicate that the reverse thermal isomerization process is not affected by the DNA sequences and

follows first order kinetics with an Arrhenius activation energy similar to that of the free azobenzene in solution. These findings provide effective design principles for engineering more efficient photo-reconfigurable plasmonic nanomaterials using azobenzene-modified DNAs.

Next, in chapter 4 we demonstrate the assembly of photoswitchable gold nanoparticle dimers using an azobenzene-modified hairpin DNA linker and optically characterize their optical reconfiguration upon reversible photoisomerization of azobenzene. The *trans*-to-*cis* azobenzene photoconversion upon UV light exposure leads to the unzipping of the hairpin DNA that increases the separation between the two nanoparticles. Blue light illumination reforms the hairpin structure and restores the closed form of the dimer. The light-induced reconfiguration of the interparticle distances is reflected in the reversible plasmonic shift of the dimer scattering spectra measured by single particle dark field spectroscopy over multiple cycles of UV and blue light exposure. Our results significantly contribute to the fundamental understanding of the dynamical optical and structural properties of the DNA-linked gold nanoparticle dimers and lay the ground work for using them as building blocks in the future plasmonic nanomaterials.

Finally, in chapter 5, we assemble and characterize novel reconfigurable hybrid nanocomposite materials that combines the optical properties of plate-like anisotropic silver nanoprisms with thermally responsive PNIPAM microgels. We find that these composites exhibit large thermochromic shifts upon the reversible volume-phase transition of PNIPAM that results in an easily observed color switching of the solution with temperature cycling. We also show that both the nanoprism size and loading density on the microgel can be used to independently tailor the thermo-responsive optical properties of the composites in the visible and NIR region of the spectra. The hybrid microgels exhibit a strong, reversible change and high contrast in NIR scattering intensity, achieved by the thermally reversible modulation of the

interparticle distance and near-field plasmonic coupling upon swelling-deswelling of the PNIPAM microgels. These results create opportunities to use the novel plasmonic materials in designing thermochromic sensors, NIR labels for imaging and smart materials for nanophotonics applications.

TABLE OF CONTENTS

LIST OF FIGURES

LIST OF TABLES

ACKNOWLEDGEMENTS

I am indebted to many people for their help, support, and guidance throughout the years. First and foremost, I would like to thank my parents, Nanda Samai and Sudeshna Samai, for their constant love and support from 7000 miles away, my older sister Poulami Samai, who has been a great inspiration to me since my childhood, and my brother-in-law, Paul Smith, for encouraging me to apply to the Chemistry graduate program in the University of Washington. I would also like to thank my close relatives and my friends in India. None of this would have been possible without their love and support.

I would like to express my deepest acknowledgment to my supervisor, Prof. David S. Ginger, whose expertise, guidance, patience, and generous support have contributed to my development as a scientist during my PhD. Thank you for being such a great advisor. I could not have achieved what I have covered in the dissertation without your support. Along with my advisor, I would like to thank my graduate supervisory committee members and collaborators throughout the years, Lutz Maibaum, David J. Masiello, Sarah L. Keller and Charles T. Campbell for their valuable suggestions, feedback and guidance in my research. I am also grateful to my undergraduate professors Samrajnee Dutta, Achintya K. Sarkar, Dipak K. Mandal, Pradipta Ghosh, from Presidency College, and Srihari Keshavamurthy, Nishanth N. Nair from IIT Kanpur for inspiring me to pursue research career in Chemistry. I feel blessed to have so many great teachers in my life.

I want to thank the current and some former members of the Ginger lab for being great co-workers. Thanks to Dr. Yunqi Yan and Dr. Zhaoxia Qian for being such great mentors to me. Thanks to Dr. Esha Sengupta and Dr. Jie Zhang for their thoughtful suggestions and discussions on azobenzene-modified DNAs. Special thanks to Dane deQuilettes, Sarah Vorpahl, Mark Ziffer,

Lucas Flagg, Phillip Cox, Adam Colbert, Katie Guye, Jessica Kong, Erin Jedlicka, Jake Precht, Giles Eperon, Rajiv Giridharagopal, David Moreman, Sarthak Jariwala, Demi Liu, Wenbi Wu, Susanne Koch, Susanne Birkhold, Sven Burke and Tony Wu, for creating a friendly and supportive atmosphere in the lab. It has been a pleasure to work with so many great researchers that has made my graduate school experience so wonderful.

Throughout my PhD, I got the opportunity to mentor undergraduate researchers, Tina Lok Yee Choi and Dakoda J. Bradley, who have contributed greatly to my development as a mentor and researcher. Their thoughtful scientific questions and hard work in lab have helped me to accomplish a fast and more successful completion of the research projects presented in the thesis. I would like to thank Addie Kingsland from Prof. Lutz Maibaum's group for all the discussions that have helped me further understand the local-volume dependence of azobenzene photoisomerization mechanism that we discuss in chapter 3. I am also grateful to my collaborators Jorge Chavez Benavides and Nancy Kelley-Loughnane, from Air Force Research Lab, for their time and critical contributions in studying the photo-triggered binding-unbinding events of the azobenzene-modified DNA aptamer sequences to its target.

I am thankful to all my wonderful friends for their constant care and tremendous support throughout my time here in the PhD program, and for being a family to me in Seattle. Additionally, I would like to thank all the staff members in the Department of Chemistry for all their support and assistance throughout the years. I would like to acknowledge AFOSR for funding my research projects.

Finally, I would like to dedicate this thesis to my grandfather, Sushil K. Parui, who is 90 years old and has not been doing well lately. He has always been very curious and excited about

my education and research in science. I am grateful for all your blessings and good wishes in my life. I hope you live a wonderful rest of your life and I will see you soon.

Chapter 1. INTRODUCTION

The work presented in this thesis explores the assembly and characterization of the structural, optical, and plasmonic properties of stimuli-responsive reconfigurable plasmonic nanomaterials using azobenzene-modified photoswitchable nucleic acids and thermo-responsive polymer poly(N-isopropylacrylamide) or PNIPAM microgels. In this chapter, the plasmonic properties of metal nanoparticles and their assemblies are discussed briefly, followed by an overview of recent developments of stimuli-responsive reconfigurable plasmonic nanomaterials highlighting some examples of their unique optical properties and applications in various fields.

1.1 PLASMONIC NANOPARTICLES AND THEIR ASSEMBLIES

Metal nanoparticles like gold and silver have contributed immensely to the development of a wide range of fields, starting from biosensing,[1,2] and imaging[3,4] to energy harvesting[5-7] and catalysis,[8,9] due to their unique interaction with electromagnetic radiation and the ability to form localized surface plasmons.[10,11] The conduction electrons on the surface of the metal nanoparticles collectively oscillate in response to the electric field of the light of wavelength exceeding their dimensions. Localized surface plasmon resonance (LSPR) occurs at a certain wavelength of the incident light, which creates an intense electromagnetic field confined to the surface of the particle and results in strong optical absorption and optical scattering properties. The resonant coupling with the incident light occurs in the visible region for most of the spherical metal nanoparticles. The plasmon resonance frequency can be tuned by changing the shape, size, and the composition of the nanoparticles. Nanoparticles with anisotropic shapes generate several plasmon resonance modes that show a dependence on the polarization of incident light.[12-17] The localized surface

plasmon resonance of the nanoparticles is also very sensitive to the refractive index of surrounding medium, which makes them particularly useful for molecular binding and sensing applications.

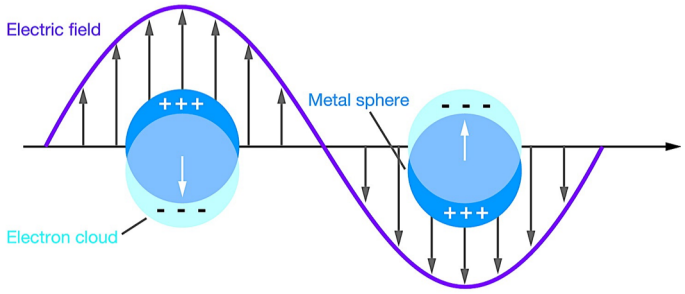

Figure 1.1 Surface Plasmon Resonance in Metal Nanoparticles**.** The free metal electrons collectively oscillate coupled with the electric field of the incident light of a specific wavelength (Image is reprinted with permission of reference 10).

In an assembly of nanoparticles, plasmon modes of different particles interact with each other, which leads to the splitting of the plasmon resonance peaks.[18,19] The extent of near-field plasmon coupling, and thus the relative intensity and the positions of the plasmon peaks in the nanomaterials assembly can be controlled by the shape, size, symmetry, and the interparticle separation between the nanoparticles. Recent advancements in the theoretical studies allow us to analyze these complex plasmon resonance modes by treating the interparticle plasmon coupling as a mixing between the plasmons on adjacent nanoparticles, like the hybridization of electronic wave functions in atomic and molecular orbital formation.[20-23]

Significant progress has been made to develop new chemical syntheses and growth methods for nanoparticles to create multiparticle assemblies of different geometries and tailor their structural and optical responses. This advancement in the colloidal chemistry has opened the door to employ these artificial architectures in various applications such as nanophotonics,[24,25] catalysis[26,27] and sensing.[28-31]. For example, strong absorption and light scattering properties of these nanomaterials, which are highly sensitive to a small change in the configuration at a length

scale comparable to structural changes in biological systems, gives them an advantage for optical detection of nucleic acid, proteins and other small biomolecules via label-free sensing.[31-33] The near-field coupling in these nanostructures also forms local electromagnetic hot spots at the junction of the nanoparticles, which increases the surface-enhanced Raman scattering (SERS) efficiency by several orders of magnitude, making it sufficient for single molecule detection[34-37] as well as super resolution imaging.[38] Due to the enhanced local electromagnetic field intensities these nanomaterials are often used to enhance the performance and efficiency of solar energy materials.[39,40]

In recent years, a considerable amount of research has been done to design plasmonic nanomaterials that allow a reconfigurable change in their structure and optical signatures by reversibly tuning the interparticle distances and plasmon coupling in these nanomaterials with the help of external stimuli, and thus, enables recycling and reusability of the materials in the above-mentioned applications. In the following section, we discuss on some emerging examples of these next-generation plasmonic nanomaterials in the context of this dissertation.

1.2 STIMULI-RESPONSIVE NANOMATERIALS

Reconfigurable plasmonic nanomaterials integrate the unique optical properties of the plasmonic nanoparticles with stimuli-responsivity of some molecules that undergo reversible change in their structural conformation in response to the change in the external reagents, such as chemicals, light, heat, electric field, pH etc. Such responsive components are used to assemble the nanoparticles either as molecular linkers or as three-dimensional scaffolds, such that, when the responsive material switches between the two different conformational states, triggered by the external stimuli, it alters the orientation and the separation between the attached nanoparticles and

thus, modifies the plasmonic and optical responses of the nanomaterials, which then goes back to the initial state in absence of the stimuli.

Among various responsive molecules, nucleic acids are extensively used for designing reconfigurable nanomaterials of well-defined geometry, because of its molecular recognition and unique structural features.[41-45] For example, Zhang al.[46] have shown the formation of core-satellite nanostructures where they assembled gold nanoparticles of different sizes through the hybridization between complementary DNA sequences. Thermal dehybridization of the linker DNAs allows a reversible dissociation and recovery of the nanostructure, making them potentially useful for sensing applications. On the other hand, Maye et al.[47] have employed DNA sequences to engineer super lattices and dimer clusters of spherical gold nanoparticles that show a transition between two rigid structures through a compressible intermediate state, by changing the interparticle linker from rigid dsDNA to flexible ssDNA. Even though most of these DNA linked plasmonic materials involve assembly of spherical gold nanoparticles, recently, gold nanords have also been explored to build anisotropic nanostructures. For instance, Kuzyk et al.[48] have constructed chiral plasmonic nanomaterials by assembling two gold nanorods (AuNR) on a DNA origami template, and achieved conformation switching of the structures between two different chiral states by employing specific ssDNA sequences, whereas Zhan et al.[49] have fabricated reconfigurable three-dimensional plasmonic nanostructures consisting of three gold nanorods assembled on the arms of a tripod-shaped DNA origami scaffold.

While most of these examples involve the use of chemical reagents to achieve the reconfigurable change of the nanostructure, Yan et al.[50] have reported a light-induced reversible dissociation/association of gold nanoparticle aggregates linked with azobenzene-modified photoswithchable DNAs. The reversible photoisomerization of azobenzene between the *trans* and

cis form causes photomelting/rehybridzation of the dsDNA linkers. The advent of azobenzene-phosphoamidite chemistry provides the opportunity to incorporate photo-triggered functionality in potential applications of DNA-linked nanomaterials. This motivates my work on reversibly reconfigurable gold nanoparticle dimers linked with a photoswitchable hairpin DNA motif, discussed in Chapter 4 in the thesis.

Besides nucleic acids, a thermally-responsive polymer, poly(N-isopropylacrylamide) (PNIPAM) has also been widely popular to fabricate stimuli-responsive nanomaterials that enable a temperature-induced reconfiguration of the structures and optical properties of the materials.[51-54] PNIPAM undergoes a heat-induced reversible volume-phase transition between its expanded, hydrated and collapsed, dehydrated form around its lower critical solution temperature (LCST, 32 ºC -38 ºC), causing almost 90% reduction in volume,[55-58] which allows to reorganize the attached nanoparticles. Both single chain PNIPAM and crosslinked PNIPAM (hydrogels) have been used to assemble plasmonic nanomaterials. The heat-triggered actuation of the nanoparticles upon thermoreversible swelling-shrinking of the PNIPAM results in distinct optical features of the materials at its two different conformational states, which is employed in several applications ranging from sensing[59-62], targeted drug delivery[63-65] to catalysis[66]. For instance, Karg et al. have shown formation of super lattices of gold nanocrystals using PNIPAM polymer chains as the linker, where the interparticle spacing can be tailored by swelling-deswelling of PNIPAM with temperature.[67] Furthermore, Wu et al.[66] have designed core-shell nanostructures with gold nanoparticle core and PNIPAM microgel shell that exhibits temperature-induced reversible catalytic activity and tunable selectivity due to the thermally reversible volume-phase transition of PNIPAM. Gorelikov et al.[65] have reported synthesis of photothermally active PNIPAM microgels containing gold nanorods (AuNR), which undergo volume transition on exposure to near infra-red

radiation, and can be used for drug releasing purposes. Lopez et al.[68] have demonstrated heat-induced formation of local hot spots in AuNR doped PNIPAM microgels that results in thermally reversible SERS activity of the materials. These nanomaterials can serve as highly efficient SERS substrates in sensing applications. While temperature is certainly the most commonly used external stimuli, several researchers have also developed PNIPAM derivatives that are sensitive to pH, light, metal cations etc. by introducing functional molecules and side chains via copolymerization, which opens more opportunities to engineer stimuli-responsive reconfigurable nanomaterials.[69,70]

Silver nanoparticles (Ag nanoparticles) have also been incorporated into PNIPAM hydrogels to prepare reconfigurable plasmonic materials.[71] Besides the thermally sensitive optical responses,[72,73] SERS efficiency[74] and catalytic activity,[73,75-77] such hybrid materials exhibit antibacterial activities and have shown stimuli-triggered metal enhanced fluorescence effect.[78] Liu et al.[73] have reported synthesis of hybrid microgels by in-situ formation of silver nanoparticles inside PNIPAM microgels that exhibit reversible catalytic properties in response to temperature change between 20 to 40 ºC due to the heat induced volume change of PNIPAM. Moreover, Tang et al. have designed Ag nanoparticle incorporated poly(N-isopropylacrylamide-co-acrylic acid) (PNIPAM-co-PAA) hybrids that show stimuli-responsive metal enhanced fluorescence effect.[78] The separation between the fluorophore and the nanoparticle changes upon swelling-shrinking of the microgels that is controlled by adjusting the pH in the range 2-12 and temperature between 25-50 ºC. Silver nanoparticles doped PNIPAM microgels have also been used as building blocks to construct nanophotonic crystals that allow coupling between optical properties of the nanoparticles and Bragg diffraction.[79]

The unique synergistic properties of these PNIPAM based-plasmonic nanomaterials and their outstanding contribution to the advancement in nanophotonics, controlled drug delivery, and

sensing applications have inspired my research on thermally reconfigurable PNIPAM/silver nanoprism hybrid composite materials, presented in Chapter 5.

1.3 REFERENCES

(1) Rosi, N. L.; Mirkin, C. A. Nanostructures in biodiagnostics. *Chem. Rev.* **2005**, *105*, 1547-1562.

(2) Anker, J. N.; Hall, W. P.; Lyandres, O.; Shah, N. C.; Zhao, J.; Van Duyne, R. P. Biosensing with plasmonic nanosensors. *Nat. Mater.* **2008**, *7*, 442-453.

(3) Willets, K. A. Super-resolution imaging of interactions between molecules and plasmonic nanostructures. *Phys. Chem. Chem. Phys.* **2013**, *15*, 5345-5354.

(4) Willets, K. A.; Wilson, A. J.; Sundaresan, V.; Joshi, P. B. Super-Resolution Imaging and Plasmonics. *Chem. Rev.* **2017**, *117*, 7538-7582.

(5) Pillai, S.; Catchpole, K. R.; Trupke, T.; Green, M. A. Surface plasmon enhanced silicon solar cells. *J. Appl. Phys.* **2007**, *101*.

(6) Stavytska-Barba, M.; Salvador, M.; Kulkarni, A.; Ginger, D. S.; Kelley, A. M. Plasmonic Enhancement of Raman Scattering from the Organic Solar Cell Material P3HT/PCBM by Triangular Silver Nanoprisms. *J. Phys. Chem. C* **2011**, *115*, 20788-20794.

(7) Stratakis, E.; Kymakis, E. Nanoparticle-based plasmonic organic photovoltaic devices. *Mater. Today* **2013**, *16*, 133-146.

(8) Linic, S.; Aslam, U.; Boerigter, C.; Morabito, M. Photochemical transformations on plasmonic metal nanoparticles. *Nat. Mater.* **2015**, *14*, 567-576.

(9) Hou, W. B.; Cronin, S. B. A Review of Surface Plasmon Resonance-Enhanced Photocatalysis. *Adv. Funct. Mater.* **2013**, *23*, 1612-1619.

(10) Willets, K. A.; Van Duyne, R. P. Localized surface plasmon resonance spectroscopy and sensing. *Annu. Rev. Phys. Chem.* **2007**, *58*, 267-297.

(11) Jain, P. K.; Huang, X. H.; El-Sayed, I. H.; El-Sayed, M. A. Noble Metals on the Nanoscale: Optical and Photothermal Properties and Some Applications in Imaging, Sensing, Biology, and Medicine. *Acc. Chem. Res.* **2008**, *41*, 1578-1586.

(12) Nome, R. A.; Guffey, M. J.; Scherer, N. F.; Gray, S. K. Plasmonic Interactions and Optical Forces between Au Bipyramidal Nanoparticle Dimers. *J. Phys. Chem. A* **2009**, *113*, 4408-4415.

(13) Ma, W.; Kuang, H.; Wang, L. B.; Xu, L. G.; Chang, W. S.; Zhang, H. N.; Sun, M. Z.; Zhu, Y. Y.; Zhao, Y.; Liu, L. Q.; Xu, C. L.; Link, S.; Kotov, N. A. Chiral plasmonics of self-assembled nanorod dimers. *Sci. Rep.* **2013**, *3*.

(14) Chen, H. J.; Shao, L.; Li, Q.; Wang, J. F. Gold nanorods and their plasmonic properties. *Chem. Soc. Rev.* **2013**, *42*, 2679-2724.

(15) Link, S.; El-Sayed, M. A. Shape and size dependence of radiative, non-radiative and photothermal properties of gold nanocrystals. *Int. Rev. Phys. Chem.* **2000**, *19*, 409-453.

(16) Jain, P. K.; Eustis, S.; El-Sayed, M. A. Plasmon coupling in nanorod assemblies: Optical absorption, discrete dipole approximation simulation, and exciton-coupling model. *J. Phys. Chem. B* **2006**, *110*, 18243-18253.

(17) Funston, A. M.; Novo, C.; Davis, T. J.; Mulvaney, P. Plasmon Coupling of Gold Nanorods at Short Distances and in Different Geometries. *Nano Lett.* **2009**, *9*, 1651-1658.

(18) Jain, P. K.; El-Sayed, M. A. Plasmonic coupling in noble metal nanostructures. *Chem. Phys. Lett.* **2010**, *487*, 153-164.

(19) Myroshnychenko, V.; Rodriguez-Fernandez, J.; Pastoriza-Santos, I.; Funston, A. M.; Novo, C.; Mulvaney, P.; Liz-Marzan, L. M.; de Abajo, F. J. G. Modelling the optical response of gold nanoparticles. *Chem. Soc. Rev.* **2008**, *37*, 1792-1805.

(20) Halas, N. J.; Lal, S.; Chang, W. S.; Link, S.; Nordlander, P. Plasmons in Strongly Coupled Metallic Nanostructures. *Chem. Rev.* **2011**, *111*, 3913-3961.

(21) Wang, H.; Brandl, D. W.; Nordlander, P.; Halas, N. J. Plasmonic nanostructures: Artificial molecules. *Acc. Chem. Res.* **2007**, *40*, 53-62.

(22) Sheikholeslami, S.; Jun, Y. W.; Jain, P. K.; Alivisatos, A. P. Coupling of Optical Resonances in a Compositionally Asymmetric Plasmonic Nanoparticle Dimer. *Nano Lett.* **2010**, *10*, 2655-2660.

(23) Halas, N. J.; Lal, S.; Link, S.; Chang, W. S.; Natelson, D.; Hafner, J. H.; Nordlander, P. A Plethora of Plasmonics from the Laboratory for Nanophotonics at Rice University. *Adv. Mater.* **2012**, *24*, 4842-4877.

(24) Najafabadi, A. F.; Pakizeh, T. Analytical Chiroptics of 2D and 3D Nanoantennas. *ACS Photonics* **2017**, *4*, 1447-1452.

(25) Shegai, T.; Chen, S.; Miljkovic, V. D.; Zengin, G.; Johansson, P.; Kall, M. A bimetallic nanoantenna for directional colour routing. *Nat.Commun.* **2011**, *2*.

(26) Yen, C. W.; Mahmoud, M. A.; El-Sayed, M. A. Photocatalysis in Gold Nanocage Nanoreactors. *J. Phys. Chem. A* **2009**, *113*, 4340-4345.

(27) Boote, B. W.; Byun, H.; Kim, J. H. Silver-Gold Bimetallic Nanoparticles and Their Applications as Optical Materials. *J. Nanosci. Nanotechnol.* **2014**, *14*, 1563-1577.

(28) Guo, L. H.; Ferhan, A. R.; Chen, H. L.; Li, C. M.; Chen, G. N.; Hong, S.; Kim, D. H. Distance-Mediated Plasmonic Dimers for Reusable Colorimetric Switches: A Measurable Peak Shift of More than 60 nm. *Small* **2013**, *9*, 234-240.

(29) Kim, K.; Oh, J. W.; Lee, Y. K.; Son, J.; Nam, J. M. Associating and Dissociating Nanodimer Analysis for Quantifying Ultrasmall Amounts of DNA. *Angew. Chem. Int. Ed.* **2017**, *56*, 9877-9880.

(30) Zhao, W.; Brook, M. A.; Li, Y. F. Design of Gold Nanoparticle-Based Colorimetric Biosensing Assays. *ChemBioChem* **2008**, *9*, 2363-2371.

(31) Sepulveda, B.; Angelome, P. C.; Lechuga, L. M.; Liz-Marzan, L. M. LSPR-based nanobiosensors. *Nano Today* **2009**, *4*, 244-251.

(32) Jain, P. K.; Huang, X.; El-Sayed, I. H.; El-Sayad, M. A. Review of some interesting surface plasmon resonance-enhanced properties of noble metal nanoparticles and their applications to biosystems. *Plasmonics* **2007**, *2*, 107-118.

(33) Jain, P. K.; Ei-Sayed, M. A. Surface plasmon resonance sensitivity of metal nanostructures: Physical basis and universal scaling in metal nanoshells. *J. Phys. Chem. C* **2007**, *111*, 17451-17454.

(34) Xu, H. X.; Bjerneld, E. J.; Kall, M.; Borjesson, L. Spectroscopy of single hemoglobin molecules by surface enhanced Raman scattering. *Phys. Rev. Lett.* **1999**, *83*, 4357-4360.

(35) Le Ru, E. C.; Etchegoin, P. G.; Meyer, M. Enhancement factor distribution around a single surface-enhanced Raman scattering hot spot and its relation to single molecule detection. *J. Chem. Phys.* **2006**, *125*.

(36) Nie, S. M.; Emery, S. R. Probing single molecules and single nanoparticles by surface-enhanced Raman scattering. *Science* **1997**, *275*, 1102-1106.

(37) Le Ru, E. C.; Etchegoin, P. G. Single-Molecule Surface-Enhanced Raman Spectroscopy. *Annual Review of Physical Chemistry, Vol 63* **2012**, *63*, 65-87.

(38) Willets, K. A. Super-resolution imaging of SERS hot spots. *Chem. Soc. Rev.* **2014**, *43*, 3854-3864.

(39) Karatay, D. U.; Salvador, M.; Yao, K.; Jen, A. K. Y.; Ginger, D. S. Performance limits of plasmon-enhanced organic photovoltaics. *Appl. Phys. Lett.* **2014**, *105*.

(40) Boriskina, S. V.; Ghasemi, H.; Chen, G. Plasmonic materials for energy: From physics to applications. *Mater. Today* **2013**, *16*, 375-386.

(41) Kumar, A.; Hwang, J. H.; Kumar, S.; Nam, J. M. Tuning and assembling metal nanostructures with DNA. *Chem. Commun.* **2013**, *49*, 2597-2609.

(42) Kuzyk, A.; Schreiber, R.; Zhang, H.; Govorov, A. O.; Liedl, T.; Liu, N. Reconfigurable 3D plasmonic metamolecules. *Nat. Mater.* **2014**, *13*, 862-866.

(43) Nykypanchuk, D.; Maye, M. M.; van der Lelie, D.; Gang, O. DNA-guided crystallization of colloidal nanoparticles. *Nature* **2008**, *451*, 549-552.

(44) Macfarlane, R. J.; Lee, B.; Jones, M. R.; Harris, N.; Schatz, G. C.; Mirkin, C. A. Nanoparticle Superlattice Engineering with DNA. *Science* **2011**, *334*, 204-208.

(45) Tan, S. J.; Campolongo, M. J.; Luo, D.; Cheng, W. L. Building plasmonic nanostructures with DNA. *Nat. Nanotechnol.* **2011**, *6*, 268-276.

(46) Zhang, T. T.; Li, H.; Hou, S. W.; Dong, Y. Q.; Pang, G. S.; Zhane, Y. W. Construction of Plasmonic Core-Satellite Nanostructures on Substrates Based on DNA-Directed Self-Assembly as a Sensitive and Reproducible Biosensor. *ACS Appl. Mater. Interfaces* **2015**, *7*, 27131-27139.

(47) Maye, M. M.; Kumara, M. T.; Nykypanchuk, D.; Sherman, W. B.; Gang, O. Switching binary states of nanoparticle superlattices and dimer clusters by DNA strands. *Nat. Nanotechnol.* **2010**, *5*, 116-120.

(48) Kuzyk, A.; Schreiber, R.; Fan, Z.; Pardatscher, G.; Roller, E.-M.; Hoegele, A.; Simmel, F. C.; Govorov, A. O.; Liedl, T. DNA-based self-assembly of chiral plasmonic nanostructures with tailored optical response. *Nature* **2012**, *483*, 311-314.

(49) Zhan, P. F.; Dutta, P. K.; Wang, P. F.; Song, G.; Dai, M. J.; Zhao, S. X.; Wang, Z. G.; Yin, P.; Zhang, W.; Ding, B. Q.; Ke, Y. G. Reconfigurable Three-Dimensional Gold Nanorod Plasmonic Nanostructures Organized on DNA Origami Tripod. *ACS Nano* **2017**, *11*, 1172-1179.

(50) Yan, Y. Q.; Chen, J. I. L.; Ginger, D. S. Photoswitchable Oligonucleotide-Modified Gold Nanoparticles: Controlling Hybridization Stringency with Photon Dose. *Nano Lett.* **2012**, *12*, 2530-2536.

(51) Karg, M.; Hellweg, T. New "smart" poly(NIPAM) microgels and nanoparticle microgel hybrids: Properties and advances in characterisation. *Curr. Opin. Colloid Interface Sci.* **2009**, *14*, 438-450.

(52) Karg, M.; Hellweg, T. Smart inorganic/organic hybrid microgels: Synthesis and characterisation. *J. Mater. Chem.* **2009**, *19*, 8714-8727.

(53) Roy, D.; Brooks, W. L. A.; Sumerlin, B. S. New directions in thermoresponsive polymers. *Chem. Soc. Rev.* **2013**, *42*, 7214-7243.

(54) Wang, C.; Flynn, N. T.; Langer, R. Controlled structure and properties of thermoresponsive nanoparticle-hydrogel composites. *Adv. Mater.* **2004**, *16*, 1074-+.

(55) Schild, H. G. Poly (N-isopropylacrylamide) - Experiment, Theory and Application. *Prog. Polym. Sci.* **1992**, *17*, 163-249.

(56) Osa, M. Aqueous Solution Properties of Poly(N-isopropylacrylamide). *Kobunshi Ronbunshu* **2009**, *66*, 273-288.

(57) Chiantore, O.; Guaita, M.; Trossarelli, L. SOLUTION PROPERTIES OF POLY(N-ISOPROPYLACRYLAMIDE). *Macromol. Chem. Phys.* **1979**, *180*, 969-973.

(58) Kubota, K.; Fujishige, S.; Ando, I. SOLUTION PROPERTIES OF POLY(N-ISOPROPYLACRYLAMIDE) IN WATER. *Polym. J.* **1990**, *22*, 15-20.

(59) Li, X.; Gao, Y. F.; Serpe, M. J. Responsive Polymer-Based Assemblies for Sensing Applications. *Macromol. Rapid Commun.* **2015**, *36*, 1382-1392.

(60) Guan, Y.; Zhang, Y. J. PNIPAM microgels for biomedical applications: from dispersed particles to 3D assemblies. *Soft Matter* **2011**, *7*, 6375-6384.

(61) Han, D. M.; Zhang, Q. M.; Serpe, M. J. Poly (N-isopropylacrylamide)-co-(acrylic acid) microgel/Ag nanoparticle hybrids for the colorimetric sensing of H2O2. *Nanoscale* **2015**, *7*, 2784-2789.

(62) Stuart, M. A. C.; Huck, W. T. S.; Genzer, J.; Muller, M.; Ober, C.; Stamm, M.; Sukhorukov, G. B.; Szleifer, I.; Tsukruk, V. V.; Urban, M.; Winnik, F.; Zauscher, S.; Luzinov, I.; Minko, S. Emerging applications of stimuli-responsive polymer materials. *Nat. Mater.* **2010**, *9*, 101-113.

(63) Kang, H. Z.; Trondoli, A. C.; Zhu, G. Z.; Chen, Y.; Chang, Y. J.; Liu, H. P.; Huang, Y. F.; Zhang, X. L.; Tan, W. H. Near-Infrared Light-Responsive Core-Shell Nanogels for Targeted Drug Delivery. *ACS Nano* **2011**, *5*, 5094-5099.

(64) Kawano, T.; Niidome, Y.; Mori, T.; Katayama, Y.; Niidome, T. PNIPAM Gel-Coated Gold Nanorods, for Targeted Delivery Responding to a Near-Infrared Laser. *Bioconjugate Chem.* **2009**, *20*, 209-212.

(65) Gorelikov, I.; Field, L. M.; Kumacheva, E. Hybrid microgels photoresponsive in the near-infrared spectral range. *J. Am. Chem. Soc.* **2004**, *126*, 15938-15939.

(66) Wu, S.; Dzubiella, J.; Kaiser, J.; Drechsler, M.; Guo, X. H.; Ballauff, M.; Lu, Y. Thermosensitive Au-PNIPA Yolk-Shell Nanoparticles with Tunable Selectivity for Catalysis. *Angew. Chem. Int. Ed.* **2012**, *51*, 2229-2233.

(67) Karg, M.; Hellweg, T.; Mulvaney, P. Self-Assembly of Tunable Nanocrystal Superlattices Using Poly-(NIPAM) Spacers. *Adv. Funct. Mater.* **2011**, *21*, 4668-4676.

(68) Fernandez-Lopez, C.; Polavarapu, L.; Solis, D. M.; Taboada, J. M.; Obelleiro, F.; Contreras-Caceres, R.; Pastoriza-Santos, I.; Perez-Juste, J. Gold Nanorod-pNIPAM Hybrids with Reversible Plasmon Coupling: Synthesis, Modeling, and SERS Properties. *ACS Appl. Mater. Interfaces* **2015**, *7*, 12530-12538.

(69) Rittikulsittichai, S.; Kolhatkar, A. G.; Sarangi, S.; Vorontsova, M. A.; Vekilov, P. G.; Brazdeikis, A.; Lee, T. R. Multi-responsive hybrid particles: thermo-, pH-, photo-, and magneto-responsive magnetic hydrogel cores with gold nanorod optical triggers. *Nanoscale* **2016**, *8*, 11851-11861.

(70) Wu, W. T.; Mitra, N.; Yan, E. C. Y.; Zhou, S. Q. Multifunctional Hybrid Nanogel for Integration of Optical Glucose Sensing and Self-Regulated Insulin Release at Physiological pH. *ACS Nano* **2010**, *4*, 4831-4839.

(71) Begum, R.; Naseem, K.; Farooqi, Z. H. A review of responsive hybrid microgels fabricated with silver nanoparticles: synthesis, classification, characterization and applications. *J. Sol-Gel Sci. Technol.* **2016**, *77*, 497-515.

(72) Dong, Y.; Ma, Y.; Zhai, T. Y.; Shen, F. G.; Zeng, Y.; Fu, H. B.; Yao, J. N. Silver nanoparticles stabilized by thermoresponsive microgel particles: Synthesis and evidence of an electron donor-acceptor effect. *Macromol. Rapid Commun.* **2007**, *28*, 2339-2345.

(73) Liu, Y. Y.; Liu, X. Y.; Yang, J. M.; Lin, D. L.; Chen, X.; Zha, L. S. Investigation of Ag nanoparticles loading temperature responsive hybrid microgels and their temperature controlled catalytic activity. *Colloids and Surfaces a-Physicochemical and Engineering Aspects* **2012**, *393*, 105-110.

(74) Liu, X. Y.; Wang, X. Q.; Zha, L. S.; Lin, D. L.; Yang, J. M.; Zhou, J. F.; Zhang, L. Temperature- and pH-tunable plasmonic properties and SERS efficiency of the silver nanoparticles within the dual stimuli-responsive microgels. *J. Mater. Chem. C* **2014**, *2*, 7326-7335.

(75) Farooqi, Z. H.; Khan, S. R.; Hussain, T.; Begum, R.; Ejaz, K.; Majeed, S.; Ajmal, M.; Kanwal, F.; Siddiq, M. Effect of crosslinker feed content on catalaytic activity of silver nanoparticles fabricated in multiresponsive microgels. *Korean J. Chem. Eng.* **2014**, *31*, 1674-1680.

(76) Ajmal, M.; Farooqi, Z. H.; Siddiq, M. Silver nanoparticles containing hybrid polymer microgels with tunable surface plasmon resonance and catalytic activity. *Korean J. Chem. Eng.* **2013**, *30*, 2030-2036.

(77) Lu, Y.; Mei, Y.; Drechsler, M.; Ballauff, M. Thermosensitive core-shell particles as carriers for Ag nanoparticles: Modulating the catalytic activity by a phase transition in networks. *Angew. Chem. Int. Ed.* **2006**, *45*, 813-816.

(78) Tang, F.; Ma, N.; Tong, L. Y.; He, F.; Li, L. D. Control of Metal-Enhanced Fluorescence with pH- and Thermoresponsive Hybrid Microgels. *Langmuir* **2012**, *28*, 883-888.

(79) Xu, S. Q.; Zhang, J. G.; Paquet, C.; Lin, Y. K.; Kumacheva, E. From hybrid microgels to photonic crystals. *Adv. Funct. Mater.* **2003**, *13*, 468-472.

Chapter 2. BACKGROUND KNOWLEDGE

2.1 REVERSIBLE PHOTOISOMERIZATION OF AZOBENZENE

Azobenzene is a derivative of diazene molecule where two phenyl groups replace the two hydrogens on both size of N=N (azo) bond. The molecule has two geometrical isomers; *trans*-azobenzene and *cis*-azobenzene. At equilibrium in the dark, the molecule predominantly (> 99.99%) exists in the more stable *trans* configuration,[1-3] which is a planar structure with C_{2h} symmetry and has zero dipole moment.[4,5] The *cis*-isomer of azobenzene is non-planar with C_2 symmetry[6] and exhibits a net dipole moment of 3 Debye.[7] Azobenzenes are known for their clean reversible photoisomerization between the *trans* and *cis* forms that exhibits remarkable photostability and significant difference in the structural and optical properties of the two isomers. Exposure to UV light (300nm–400 nm) isomerizes the *trans* azobenzene into the *cis* form and the blue light (440 nm–480 nm) irradiation converts the *cis* isomer back to the *trans* form (Figure 2.1(a)). These photoisomerizaion reactions occur in picosecond timescale.[8,9] The *cis* form also thermally isomerizes back to the *trans* form spontaneously in the dark at room temperature with an activation energy of 90 kJ/mol.[10,11] The half-life of the *cis* isomer is sensitive to the nature of the substitution on phenyl ring.[12]

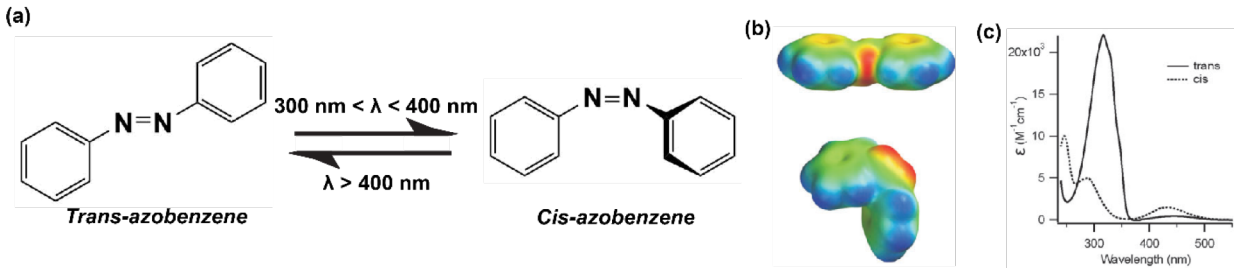

Figure 2.1 (a) Reversible *trans*-to-*cis* photoisomerization of azobenzene, (b) Electrostatic potential (red-negative, blue-positive) of *trans* and *cis* azobenzene structures, (c) Absorption spectra of *trans* and *cis* azobenzene solution in ethanol. (Image is reprinted with permission of reference 36.)

The two isomers have unique and distinct spectral features as indicated in Figure 2.1 (c). The *trans*-azobenzene exhibits two separate absorption maxima:[13-15] the symmetry allowed $\pi \rightarrow \pi^*$ transition gives rise to the more intense absorption band around 330 nm (ε ~ 22000 M^{-1} cm^{-1}),[16-18] while the symmetry forbidden $n \rightarrow \pi^*$ electronic transition is responsible for the weak absorption band in the visible region (λ_{max} ~ 450 nm, ε ~ 400 M^{-1} cm^{-1}).[19] On the other hand the *cis*-azobenzene shows weaker $\pi \rightarrow \pi^*$ absorption bands in the UV region (λ_{max} ~ 270 nm, ε ~ 5000 L mol^{-1} cm^{-1}; λ_{max} ~250 nm, ε ~ 11 000 L mol^{-1} cm^{-1}) and a stronger absorption maxima due to the $n \rightarrow \pi^*$ transition around 450 nm (ε ~ 1500 M^{-1} cm^{-1}).[16,17]

Several groups have performed ultrafast spectroscopy along with ab-initio and semi-empirical calculations to probe the *trans*-to-*cis* isomerization mechanisms of azobenzene. The rate and efficiency of the isomerization process along with the reaction pathways depends on irradiation wavelength,[20-22] solvent,[23-25] temperature,[26] pressure,[27] and molecular substitutions on the phenyl rings[28,29] in the azobenzene. Based on these results, several mechanisms have been reported in the literature to explain the details of the complex isomerization processes: rotation, inversion, concerted inversion and, inversion assisted rotation (see Figure 2.2).[4,28,30,31] In the rotation mechanism, the N=N bond breaks upon excitation with the UV photons, followed by phenyl ring rotation around the N—N bond. While the C—N—N—C dihedral angle changes but the N—N—C bond angle remains constant at 120º in the rotation mechanism, the inversion mechanism involves a change in the N=N—C bond angle to 180º, keeping the C—N=N—C dihedral angle constant at 0º, resulting in one sp-hybridized azo-nitrogen atom in the transition state. Both the N=N—C bond angle keeps increasing during a concerted inversion mechanism, leading to a linear transition state. In the inversion assisted rotation mechanism of azobenzene

isomerization, mainly the C—N—N—C dihedral angle changes with a small change in the N=N—C bond angle at the same time. Irrespective of the mechanism, the transition states can relax back to either the *cis* or the *trans* isomer, thus, both the isomers exist at the photostationary state. No single mechanism is able provide adequate explanation for all the characteristics of the isomerization process.

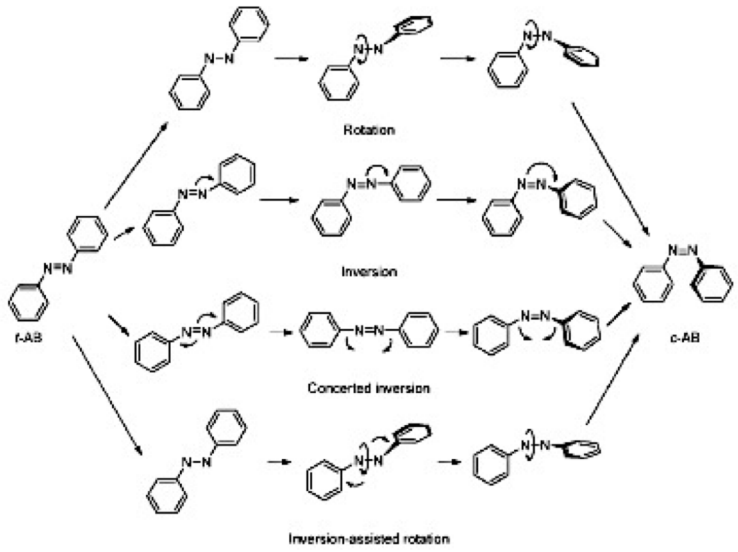

Figure 2.2 Scheme for proposed mechanisms for *trans*-to-*cis* isomerization of azobenzene (Image is preprinted with permission of reference 30.)

The photoisomerization efficiency of azobenzene is generally measured by quantum yield (QY), which is defined as the ratio of isomerized azobenzene to the number of irradiation photons absorbed.[20,32] For the reversible photoisomerization process of azobenzene two separate quantum yields can be measured: *trans*-to-*cis* and *cis*-to-*trans* quantum yield. Both the quantum yields are affected by irradiation wavelength,[20,25] temperature[26] as well as viscosity and polarity of the solvents.[23,24] As the two photoisomerization reactions follow different pathways, the sum of the two quantum yields is not equal to unity.[30] The rate of the *trans*-to-*cis* reversible isomerization of azobenzene can be expressed by the following differential rate equation assuming that the

quantum yields are independent of the irraditation intensity and the concentration of the isomers, also assuming a monochromatic light source, Beer's law and complete stirring of the solution.[20,33]

$$\frac{\mathbf{d}[\boldsymbol{cis}]_{\mathbf{t}}}{\mathbf{dt}} = \frac{\mathbf{I}^{\lambda}\,\mathbf{l}\left(\mathbf{1}-\mathbf{10}^{-\mathbf{abs}_{\mathbf{t}}^{\lambda}}\right)\phi_{\boldsymbol{trans}}^{\lambda}\boldsymbol{\varepsilon}_{\boldsymbol{trans}}^{\lambda}}{\mathbf{V}\,\mathbf{abs}_{\mathbf{t}}^{\lambda}}\,[\boldsymbol{trans}]_{\mathbf{t}} - \frac{\mathbf{I}^{\lambda}\mathbf{l}\left(\mathbf{1}-\mathbf{10}^{-\mathbf{abs}_{\mathbf{t}}^{\lambda}}\right)\phi_{\boldsymbol{cis}}^{\lambda}\boldsymbol{\varepsilon}_{\boldsymbol{cis}}^{\lambda}}{\mathbf{V}\,\mathbf{abs}_{\mathbf{t}}^{\lambda}}\,[\boldsymbol{cis}]_{\mathbf{t}} - \mathbf{k}_{\mathbf{therm}}[\boldsymbol{cis}]_{\mathbf{t}}$$

$$= \frac{\mathbf{I}^{\lambda}\,\mathbf{l}\left(\mathbf{1}-\mathbf{10}^{-\mathbf{abs}_{\mathbf{t}}^{\lambda}}\right)\phi_{\boldsymbol{trans}}^{\lambda}\boldsymbol{\varepsilon}_{\boldsymbol{trans}}^{\lambda}}{\mathbf{V}\,\mathbf{abs}_{\mathbf{t}}^{\lambda}}\,([\boldsymbol{trans}]_{\mathbf{0}} - [\boldsymbol{cis}]_{\mathbf{t}}) - \frac{\mathbf{I}^{\lambda}\mathbf{l}\left(\mathbf{1}-\mathbf{10}^{-\mathbf{abs}_{\mathbf{t}}^{\lambda}}\right)\phi_{\boldsymbol{cis}}^{\lambda}\boldsymbol{\varepsilon}_{\boldsymbol{cis}}^{\lambda}}{\mathbf{V}\,\mathbf{abs}_{\mathbf{t}}^{\lambda}}\,[\boldsymbol{cis}]_{\mathbf{t}} - \mathbf{k}_{\mathbf{therm}}[\boldsymbol{cis}]_{\mathbf{t}} \qquad (\mathbf{1})$$

The first two terms in the equation $(\mathbf{1})$ define the rate of *trans*-to-*cis* and *cis*-to-*trans* photoisomerization process, respectively, with $\phi_{\boldsymbol{trans}}^{\lambda}$ and $\phi_{\boldsymbol{cis}}^{\lambda}$ as the respective quantum yields. $\boldsymbol{\varepsilon}_{\boldsymbol{trans}}^{\lambda}$ and $\boldsymbol{\varepsilon}_{\boldsymbol{cis}}^{\lambda}$ are the molar absorption coefficients of *trans* and *cis* forms of azobenzene, respectively, at the excitation wavelength. $[\boldsymbol{trans}]_{\mathbf{0}}$ is the concentration of *trans*-azobenzene before UV irradiation, which we can assume as the total initial concentration of the azobenzene in the system and $[\boldsymbol{cis}]_{\mathbf{t}}$ is the concentration of *cis*-azobenzene after time $\mathbf{t}$ of UV exposure. $\mathbf{I}^{\lambda}$ is the intensity of the incident UV light, $\mathbf{l}$ is the beam path length through the solution in UV-vis absorption measurement, which is 1 cm, $\mathbf{abs}_{\mathbf{t}}^{\lambda}$ is the time dependent absorbance of the sample at the excitation wavelength at time $\mathbf{t}$, and $\mathbf{V}$ is the volume of the solution. The last term in equation $(\mathbf{1})$ takes into account the thermal *cis*-to-*trans* isomerization with a first order rate constant of $\mathbf{k}_{\mathbf{therm}}$. This equation indicates that the ratio of *trans* to *cis* isomer at the photostationary state depends on the irradiation wavelength. For example, photoisomerization achieved by 316 nm irradiation yields ~80 % of the *cis* isomer whereas continuous exposure to 436 nm results in ~90% of the *trans* isomer at the photostationary state.[34]

2.2 AZOBENZENE-MODIFIED DNA

Due to its reversible photochromic properties, azobenzene has been used as an effective molecular photoswitch in a variety of applications, ranging from optoelectronics to photocontrol of biomolecules.[35,36] Azobenzene molecules have been successfully embedded in polymers, peptides and proteins through chemical modifications to introduce photoresponsivity without affecting their stability or biological functions.[36] Significant similarity of the spatial size and polarity distribution of the planar *trans*-form and a DNA base pair[30,37-39] has facilitated the incorporation of azobenzenes in nucleic acids. Asanuma and co-workers have developed the synthetic modification of oligonucleotides with azobenzene, where it is inserted into the DNA phosphate backbone through a D-threoninol linkage.[40] NMR studies reveal that *trans*-azobenzene is capable of intercalating with the neighboring base pairs through pi-stacking interaction that leads to an overall stabilization of the double stranded DNA (dsDNA), despite of the structural distortions caused by azobenzene insertion.[41] This additional stabilization is reflected in the substantial increment of the melting temperature of the azobenzene-modified dsDNA compared to the native duplex.[42,43] UV-induced photoisomerization of *trans*-azobenzene to the non-planar *cis*-form disrupts the π- π interaction due to steric hindrance and destabilizes the duplex structure. Thus, *trans*-to-*cis* photoisomerization results in a lowering of the melting temperature of the azobenzene-modified dsDNA compared to the unmodified duplex.[44] Blue light exposure converts *cis*-azobenzene back to the *trans* form and restores the stability of the dsDNA. Incorporation of several azobenzene units can lead to photo-induced dissociation and rehybridization of a dsDNA, allowing a reversible control of the duplex forming activity of DNA by an external stimulus. Recent advancements of the azobenzene-modified-photoswitchable DNA chemistry have enabled its potential applications in light-driven DNA nanomotors,[45,46] photosensitive DNA aptamers,[47,48]

photoregulated DNA hybridization stringency [49-51] and enzymatic activity,[52-54] optically-controlled drug delivery[55] and gene regulation[56-58] etc. The ability to remotely control the functionality of nanomaterials and biological systems with light is what has motivated much of the work in this thesis on understanding the basic photophysics of azobenzenes incorporated in DNA sequences to improve the photoregulation efficiency of DNA based nanomaterials and biosensors.

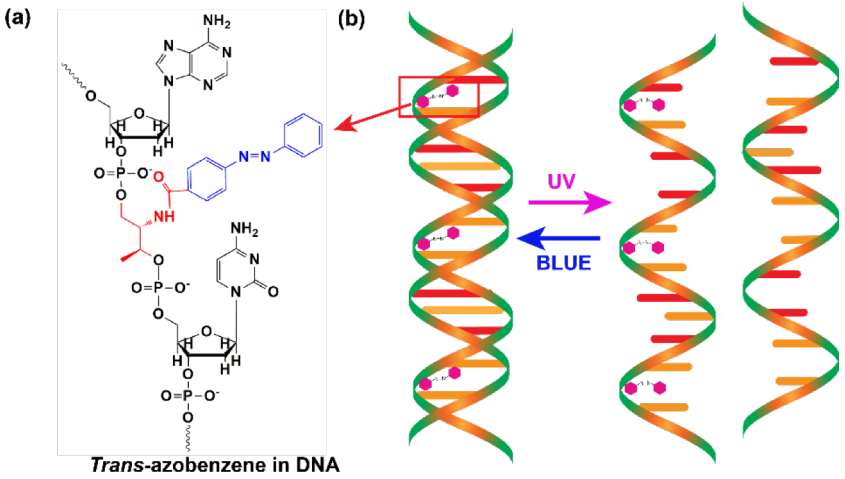

Figure 2.3 (a) Incorporation of azobenzene molecule (blue) into DNA backbone by D-threoninol linker (red), (b) Representation of the photo-induced melting and rehybridization of azobenzene-modified dsDNA on *trans*-to-*cis* reversible photoisomerization of azobenzene units in the DNA.

2.3 DNA-FUNCTIONALIZATION OF GOLD NANOPARTICLES

DNA has been extensively used as ligands[59-64] to link nanoparticles in a highly-ordered fashion through its unique base pairing capability. Mirkin and coworkers successfully demonstrated a synthetic protocol for DNA functionalization of gold nanoparticles in solution, where they attach a thiol-modified DNA on the gold nanoparticle surface via Au-S covalent bond.[65-68] The electrostatic repulsion between the negatively charged phosphate backbones of DNA makes it difficult to densely cover the nanoparticle surface with DNAs. Mirkin et al.

achieved a high loading density of the DNA strands by a gradual increment of the sodium ion concentration (salt-aging) that screens the repulsive interactions between the neighboring strands. The DNA sequences are usually comprised of three separate regions: 1. thiol modification at the 5' or 3' end that forms Au-S bond formation with the nanoparticle, 2. a spacer, typically 10-30 poly adenine (poly-A) or poly-thyamine (poly-T) which separates the nanoparticle core from the sensing region and 3. the active binding region that hybridizes with complementary target DNA sequences and can be modified according to the purpose of its application. These DNA functionalized gold nanoparticles can be precisely arranged into well-defined architectures through Watson-Crick base pairing between two complementary sequences.

DNA-conjugated gold nanoparticles and their assemblies are of widespread interest, spanning gene biosensing, [59,60] gene regulation[69,70], and therapeutics.[71,72] The recent progress of the azobenzene-phosphoramidite chemistry facilitates the incorporation of photosensitivity in the DNA-based nanomaterials that allows reversible reconfiguration of the nanostructures and remote control of their functionality in future diagnostics and sensing applications.[50,73] This has inspired my research on azobenzene-modified DNA-functionalized gold nanoparticles dimers that provides a basic understanding of the structural properties and optical responses of these discrete plasmonic dimers to facilitate their use as building blocks in designing optically reprogrammable bionanomaterials. I mainly followed Mirkin's 'salt aging' procedure to functionalize gold nanoparticles with DNA sequences and assembled them to form dimers through DNA hybridization. The azobenzene photoswitches are inserted in the functional part of the DNA sequences to introduce photoresponsivity in these DNA-linked gold nanoparticle dimers.

2.4 POLY(N-ISOPROPYLACRYLAMIDE) (PNIPAM) MICROGELS

Inspired by the responsivity of biological macromolecules, several responsive synthetic macromolecules have been developed with an aim to mimic the functionality and match compatibility of biomolecules. Stimuli-responsive polymers undergo structural transformation in response to a change in temperature, light, pH, and other external factors that alter the macroscopic properties of the polymers. Since heat is the most promising external stimulus, thermoresponsive polymer, poly(N-isopropylacrylamide) or PNIPAM is by far the most extensively investigated stimuli-sensitive polymer. PNIPAM can be readily synthesized by free radical polymerization with tunable particle size and narrow size distribution.[74] It exhibits a reversible volume-phase transition upon heating.[75-77] At room temperature PNIPAM is relatively hydrophilic, it absorbs water molecule while dissolving in the solution. The water molecules orient themselves around the polar region of the polymer to form hydrogen bonds in the polymer matrix, resulting in a hydrated swollen state of the polymer at room temperature. However, at higher temperatures hydrogen bonds with the water molecules are disrupted because of a higher entropy of the system, causing the polymer molecules to collapse by releasing the water and become hydrophobic. The swelling-deswelling behavior of the polymer is measured by the deswelling factor (α), which is the ratio of the volume of the collapsed state to the volume of swollen state of the polymer,[78,79] i.e. $\alpha = \frac{V(T)}{V_0} = \frac{R_h(T)^3}{R_0^3}$, assuming that polymer particles attain spherical shape in solution with R_h and R_0 as the hydrodynamic radius in shrunken and swollen state, respectively. For PNIPAM, the value of the deswelling factor typically lies in the range of 0.02-0.10. Lower critical solution temperature (LCST), at which a sharp volume-phase transition occurs, is typically in the range of 32-38 ºC for PNIPAM. However, LCST of the PNIPAM and

the swelling-shrinking kinetics can be modified by inserting hydrophobic and hydrophilic groups into the polymer chain through copolymerization or by alteration of the end groups.[80]

Hydrogels of PNIPAM are produced by chemically crosslinking the polymer network, which also exhibits the sharp change in volume on phase transition from hydrated swollen state to collapsed hydrophobic state near the critical solution temperature. PNIPAM microgels are hydrogels with size ranging from tens of nanometers to several microns.[80-83] Smaller size allows these PNIPAM microgels to undergo thermoreversible swelling-deswelling at a much faster rate compared to the bulky hydrogels,[80,84] which has been exploited in variety of applications ranging from biosensing, and drug delivery to designing smart nanomaterials.[83,85-87]

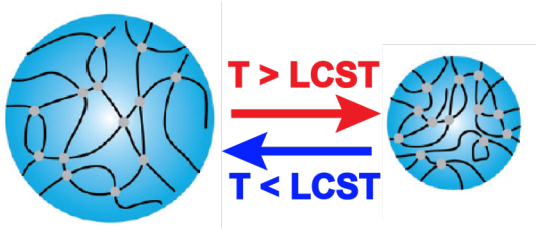

Figure 2.4 Schematic illustration of the thermally reversible swelling-deswelling of PNIPAM microgels around the lower critical solution temperature (LCST) of the polymer. The black lines are the polymer chains and the grey dots represent the crosslinking between them in the microgel. (Image is reprinted with the permission from the reference 79.)

2.5 PNIPAM/PLASMONIC NANOPARTICLE HYBRID MICROGELS

Due to their faster thermally reversible structural change, PNIPAM microgels are widely popular in designing reconfigurable nanomaterials by incorporating various shapes and sizes of gold and silver nanoparticles to enable stimuli-sensitive optical properties of the material that can be regulated by changing the temperature of the system. Such organic/inorganic hybrid nanomaterials are broadly categorized into three classes:[78,88] i) core-shell structure, which are typically formed by polymerization of the monomer unit on the nanoparticle surface, ii) microgels filled with nanoparticles, synthesized by in situ formation of the nanoparticle inside the PNIPAM microgel network, iii) microgels covered with nanoparticles, prepared by physical mixing of the nanoparticles with microgels dispersion. In all these conformations of the hybrids, the nanoparticles are widely separated by the hydrated expanded form of the microgel at low temperatures, and they are brought closer when the PNIPAM collapses at higher temperatures

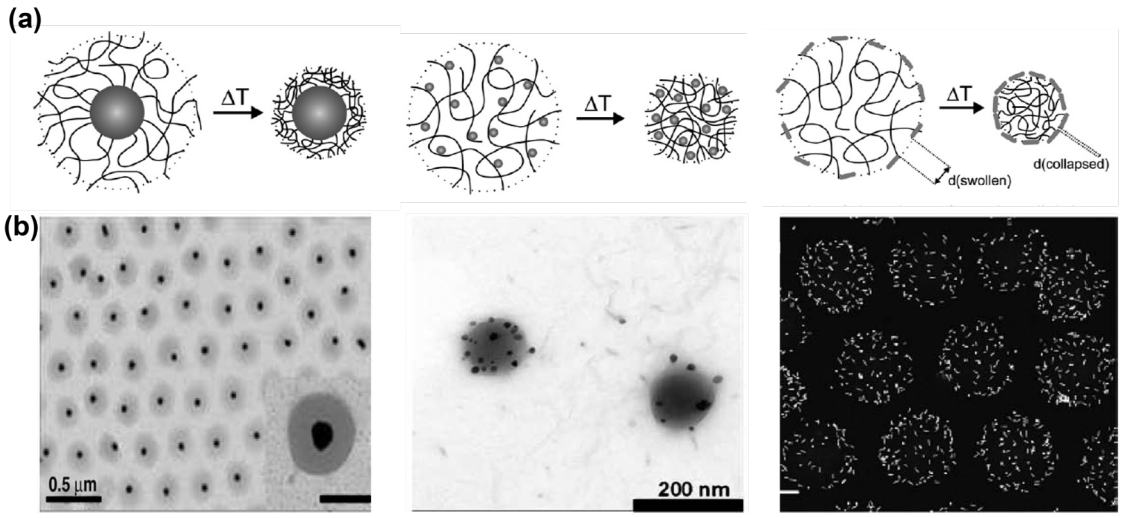

Figure 2.5 (a) Scheme (above) (b) SEM and TEM images (below) of three different types of reconfigurable nanomaterials composed of thermoresponsive PNIPAM microgels and metal nanoparticles. Core-shell structure (right), microgels filled with nanoparticles (middle), microgels covered with nanoparticles (left) (image is preprinted with permission of reference 78 and 79).

(beyond LCST), resulting in an increased interparticle plasmon coupling, and enhanced optical and electronic properties of the hybrid microgels.

The synthesis of core-shell nanoparticle/PNIPAM microgel hybrid structures and PNIPAM microgels filled with nanoparticles gives rise to a poor control over the size of the microgels or the morphology of the nanoparticles. However, fabrication of the hybrid microgels by mixing the individual components allows us to tailor the sizes of the constituent particles, shape of the nanoparticles, and the loading density of the nanoparticles on the microgel surface, and thus enables a wide range of tunability of the optical responses of such hybrid nanostructures. For example, Lim et al.[89] have successfully assembled gold nanospheres on PNIPAM microgels by mixing these two separately-prepared components. These hybrid microgels exhibit a thermoreversible optical bandwidth that increases with temperature and can be readily modulated by changing the nanoparticle size. Lopez et al.[90] have also shown a variation in the optical properties of gold nanorods (AuNR) doped PNIPAM hybrid microgels in the visible and near IR region by tuning the aspect ratio of nanorods and its loading density on the PNIPAM microgel.

However, the majority of the hybrid PNIPAM microgels incorporated with silver nanoparticles are synthesized by in situ reduction of the Ag^+ inside the microgel matrix.[88] This method restricts the tunability of nanoparticle size, shape and dispersity in the hydrogel, and thus limits the optical performances of the materials. In this thesis, I present my research on silver nanoprisms containing PNIPAM microgels, synthesized by mixing the two individual components, which provides the opportunity to expand the thermoreversible optical responses of such hybrid microgels in the visible and IR region by independently varying the size and loading density of nanoprisms on the microgels.

2.6 REFERENCES

(1) Dias, A. R.; Dapiedade, M. E. M.; Simoes, J. A. M.; Simoni, J. A.; Teixeira, C.; Diogo, H. P.; Yang, M. Y.; Pilcher, G. Enthalpies of Formation of *Cis*-Azobenzene and *Trans*-Azobenzene *J. Chem. Thermodyn.* **1992**, *24*, 439-447.

(2) Mita, I.; Horie, K.; Hirao, K. Photochemistry in Polymer Solids. 9. Photoisomerization of Azobenzene in a Polycarbonate Film. *Macromolecules* **1989**, *22*, 558-563.

(3) Rau, H. Spectroscopic Properties of Organic Azo-Compounds. *Angew. Chem. Int. Ed.* **1973**, *12*, 224-235.

(4) Crecca, C. R.; Roitberg, A. E. Theoretical study of the isomerization mechanism of azobenzene and disubstituted azobenzene derivatives. *J. Phys. Chem. A* **2006**, *110*, 8188-8203.

(5) Brown, C. J. A Refinement of Crystal Structure of Azobenzene. *Acta Crystallogr.* **1966**, *21*, 146-152.

(6) Gagliardi, L.; Orlandi, G.; Bernardi, F.; Cembran, A.; Garavelli, M. A theoretical study of the lowest electronic states of azobenzene: the role of torsion coordinate in the cis-trans photoisomerization. *Theor. Chem. Acc.* **2004**, *111*, 363-372.

(7) Fliegl, H.; Kohn, A.; Hattig, C.; Ahlrichs, R. Ab initio calculation of the vibrational and electronic spectra of trans- and cis-azobenzene. *J. Am. Chem. Soc.* **2003**, *125*, 9821-9827.

(8) Kobayashi, T.; Degenkolb, E. O.; Rentzepis, P. M. Picosecond Spectroscopy of 1-Phenylazo-2-hydroxynaphthalene. *J. Phys. Chem.* **1979**, *83*, 2431-2434.

(9) Lednev, I. K.; Ye, T. Q.; Hester, R. E.; Moore, J. N. Femtosecond time-resolved UV-visible absorption spectroscopy of trans-azobenzene in solution. *J. Phys. Chem.* **1996**, *100*, 13338-13341.

(10) Haberfield, P.; Block, P. M.; Lux, M. S. Enthalpies Of Solvent Transfer Of Transition-States In Cis-Trans Isomerization Of Azo-Compounds - Rotation Vs Nitrogen Inversion Mechanism. *J. Am. Chem. Soc.* **1975**, *97*, 5804-5806.

(11) Brown, E. V.; Granneman, G. R. Cis-Trans Isomerism In Pyridyl Analogs Of Azobenzene - Kinetic And Molecular-Orbital Analysis. *J. Am. Chem. Soc.* **1975**, *97*, 621-627.

(12) Yager, K. G.; Barrett, C. J. Novel photo-switching using azobenzene functional materials. *Journal of Photochemistry and Photobiology a-Chemistry* **2006**, *182*, 250-261.

(13) Hamm, P.; Ohline, S. M.; Zinth, W. Vibrational cooling after ultrafast photoisomerization of azobenzene measured by femtosecond infrared spectroscopy. *J. Chem. Phys.* **1997**, *106*, 519-529.

(14) Lednev, I. K.; Ye, T. Q.; Matousek, P.; Towrie, M.; Foggi, P.; Neuwahl, F. V. R.; Umapathy, S.; Hester, R. E.; Moore, J. N. Femtosecond time-resolved UV-visible absorption spectroscopy of trans-azobenzene: dependence on excitation wavelength. *Chem. Phys. Lett.* **1998**, *290*, 68-74.

(15) Tahara, T.: *Advances in Multi-Photon Processes and Spectroscopy*; World ScientificPublishing Co.: Singapore, 2004; Vol. 16. pp. 1-72.

(16) Forber, C. L.; Kelusky, E. C.; Bunce, N. J.; Zerner, M. C. Electronic-Spectra Of Cis-Azobenzenes And Trans-Azobenzenes - Consequences Of Ortho Substitution. *J. Am. Chem. Soc.* **1985**, *107*, 5884-5890.

(17) Knoll, H.: *CRC Handbook of Organic Photochemistry and Photobiology* 2ed.; CRC Press FL, 2004.

(18) Dyck, R. H.; McClure, D. S. Ultraviolet Spectra Of Stilbene, P-Monohalogen Stilbenes, And Azobenzene And Trans To Cis Photoisomerization Process. *J. Chem. Phys.* **1962**, *36*, 2326-2345.

(19) Cusati, T.; Granucci, G.; Persico, M.; Spighi, G. Oscillator strength and polarization of the forbidden n ->pi(*) band of trans-azobenzene: A computational study. *J. Chem. Phys.* **2008**, *128*.

(20) Zimmerman, G.; Chow, L. Y.; Paik, U. J. The Photochemical Isomerization of Azobenzene1. *J. Am. Chem. Soc.* **1958**, *80*, 3528-3531.

(21) Liang, Z. C.; Ming, H.; Wang, P.; Zhang, J. Y.; Xie, J. P.; Zhang, Q. J. Nonlinearly optical-optical isomerization cycle in azobenzene liquid crystal polymers. *J. Appl. Phys.* **2001**, *90*, 5866-5870.

(22) Loudwig, S.; Bayley, H. Photoisomerization of an individual azobenzene molecule in water: An on-off switch triggered by light at a fixed wavelength. *J. Am. Chem. Soc.* **2006**, *128*, 12404-12405.

(23) Bortolus, P.; Monti, S. Cis-Trans Photoisomerization Of Azobenzene - Solvent And Triplet Donor Effects. *J. Phys. Chem.* **1979**, *83*, 648-652.

(24) Gegiou, D.; Muszkat, K. A.; Fischer, E. Temperature dependence of photoisomerization. V. Effect of substituents on the photoisomerization of stilbenes and azobenzenes. *J. Am. Chem. Soc.* **1968**, *90*, 3907-3918.

(25) Siampiringue, N.; Guyot, G.; Monti, S.; Bortolus, P. The *cis- trans* Photoisomerization of Azobenzene - An Experimental Reexamination. *Journal of Photochemistry* **1987**, *37*, 185-188.

(26) Malkin, S.; Fischer, E. Temperature Dependence Of Photoisomerization .2. Quantum Yields Of *Cis* -- *Trans* Isomerizations In Azo-Compounds. *J. Phys. Chem.* **1962**, *66*, 2482-2486.

(27) Asano, T.; Okada, T.; Shinkai, S.; Shigematsu, K.; Kusano, Y.; Manabe, O. Temperature and Pressure Dependences of Thermal Cis-to-Trans Isomerization of Azobenzenes Which Evidence an Inversion Mechanism. *J. Am. Chem. Soc.* **1981**, *103*, 5161-5165.

(28) Front matter A2 - Sekkat, Zouheir. In *Photoreactive Organic Thin Films*; Knoll, W., Ed.; Academic Press: San Diego, 2002; pp i-ii.

(29) Rau, H.; Luddecke, E. On The Rotation-Inversion Controversy On Photo-Isomerization Of Azobenzenes - Experimental Proof Of Inversion. *J. Am. Chem. Soc.* **1982**, *104*, 1616-1620.

(30) Bandara, H. M. D.; Burdette, S. C. Photoisomerization in different classes of azobenzene. *Chem. Soc. Rev.* **2012**, *41*, 1809-1825.

(31) Curtin, D. Y.; Grubbs, E. J.; McCarty, C. G. Uncatalyzed Syn-Anti Isomerization Of Imines Oxime Ethers And Haloimines. *J. Am. Chem. Soc.* **1966**, *88*, 2775-2786.

(32) Contributors A2 - Sekkat, Zouheir. In *Photoreactive Organic Thin Films*; Knoll, W., Ed.; Academic Press: San Diego, 2002; pp xv-xvii.

(33) Rau, H.: 1 - Photoisomerization of Azobenzenes A2 - Sekkat, Zouheir. In *Photoreactive Organic Thin Films*; Knoll, W., Ed.; Academic Press: San Diego, 2002; pp 3-47.

(34) Fischer, E. Temperature Dependence Of Photoisomerization Equilibria .1. Azobenzene And The Azonaphthalenes. *J. Am. Chem. Soc.* **1960**, *82*, 3249-3252.

(35) Mahimwalla, Z.; Yager, K. G.; Mamiya, J.-i.; Shishido, A.; Priimagi, A.; Barrett, C. J. Azobenzene photomechanics: prospects and potential applications. *Polym. Bull.* **2012**, *69*, 967-1006.

(36) Beharry, A. A.; Woolley, G. A. Azobenzene photoswitches for biomolecules. *Chem. Soc. Rev.* **2011**, *40*, 4422-4437.

(37) Rau, H.: *Photochemistry and Photophysics*; CRC Press: Florida, 1990; Vol. 4. pp. 120 - 141.

(38) Lee, S.; Kang, H. S.; Park, J. K. Directional Photofluidization Lithography: Micro/Nanostructural Evolution by Photofluidic Motions of Azobenzene Materials. *Adv. Mater.* **2012**, *24*, 2069-2103.

(39) Li, J.; Wang, X. Y.; Liang, X. G. Modification of Nucleic Acids by Azobenzene Derivatives and Their Applications in Biotechnology and Nanotechnology. *Chemistry-an Asian Journal* **2014**, *9*, 3344-3358.

(40) Asanuma, H.; Liang, X.; Nishioka, H.; Matsunaga, D.; Liu, M.; Komiyama, M. Synthesis of azobenzene-tethered DNA for reversible photo-regulation of DNA functions: hybridization and transcription. *Nat. Protoc.* **2007**, *2*, 203-212.

(41) Liang, X. G.; Asanuma, H.; Kashida, H.; Takasu, A.; Sakamoto, T.; Kawai, G.; Komiyama, M. NMR study on the photoresponsive DNA tethering an azobenzene. Assignment of the absolute configuration of two diastereomers and structure determination of their duplexes in the trans-form. *J. Am. Chem. Soc.* **2003**, *125*, 16408-16415.

(42) Asanuma, H.; Ito, T.; Yoshida, T.; Liang, X. G.; Komiyama, M. Photoregulation of the formation and dissociation of a DNA duplex by using the cis-trans isomerization of azobenzene. *Angew. Chem. Int. Ed.* **1999**, *38*, 2393-2395.

(43) Asanuma, H.; Liang, X. G.; Yoshida, T.; Komiyama, M. Photocontrol of DNA duplex formation by using azobenzene-bearing oligonucleotides. *ChemBioChem* **2001**, *2*, 39-44.

(44) Nakasone, Y.; Ooi, H.; Kamiya, Y.; Asanuma, H.; Terazima, M. Dynamics of Inter-DNA Chain Interaction of Photoresponsive DNA. *J. Am. Chem. Soc.* **2016**, *138*, 9001-9004.

(45) Kamiya, Y.; Asanuma, H. Light-Driven DNA Nanomachine with a Photoresponsive Molecular Engine. *Acc. Chem. Res.* **2014**, *47*, 1663-1672.

(46) Liang, X.; Mochizuki, T.; Asanuma, H. A Supra-photoswitch Involving Sandwiched DNA Base Pairs and Azobenzenes for Light-Driven Nanostructures and Nanodevices. *Small* **2009**, *5*, 1761-1768.

(47) Phillips, J. A.; Liu, H.; O'Donoghue, M. B.; Xiong, X.; Wang, R.; You, M.; Sefah, K.; Tan, W. Using Azobenzene Incorporated DNA Aptamers to Probe Molecular Binding Interactions. *Bioconjugate Chem.* **2011**, *22*, 282-288.

(48) Yu, J. M.; Yang, L. R.; Liang, X. F.; Dong, T. T.; Liu, H. Z. Reversible regulation of thrombin adsorption and desorption based on photoresponsive-aptamer modified gold nanoparticles. *Talanta* **2015**, *144*, 312-317.

(49) Yan, Y.; Wang, X.; Chen, J. I. L.; Ginger, D. S. Photoisomerization Quantum Yield of Azobenzene-Modified DNA Depends on Local Sequence. *J. Am. Chem. Soc.* **2013**, *135*, 8382-8387.

(50) Yan, Y. Q.; Chen, J. I. L.; Ginger, D. S. Photoswitchable Oligonucleotide-Modified Gold Nanoparticles: Controlling Hybridization Stringency with Photon Dose. *Nano Lett.* **2012**, *12*, 2530-2536.

(51) Yan, Y. Q.; Samai, S.; Bischoff, K. L.; Zhang, J.; Ginger, D. S. Photocontrolled DNA Hybridization Stringency with Fluorescence Detection in Heterogeneous Assays. *ACS Sensors* **2016**, *1*, 566-571.

(52) Kim, Y. M.; Phillips, J. A.; Liu, H. P.; Kang, H. Z.; Tan, W. H. Using photons to manipulate enzyme inhibition by an azobenzene-modified nucleic acid probe. *Proc. Natl. Acad. Sci. U.S.A.* **2009**, *106*, 6489-6494.

(53) Liang, X. G.; Fujioka, K.; Asanuma, H. Nick Sealing by T4 DNA Ligase on a Modified DNA Template: Tethering a Functional Molecule on D-Threoninol. *Chemistry-A European Journal* **2011**, *17*, 10388-10396.

(54) You, M. X.; Wang, R. W.; Zhang, X. B.; Chen, Y.; Wang, K. L.; Peng, L.; Tan, W. H. Photon-Regulated DNA-Enzymatic Nanostructures by Molecular Assembly. *ACS Nano* **2011**, *5*, 10090-10095.

(55) Kang, H. Z.; Liu, H. P.; Zhang, X. L.; Yan, J. L.; Zhu, Z.; Peng, L.; Yang, H. H.; Kim, Y. M.; Tan, W. H. Photoresponsive DNA-Cross-Linked Hydrogels for Controllable Release and Cancer Therapy. *Langmuir* **2011**, *27*, 399-408.

(56) Kamiya, Y.; Takagi, T.; Ooi, H.; Ito, H.; Liang, X.; Asanuma, H. Synthetic Gene Involving Azobenzene-Tethered T7 Promoter for the Photocontrol of Gene Expression by Visible Light. *ACS Synth. Biol.* **2015**, *4*, 365-370.

(57) Matsunaga, D.; Asanuma, H.; Komiyama, M. Photoregulation of RNA digestion by RNase H with azobenzene-tethered DNA. *J. Am. Chem. Soc.* **2004**, *126*, 11452-11453.

(58) Yamazawa, A.; Liang, X. G.; Asanuma, H.; Komiyama, M. Photoregulation of the DNA polymerase reaction by oligonucleotides bearing an azobenzene. *Angew. Chem. Int. Ed.* **2000**, *39*, 2356-2357.

(59) Chen, J. I. L.; Chen, Y.; Ginger, D. S. Plasmonic Nanoparticle Dimers for Optical Sensing of DNA in Complex Media. *J. Am. Chem. Soc.* **2010**, *132*, 9600-9601.

(60) Chen, J. I. L.; Durkee, H.; Traxler, B.; Ginger, D. S. Optical Detection of Protein in Complex Media with Plasmonic Nanoparticle Dimers. *Small* **2011**, *7*, 1993-1997.

(61) Maye, M. M.; Kumara, M. T.; Nykypanchuk, D.; Sherman, W. B.; Gang, O. Switching binary states of nanoparticle superlattices and dimer clusters by DNA strands. *Nat. Nanotechnol.* **2010**, *5*, 116-120.

(62) Maye, M. M.; Nykypanchuk, D.; van der Lelie, D.; Gang, O. A simple method for kinetic control of DNA-induced nanoparticle assembly. *J. Am. Chem. Soc.* **2006**, *128*, 14020-14021.

(63) Nykypanchuk, D.; Maye, M. M.; van der Lelie, D.; Gang, O. DNA-guided crystallization of colloidal nanoparticles. *Nature* **2008**, *451*, 549-552.

(64) Kumar, A.; Hwang, J. H.; Kumar, S.; Nam, J. M. Tuning and assembling metal nanostructures with DNA. *Chem. Commun.* **2013**, *49*, 2597-2609.

(65) Hurst, S. J.; Lytton-Jean, A. K. R.; Mirkin, C. A. Maximizing DNA loading on a range of gold nanoparticle sizes. *Anal. Chem.* **2006**, *78*, 8313-8318.

(66) Elghanian, R.; Storhoff, J. J.; Mucic, R. C.; Letsinger, R. L.; Mirkin, C. A. Selective colorimetric detection of polynucleotides based on the distance-dependent optical properties of gold nanoparticles. *Science* **1997**, *277*, 1078-1081.

(67) Hill, H. D.; Millstone, J. E.; Banholzer, M. J.; Mirkin, C. A. The Role Radius of Curvature Plays in Thiolated Oligonucleotide Loading on Gold Nanoparticles. *ACS Nano* **2009**, *3*, 418-424.

(68) Mirkin, C. A.; Letsinger, R. L.; Mucic, R. C.; Storhoff, J. J. A DNA-based method for rationally assembling nanoparticles into macroscopic materials. *Nature* **1996**, *382*, 607-609.

(69) Rosi, N. L.; Mirkin, C. A. Nanostructures in biodiagnostics. *Chem. Rev.* **2005**, *105*, 1547-1562.

(70) Giljohann, D. A.; Seferos, D. S.; Daniel, W. L.; Massich, M. D.; Patel, P. C.; Mirkin, C. A. Gold Nanoparticles for Biology and Medicine. *Angew. Chem. Int. Ed.* **2010**, *49*, 3280-3294.

(71) Blum, A. P.; Kammeyer, J. K.; Rush, A. M.; Callmann, C. E.; Hahn, M. E.; Gianneschi, N. C. Stimuli-Responsive Nanomaterials for Biomedical Applications. *J. Am. Chem. Soc.* **2015**, *137*, 2140-2154.

(72) Pinheiro, A. V.; Han, D. R.; Shih, W. M.; Yan, H. Challenges and opportunities for structural DNA nanotechnology. *Nat. Nanotechnol.* **2011**, *6*, 763-772.

(73) Kuzyk, A.; Yang, Y.; Duan, X.; Stoll, S.; Govorov, A. O.; Sugiyama, H.; Endo, M.; Liu, N. A light-driven three-dimensional plasmonic nanosystem that translates molecular motion into reversible chiroptical function. *Nat. Commun.* **2016**, *7*, 10591.

(74) Schild, H. G. Poly (N-isopropylacrylamide) - Experiment, Theory and Application. *Prog. Polym. Sci.* **1992**, *17*, 163-249.

(75) Chiantore, O.; Guaita, M.; Trossarelli, L. Solution Properties Of Poly(N-Isopropylacrylamide). *Makromolekulare Chemie-Macromolecular Chemistry and Physics* **1979**, *180*, 969-973.

(76) Kubota, K.; Fujishige, S.; Ando, I. Solution Properties Of Poly(N-Isopropylacrylamide) In Water. *Polym. J.* **1990**, *22*, 15-20.

(77) Osa, M. Aqueous Solution Properties of Poly(N-isopropylacrylamide). *Kobunshi Ronbunshu* **2009**, *66*, 273-288.

(78) Karg, M.; Hellweg, T. New "smart" poly(NIPAM) microgels and nanoparticle microgel hybrids: Properties and advances in characterisation. *Current Opinion in Colloid & Interface Science* **2009**, *14*, 438-450.

(79) Karg, M.; Hellweg, T. Smart inorganic/organic hybrid microgels: Synthesis and characterisation. *J. Mater. Chem.* **2009**, *19*, 8714-8727.

(80) Pelton, R. Temperature-sensitive aqueous microgels. *Adv. Colloid Interface Sci.* **2000**, *85*, 1-33.

(81) Zhou, N.; Ni, J.; Yan, X. H.; Wang, Z. L.; Cheng, R. S. Synthesis and solution properties of single-chain microgels from poly(N-isopropylacrylamide) copolymer. *J. Appl. Polym. Sci.* **2003**, *89*, 2179-2183.

(82) Kawaguchi, H. Thermoresponsive microhydrogels: preparation, properties and applications. *Polym. Int.* **2014**, *63*, 925-932.

(83) Guan, Y.; Zhang, Y. J. PNIPAM microgels for biomedical applications: from dispersed particles to 3D assemblies. *Soft Matter* **2011**, *7*, 6375-6384.

(84) Wei, J. J.; Li, Y.; Ngai, T. Tailor-made microgel particles: Synthesis and characterization. *Colloids and Surfaces a-Physicochemical and Engineering Aspects* **2016**, *489*, 122-127.

(85) Roy, D.; Brooks, W. L. A.; Sumerlin, B. S. New directions in thermoresponsive polymers. *Chem. Soc. Rev.* **2013**, *42*, 7214-7243.

(86) Stuart, M. A. C.; Huck, W. T. S.; Genzer, J.; Muller, M.; Ober, C.; Stamm, M.; Sukhorukov, G. B.; Szleifer, I.; Tsukruk, V. V.; Urban, M.; Winnik, F.; Zauscher, S.; Luzinov, I.; Minko, S. Emerging applications of stimuli-responsive polymer materials. *Nat. Mater.* **2010**, *9*, 101-113.

(87) Islam, M. R.; Ahiabu, A.; Li, X.; Serpe, M. J. Poly (N-isopropylacrylamide) Microgel-Based Optical Devices for Sensing and Biosensing. *Sensors* **2014**, *14*, 8984-8995.

(88) Begum, R.; Naseem, K.; Farooqi, Z. H. A review of responsive hybrid microgels fabricated with silver nanoparticles: synthesis, classification, characterization and applications. *J. Sol-Gel Sci. Technol.* **2016**, *77*, 497-515.

(89) Lim, S.; Song, J. E.; La, J. A.; Cho, E. C. Gold Nanospheres Assembled on Hydrogel Colloids Display a Wide Range of Thermoreversible Changes in Optical Bandwidth for Various Plasmonic-Based Color Switches. *Chem. Mater.* **2014**, *26*, 3272-3279.

(90) Fernandez-Lopez, C.; Polavarapu, L.; Solis, D. M.; Taboada, J. M.; Obelleiro, F.; Contreras-Caceres, R.; Pastoriza-Santos, I.; Perez-Juste, J. Gold Nanorod-pNIPAM Hybrids with Reversible Plasmon Coupling: Synthesis, Modeling, and SERS Properties. *ACS Appl. Mater. Interfaces* **2015**, *7*, 12530-12538.

Chapter 3. EFFECT OF TEMPERATURE ON PHOTOISOMERIZATION QUANTUM YIELDS FOR AZOBENZENE-MODIFIED DNA

This chapter is mostly adapted from the original publication "Temperature Dependent Photoisomerization Quantum Yields for Azobenzene-modified DNA", Soumyadyuti Samai, Dakoda J. Bradley, Tina Lok Yee Choi, Yunqi Yan, David S. Ginger, *J. Phys. Chem. C*, **2017**, *121* (12), 6997–7004**, DOI:** 10.1021/acs.jpcc.6b12241.

3.1 OVERVIEW

In this chapter, we study the photoisomerization quantum yield of azobenzene-modified DNA as a function of temperature for various DNA sequences. We find that even though the photoisomerization quantum yield of free azobenzene is essentially temperature independent, the *trans*-to-*cis* photoisomerization quantum yield depends strongly on temperature when the azobenzene is incorporated into DNA. We show that this temperature dependence is DNA-sequence dependent, and closely linked to the melting temperature of the host DNA. While the *trans*-to-*cis* isomerization quantum yield is sequence and temperature dependent, in contrast, the thermal *cis*-to-*trans* isomerization of azobenzene embedded in DNA is sequence-independent, exhibits an Arrhenius-like behavior and follows a first order kinetics. These results provide an understanding of the azobenzene isomerization mechanisms in DNA sequences to enable more efficient design of optically re-programmable nanomaterials and biosensors.

3.2 INTRODUCTION

Nucleic acids are now extensively used to design, tailor, and assemble nanomaterials[1] ranging from Mirkin-type spherical nucleic acids,[2-4] to functional aptamers,[5-8] DNA origami,[9-12]

and nanomachines.[13-15] The ability to incorporate molecular photoswitches into synthetic DNA, sequences, such as azobenzene attached to the sugar-phosphate backbone during solid phase DNA synthesis, as pioneered by Asanuma et al[34], has opened up new possibilities for stimulus-responsive materials in these fields,[12,16-25] while at the same time enabling applications such as photoregulation of gene expression[26-28] and enzymatic reactions,[29-31] and also facilitating studies of aptamer folding and target binding.[32,33]

Importantly, the performance of these applications depends sensitively on photophysical properties of the azobenzene, such as its photoisomerization quantum yield, and the reverse thermal isomerization rate. While the photophysics of azobenzene isomerization and its applications as a molecular photoswitch have been well-studied,[40-42] the effects of incorporating azobenzene into DNA sequences on photoisomerization have received much less attention, despite the observation that the DNA environment can have a profound effect on the azobenzene properties[43-46] – and that these interactions are in fact critical to enabling some applications, such as photo-controlled DNA hybridization stringency.[39,47]

Here, we study the variation of the *trans*-to-*cis* photoswitch quantum yield, and reverse thermal *cis*-to-*trans* isomerization of azobenzene with temperature and DNA sequence. We find that the photoisomerization quantum yield for different DNA sequences increases with temperature -- a behavior distinct from that of the free azobenzene in solution – and converges to similar values when the temperature is above the melting temperature of the sequences. We also show that the *cis*-to-*trans* thermal isomerization of azobenzenes attached to the DNA backbone is slower compared to the free azobenzene, even though the activation energy is nearly the same for both the systems. These results are not only useful in the advancement of bionanotechnology, but

also provide an insight into the different isomerization mechanisms of azobenzene when inserted into DNA sequence.

3.3 *TRANS*-TO-*CIS* PHOTOISOMERIZATION QUANTUM YIELD MEASUREMENTS FOR AZOBENZENE-MODIFIED DNA SEQUENCES

Figure 3.1(a) depicts the reversible photoisomerization of azobenzene incorporated into a DNA strand through a D-threoninol linkage. The azobenzene moiety photoisomerizes from *trans*-to-*cis* configuration under UV illumination and undergoes *cis*-to-*trans* reverse isomerization on exposure to visible light (or via slower thermal activation). Figure 3.1(b) shows the change in the UV-Vis absorption spectrum of the azobenzene connected to DNA following excitation with 330 nm UV light. Figure 3.1(c) shows our basic experimental approach to measure the temperature-dependent quantum yield of azobenzene photoisomerization in various DNA sequences (see Table 1 for sequence details). Briefly, we measure the UV-Vis spectrum of azobenzene as a function of UV illumination time for samples at varying temperatures and calculate the ratio of *cis* to *trans*-azobenzene to construct classic photokinetic curves.[44] It is clear that the 330 nm UV light is only absorbed by the azobenzene but not by the DNA bases (Figure 3.1(b)).

Figure 3.2 shows a series of photokinetic curves plotting the fraction of *cis*-azobenzene as a function of integrated photokinetic factor (IPF) that we use to extract the photoisomerization quantum yields for different DNA sequences at temperatures ranging from 27°C to 85°C (data for 75°C and 85°C are not shown). These plots account for the changing absorption spectrum of the azobenzene over time, allowing us to fit the data according to equation 1[44,45]

$$y_t = (y_0 - y_\infty)\ \exp(-Ax) + y_\infty \qquad (1)$$

where y_0, y_t and y_∞ denote the initial fraction of *cis*-azobenzene at time $t = 0$, at a later time t during UV illumination and at the final photostationary state i.e., at long time ($t = \infty$) respectively; x is the integrated photokinetic factor (IPF),[44] which rationalizes the change in the absorbance of the solution during the photoconversion process by transforming the UV irradiation time into photon doses; A is a pre-factor that relates to the *trans*-to-*cis* photoisomerization quantum yield (ϕ_{trans}) at 330 nm (see Appendix A). This equation neglects the reverse *cis*-to-*trans* thermal isomerization of azobenzene for photoisomerization quantum yield calculation, which is a valid assumption under the experimental conditions we use (see Appendix A for discussion).

Table 3.1. List of the azobenzene-modified DNA sequences used to measure *trans*-to-*cis* photoisomerization quantum yields and the measured activation energies for *cis*-to-*trans* thermal isomerization (E_a)

Sequence name	Sequence	T_m (°C) †	E_a (kJ/mol)
ssDNA	5' – AGACTGAAC**X**CAATGTATG – 3' **X**: *trans*-azobenzene	-	90.0 ± 2.47
PM (Perfect Matched)	5' – AGACTGAAC**X**CAATGTATG – 3' 3' – TCTGACTTG GTTACATAC – 5'	61	86.8 ± 2.42
PM-abasic	5' – AGACTGAAC**X**CAATGTATG – 3' 3 '– TCTGACTTG*Y*GTTACATAC – 5' *Y*: abasic site	59	89.1 ± 2.34
mm1A	5' – AGACTGAAC**X***C*AATGTATG – 3' 3' – TCTGACTTG *A*TTACATAC – 5'	48	89.1 ± 2.36
mm1C	5' – AGACTGAAC**X***C*AATGTATG – 3' 3' – TCTGACTTG *C*TTACATAC – 5'	47	-
mm1T	5' – AGACTGAAC**X***C*AATGTATG – 3' 3' – TCTGACTTG *T*TTACATAC – 5'	49	-
mm2	5' – AGACTGAAC**X**C*A*ATGTATG – 3' 3' – TCTGACTTG G*C*TACATAC – 5'	51	-
mm3	5' – AGACTGAAC**X**CA*A*TGTATG – 3' 3' – TCTGACTTG GT*G*ACATAC – 5'	55	-

† Melting temperature of the DNA sequences

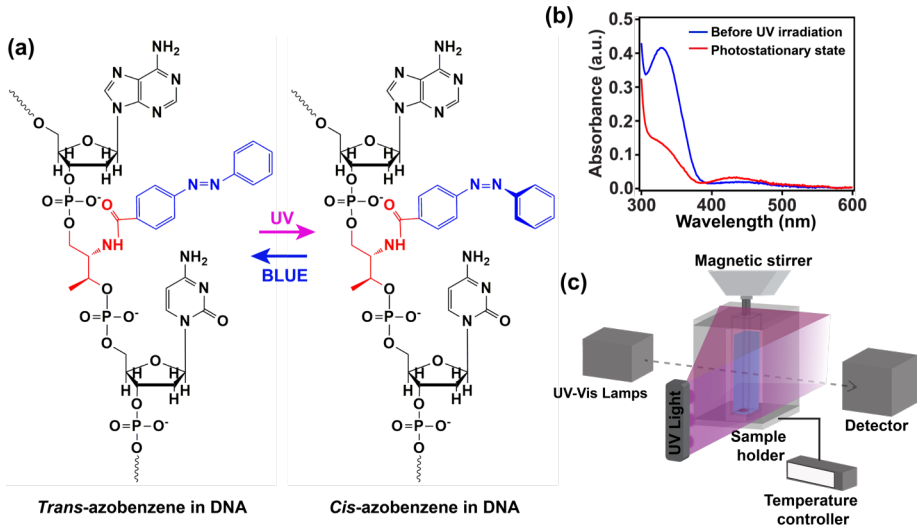

Figure 3.1 Reversible photoisomerization of azobenzene-modified DNA. (a) The azobenzene molecule (blue) is inserted to the DNA strand via a D-threoninol molecule (red) as a linker. (b) UV-Vis absorbance spectra of the azobenzene molecule embedded to the DNA backbone before UV irradiation (blue curve) and at the photostationary state (red curve). (c) Schematic of the experimental set up for measuring the photoisomerization quantum yields at different temperatures using UV-Vis spectroscopy system.

3.4 TEMPERATURE-DEPENDENT *TRANS*-TO-*CIS* PHOTOISOMERIZATION QUANTUM YIELDS FOR AZOBENZENE-MODIFIED DNA SEQUENCES

Figure 3.2 (a) plots the photokinetic curves for free azobenzene in isooctane at varying temperatures, which shows a nearly temperature-independent quantum yield of (11.3 ± 0.265)%, in good agreement with previous reports.[45] Figure 3.2 (b) plots the photokinetic curves for a 18-base-pair sequence of perfectly complementary double stranded (ds) DNA with a single azobenzene molecule in the middle of the sequence (see Table 3.1). In contrast to the free azobenzene data in Figure 3.2 (a), the data for the azobenzene attached to dsDNA in Figure 3.2 (b) show a striking temperature dependence. Notably, the fraction of *cis*-azobenzene at the photostationary state, and the photoisomerization quantum yield, both increase dramatically with temperature.

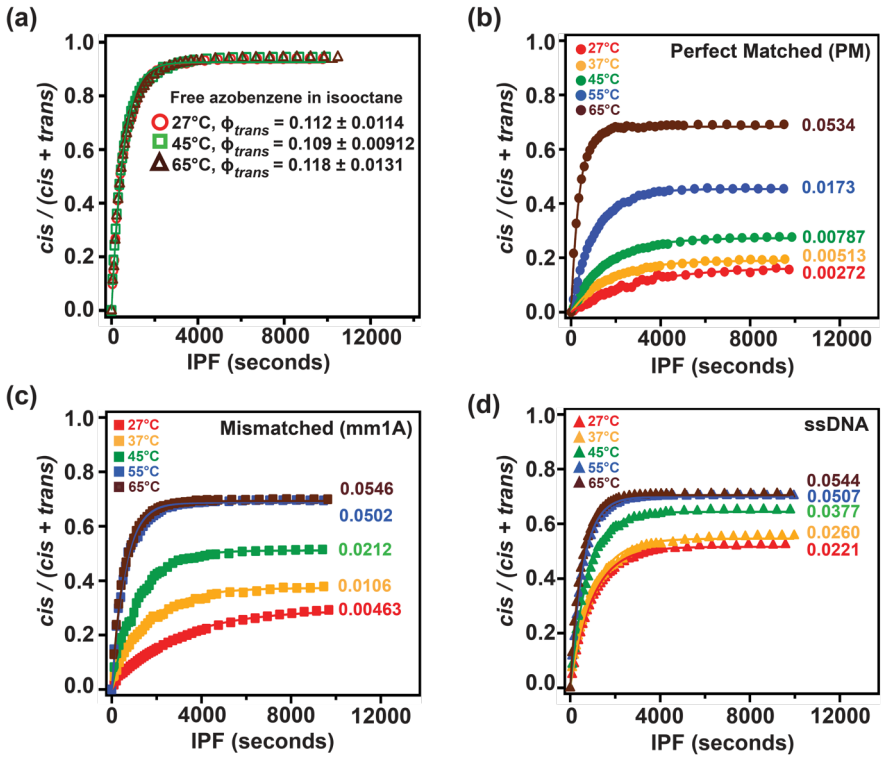

Figure 3.2 Photokinetic curves for free azobenzene and azobenzene-modified DNAs at different temperatures**.** Plots of the fraction of *cis*-azobenzene as a function of integrated photokinetic factor (IPF) for: (a) free azobenzene in isooctane; (b) 18-base-pair long dsDNA sequence bearing an azobenzene at the center of the sequence with perfect complementarity; (c) the same sequence with a single non-complementary base pair (C-A) next to the azobenzene in the sequence; and (d) the single stranded azobenzene-modified DNA without its complement at different temperatures. The red, yellow, green, blue and brown solid traces are the fits using the equation (1) to experimental data at 27°C, 37°C, 45°C, 55°C, and 65°C, respectively. The average values of the *trans*-to-*cis* photoisomerization quantum yields (Φ_{trans}) at 330 nm are obtained from three identical experiments and are reported next to the respective fits (the uncertainties in these values are reported in Table S1 in Appendix A).

We investigate the origin of this temperature-dependence of the photoisomerization quantum yield by studying different double and single-stranded azobenzene-modified DNA sequences. Previous research has shown that even single-base mismatches near the location of the azobenzene attachment site can significantly increase the quantum yield of the azobenzene.[38] To explore this effect in depth, Figure 3.2 (c) shows the photokinetic curves at different temperatures for the dsDNA sequence mm1A which has a non-complementary base pair (C-A) located adjacent

to the azobenzene. The same set of photokinetic curves for azobenzene incorporated into the same *single* stranded DNA sequence, without its complement are shown in Figure 3.2 (d). Figure 3.2 (c-d) show that, like the perfect matched dsDNA sequence shown in Figure 3.2 (b), both the partially mismatched sequence and ssDNA exhibit an increase in the photoisomerization quantum yield with temperature. Interestingly, compared to the perfectly complementary sequence, the photoisomerization quantum yield of azobenzene in ssDNA displays a gradual temperature dependence, while for the *mismatched* double stranded DNA sequence mm1A the temperature dependence lies in between the two.

3.5 Effect of Nearby DNA Sequence Mismatch on Temperature-Dependence of Azobenzene Photoisomerization Quantum Yields

Observing this interesting temperature-dependent behavior in the presence of a mismatched base pair, we looked at a number of partially mismatched dsDNA sequences (see Table 3.1) to investigate the effect of sequence non-complementarity on the temperature dependence of azobenzene photoisomerization quantum yield (Figure S1 in Appendix A). We measure the quantum yield as a function of temperature for these sequences and plot them in Figure 3.3 (a). The data in Figure 3.3 (a) indicate that the temperature dependency of photoisomerization quantum yield varies slightly among different DNA sequences. We observe the largest increment in the quantum yield values between 45°C and 55°C for azobenzenes in the mismatched dsDNA sequences, while the quantum yields for the perfectly complementary dsDNA sequences show the largest change in between 55°C and 65°C. Overlaying the melting temperature (T_m) values for these sequences with the quantum yield curves (Figure 3.3 (a)) shows that the maximum change in the quantum yield happens near the melting temperature for each sequence.

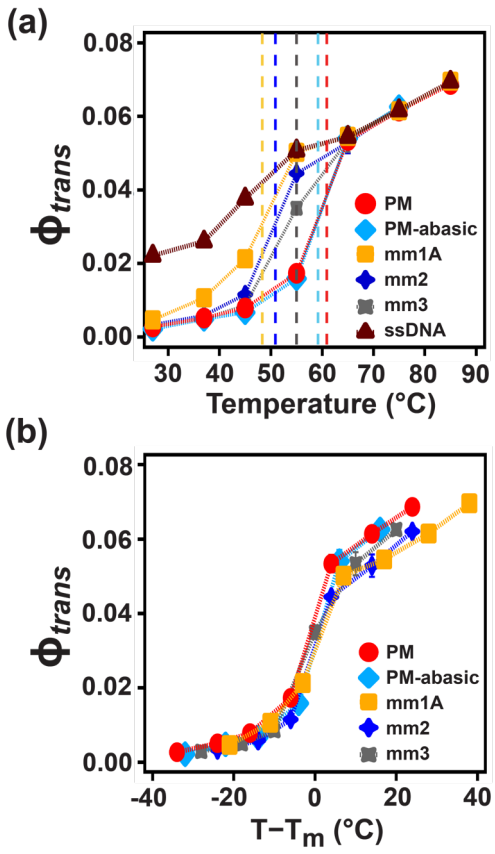

Figure 3.3 Variation of temperature-dependent photoisomerization quantum yields of azobenzene with nearby DNA sequence. (a) Plot of azobenzene photoisomerization quantum yields (ϕ_{trans}) as a function of the solution temperature (T) for sequences PM, PM-abasic, mm1A, mm2, mm3 and ssDNA. As the position of the mismatched base pair changes, the shape of the curve changes, which appears to correlate with the DNA melting temperature (T_m). The vertical dashed lines denote T_m of the sequences: red, aqua, yellow, blue and grey for sequences PM, PM-abasic, mm1A, mm2 and mm3 respectively. (b) Plot of the quantum yields (ϕ_{trans}) of the dsDNA sequences as a function of the difference between the solution temperature and the melting temperature of the corresponding dsDNA sequence i.e. ($T-T_m$), which indicates that the trends are dominated by the melting transition of the sequences. The largest increment of the quantum yield was observed near the T_m of the sequence beyond which all the sequences show nearly same quantum yield and identical dependence on T.

Noting that ssDNA exhibits a weaker temperature dependent quantum yield than dsDNA, and noting that the maximum rise of the quantum yield of the dsDNA appears to correlate with T_m, we replot the data in Figure 3.3(a) as a function of $T-T_m$ in Figure 3.3(b). We note that, when adjusted relative to T_m, the data in Figure 3.3(b) all collapse to a single curve indicating that the

melting transition dominates the temperature dependence. Interestingly, once $T > T_m$ the temperature dependence for all sequences has the same slope as the ssDNA: these sequences are similar enough that the temperature dependence of the quantum yield is essentially that of the identical ssDNA above T_m. Because of our focus on dsDNA here, we did not explore the temperature dependence of an extensive series of azobenzene-modified ssDNAs, but we note that previous work has identified that the azobenzene quantum yield in ssDNA is sensitive to the structural rigidity of the ssDNA.[38] So we suspect that a wider range of ssDNA sequences might exhibit differences in the temperature dependence of the incorporated azobenzene quantum yield, especially if the ssDNAs show different local stiffness.[39] Nevertheless, we expect that such variations would be smaller than the variations between the dsDNAs around T_m.

3.6 *CIS*-TO-*TRANS* REVERSE THERMAL ISOMERIZATION OF AZOBENZENE-MODIFIED DNA SEQUENCES

Finally, we turn to probe the thermal *cis*-to-*trans* isomerization of azobenzene in the DNA sequences at different temperatures. To our knowledge, the effect of the nearby DNA base pairs on the reverse thermal isomerization has not been reported, despite the fact that the thermal stability of the *cis*-form of azobenzene largely dictates the stability or the half-life of photoswitched DNA-based nanomaterials for a broad range of applications.

In order to measure the reverse isomerization kinetics as a function of DNA sequences and temperature we first exposed the azobenzene-modified DNA solution to 330 nm UV irradiation until the *trans*-to-*cis* photoreaction reached the photostationary state, typically for a period of two hours for every temperature. After turning off the UV light source we monitored the rise in the absorbance at 330 nm in dark to measure the change in the *cis*-azobenzene concentration with time. During these measurements, we took care to work under conditions so that exposure to the

light from the UV-Vis spectrometer did not induce any significant reverse photoisomerization in the solution (Figure S2 in Appendix A). This precaution is especially important to measure the kinetics at low temperatures. During reverse thermal isomerization, we then calculated the ratio of the fraction of *cis*-azobenzene at different times (y), to the initial fraction of *cis*-azobenzene (y_0) (with y_0 now determined at the photostationary state).

Figure 3.4 (a) plots $\ln(y/y_0)$ as a function of time for the perfectly complementary (PM and PM-abasic) and mismatched (mm1A) double stranded DNAs along with that for the ssDNA at various temperature ranging from 37°C-75°C. We observe that the temperature dependence and the overall isomerization rate for the different dsDNA sequences are nearly identical regardless of temperature. As a result, we conclude that presence of a non-complementary base pair adjacent to the azobenzene or an abasic site directly across from it does not affect the thermal isomerization of the *cis*-azobenzene at any temperature. This behavior stands in strong contrast to the temperature- and sequence-dependent nature of the forward *trans*-to-*cis* photoisomerization quantum yield of azobenzene.

The high degree of linearity in Figure 3.4 (a) indicates that the thermal back reaction of *cis*-azobenzene to the *trans* form in different DNA sequences follows first order kinetics, just like the free azobenzene in solution. We extract the rate constants for the *cis*-to-*trans* thermal isomerization process (k_{therm}) from the slope of the straight lines for the DNA sequences shown in the Figure 3.4 (a). We then use these k_{therm} values to generate an Arrhenius plot, which we show as Figure 3.4 (b). The data are all linear on the Arrhenius plot, and from the fits in Figure 3.4(b) we thus obtain the activation energies (E_a) of the thermal isomerization process for azobenzene-modified DNAs (Table 3.1). Consistent with the plots in Figure 3.4(a), the activation energy for the thermal isomerization of azobenzene and the half-life of the *cis* isomer is the same in each of

the DNA sequences (Table S1 in Appendix A). We obtain an average value for the thermal activation energy of *cis*-to-*trans* isomerization of azobenzene as (88.8 ± 0.693) kJ/mol. For comparison, we also measured the rate constants for thermal isomerization of free azobenzene in isooctane under the same experimental conditions using the same procedures and apparatus. Our measurement for the thermal activation energy of free azobenzene yields E_a = (86.1 ± 3.78) kJ/mol, which is in good agreement with earlier reports.[46-48] Interestingly, with the DNA and free azobenzene results in agreement to within 3%, we conclude that the E_a value for reverse thermal isomerization changes little if any, due to attachment to the DNA.

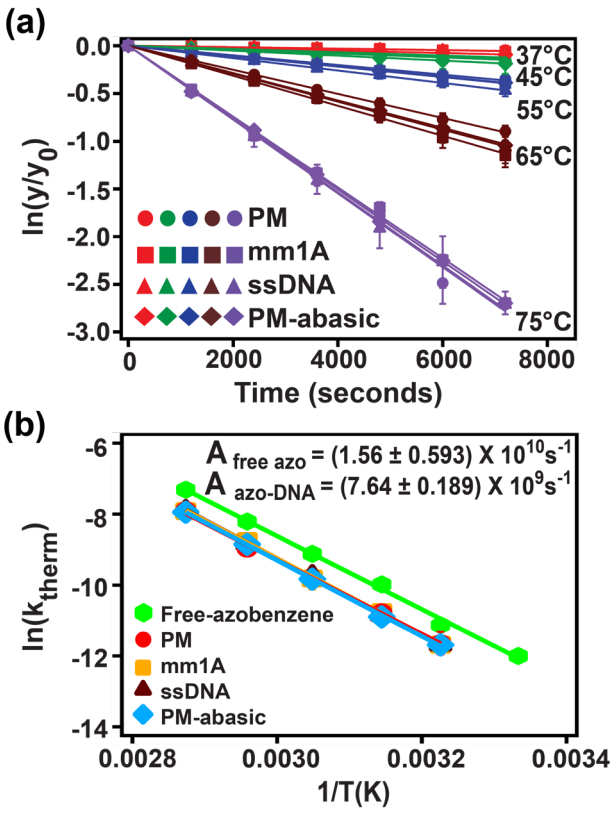

Figure 3.4 Effect of DNA sequence on *cis*-to-*trans* reverse thermal isomerization of azobenzene. (a) Plot of logarithm of the ratio between the fraction of *cis*-azobenzene (y) at different times during reverse thermal isomerization and the initial fraction of *cis*-azobenzene (y_0) versus time, showing first order kinetics of the thermal conversion of *cis*-azobenzene to *trans*-azobenzene for sequences PM (circles), mm1A (squares), ssDNA (triangles) and PM-abasic (diamonds) at 37°C (red), 45°C (green), 55°C (blue), 65°C (brown) and 75°C (purple). The rate constants do not vary among these sequences so many symbols overlap. (b) Arrhenius plots of the same set of sequences and free azobenzene in isooctane give similar activation energies (slope of the straight lines) for the *cis*-to-*trans* thermal isomerization. The average value of the pre-exponential factor of azobenzene in the DNA sequences ($A_{\text{azo-DNA}}$) is $(7.64 \pm 0.189)\times10^{9}$ s^{-1} while for free azobenzene ($A_{\text{free azo}}$) the value is $(1.56 \pm 0.593)\times10^{10}$ s^{-1}.

However, closer examination of Figure 3.4 (b) and Table 3.1 reveals that even though the activation energy for the *cis*-to-*trans* thermal isomerization of free azobenzene is very similar to the azobenzenes anchored to the DNA backbones, the first order rate constants for the azobenzenes bound to DNA sequences are measurably lower than those for the free azobenzene isomerization (Figure S3 (a) in Appendix A). From the Arrhenius plots, we can conclude that the variation occurs

due to the pre-exponential factors for azobenzene thermal isomerization, suggesting that the frequency factor decreases due to either the attachment to the DNA backbone, or due to the change between isooctane and water as a solvent, or a combination of both effects.[49,50]

3.7 *TRANS*-TO-*CIS* ISOMERIZATION MECHANISMS OF AZOBENZENE-MODIFIED DNA

We next discuss both the sequence-dependence of the photoisomerization quantum yield, and sequence-independence of the thermal back reaction rates in terms of the known mechanisms of azobenzene isomerization. The photophysics of azobenzene photoisomerization are well-studied, yet complex. The forward *trans*-to-*cis* isomerization was originally thought to proceed via a rotation,[35,51-54] whereas recent experiments suggest that a hula-twist mechanism[55] may be more probable for free azobenzenes, and yet other evidences suggest that some substituted azobenzenes may still prefer rotation,[35] while high-level theory confirms that the potential energy surface is complicated.[51,53,56] Nevertheless, both the rotation and hula-twist require more free volume than inversion, and the forward *trans*-to-*cis* isomerization of azobenzene is known from experiments to be sensitive to the local environment.[38,39,57,58] Our observation of a temperature- and sequence-dependent photoisomerization quantum yield for azobenzene anchored to different DNA sequences agrees well with these models as the neighboring base pairs in a DNA duplex likely hinder the twisting motion of the phenyl ring around the N═N bond during photoisomerization, leading to a sequence-specific reduction in quantum yield for azobenzene in dsDNA.[38,39] At higher temperatures, when the dsDNA sequences start to melt to ssDNA, the reduction in steric hindrance to the rotational motion increases the photoisomerization efficiency. The greater thermal motion of the adjacent nucleobases at elevated temperature also creates more

free space around the azobenzene and accelerates the rotation, which can explain the increase in quantum yield of azobenzene in ssDNA with temperature.

The inversion mechanism, in contrast, is consistent with the sequence-independent nature of the reverse thermal isomerization[47,59-61], where one N═N─C bond angle in the azobenzene molecule changes along a plane keeping the C─N═N─C dihedral angle constant and the movement is not inhibited by the adjoining base pairs. Another possibility that could explain the sequence-independence of the reverse thermal isomerization is that the *cis* isomer may be creating its own free volume that minimizes sequence effects. In other words, it is possible that photoconversion of the *trans*-azobenzene to the non-planar *cis* isomer can result in partial dehybridization of the adjacent base pairs in the dsDNA[62,63] without complete dehybridization of the entire strand,[40,41,64] and that this local destabilization of the duplex creates additional volume, or freedom for fluctuational motion[39] around the azobenzene that blinds the azobenzene to the local sequence effects. Either explanation, or perhaps both in concert, would be consistent with the experimentally observed sequence-independent nature of the reverse thermal isomerization.

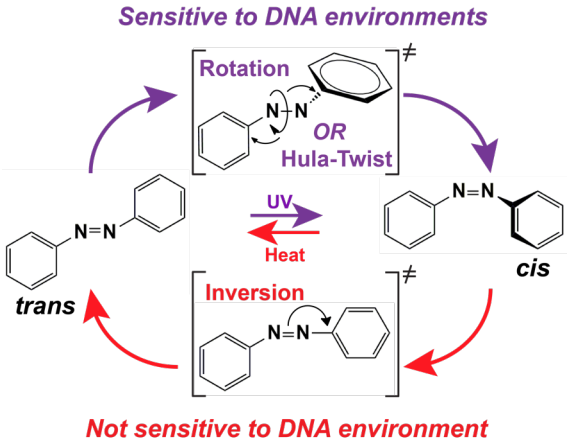

Figure 3.5 Schematic representation of probable isomerization mechanisms of azobenzene-modified DNA. Rotational and/or hula-twist mechanism of the *trans*-to-*cis* photoisomerization and the inversion mechanism of the *cis*-to-*trans* thermal isomerization of azobenzene. In the rotational pathway, the phenyl ring follows a torsional motion around the N─N bond while in the inversion mechanism the N═N─C bond angle changes along a plane. In the hula twist mechanism, the rotation of the phenyl ring is accompanied with a significant change in the N═N─C bond angle.

3.8 CONCLUSIONS

We have determined that the *trans*-to-*cis* photoisomerization quantum yield of azobenzene inserted into different DNA sequences is sensitive both to sequence and temperature, and that the main factor controlling the temperature dependence of the azobenzene quantum yield is the DNA melting transition, which provides a significant increase in flexibility and free volume to the azobenzene as one approaches, then passes through the melting transition.

Despite the fact that the neighboring DNA sequence plays an important role in the photoconversion efficiency of *trans*-azobenzene into its *cis* configuration, we find that the activation energy for the reverse thermal isomerization of azobenzene from *cis*-to-*trans* conformation is independent of the nature of the DNA sequence. These results are consistent with the generally accepted picture for azobenzene isomerization—whereby the forward photoisomerization involves a broader motion (e.g. rotation or hula-twist), which can be hindered

by the local environment, but the thermal reverse process occurs through an inversion, perhaps in a locally dehybridized pocket, which would be expected to be less sensitive to the local free volume. These results not only provide fundamental insights into the behavior of azobenzene linked to DNA, but also serve as detailed design rules for optimizing the performance of photoswitchable DNA in applications as diverse as nanomaterials assembly, molecular machines, and optical control of gene expression.

3.9 APPENDIX A

Experimental Methods, Supplementary texts and figures

3.10 ACKNOWLEDGEMENTS

This publication is based primarily on research supported by AFOSR (FA9550-14-1-02509). S.S. acknowledges Mark Ziffer for his valuable input in writing the Python script to obtain the photoisomerization quantum yields of azobenzene-modified DNAs. D.S.G. acknowledges the Alvin L. and Verla R. Kwiram endowed fund for partial support.

3.11 REFERENCES

(1) Estephan, Z. G.; Qian, Z. X.; Lee, D.; Crocker, J. C.; Park, S. J. Responsive Multidomain Free-Standing Films of Gold Nanoparticles Assembled by DNA-Directed Layer-by-Layer Approach. *Nano Lett.* **2013**, *13*, 4449-4455.

(2) Cutler, J. I.; Auyeung, E.; Mirkin, C. A. Spherical Nucleic Acids. *J. Am. Chem. Soc.* **2012**, *134*, 1376-1391.

(3) Jensen, S. A.; Day, E. S.; Ko, C. H.; Hurley, L. A.; Luciano, J. P.; Kouri, F. M.; Merkel, T. J.; Luthi, A. J.; Patel, P. C.; Cutler, J. I.; Daniel, W. L.; Scott, A. W.; Rotz, M. W.; Meade, T. J.; Giljohann, D. A.; Mirkin, C. A.; Stegh, A. H. Spherical Nucleic Acid Nanoparticle Conjugates as an RNAi-Based Therapy for Glioblastoma. *Sci. Transl. Med.* **2013**, *5,* 209ra152-209ra152.

(4) Zheng, D.; Giljohann, D. A.; Chen, D. L.; Massich, M. D.; Wang, X. Q.; Iordanov, H.; Mirkin, C. A.; Paller, A. S. Topical delivery of siRNA-based spherical nucleic acid nanoparticle conjugates for gene regulation. *Proc. Natl. Acad. Sci. U. S. A.* **2012**, *109*, 11975-11980.

(5) Jayasena, S. D. Aptamers: An emerging class of molecules that rival antibodies in diagnostics. *Clin. Chem.* **1999**, *45*, 1628-1650.

(6) Liu, J. W.; Cao, Z. H.; Lu, Y. Functional Nucleic Acid Sensors. *Chem. Rev.* **2009**, *109*, 1948-1998.

(7) Hermann, T.; Patel, D. J. Biochemistry - Adaptive recognition by nucleic acid aptamers. *Science* **2000**, *287*, 820-825.

(8) Tombelli, S.; Minunni, M.; Mascini, A. Analytical applications of aptamers. *Biosens. Bioelectron.* **2005**, *20*, 2424-2434.

(9) Pinheiro, A. V.; Han, D. R.; Shih, W. M.; Yan, H. Challenges and opportunities for structural DNA nanotechnology. *Nat. Nanotechnol.* **2011**, *6*, 763-772.

(10) Torring, T.; Voigt, N. V.; Nangreave, J.; Yan, H.; Gothelf, K. V. DNA origami: a quantum leap for self-assembly of complex structures. *Chem. Soc. Rev.* **2011**, *40*, 5636-5646.

(11) Han, D. R.; Pal, S.; Nangreave, J.; Deng, Z. T.; Liu, Y.; Yan, H. DNA Origami with Complex Curvatures in Three-Dimensional Space. *Science* **2011**, *332*, 342-346.

(12) Kuzyk, A.; Schreiber, R.; Fan, Z.; Pardatscher, G.; Roller, E.-M.; Hoegele, A.; Simmel, F. C.; Govorov, A. O.; Liedl, T. DNA-based self-assembly of chiral plasmonic nanostructures with tailored optical response. *Nature* **2012**, *483*, 311-314.

(13) Modi, S.; Swetha, M. G.; Goswami, D.; Gupta, G. D.; Mayor, S.; Krishnan, Y. A DNA nanomachine that maps spatial and temporal pH changes inside living cells. *Nat. Nanotechnol.* **2009**, *4*, 325-330.

(14) Surana, S.; Bhat, J. M.; Koushika, S. P.; Krishnan, Y. An autonomous DNA nanomachine maps spatiotemporal pH changes in a multicellular living organism. *Nat. Commun.* **2011**, *2,* 1-7.

(15) Zhang, F.; Nangreave, J.; Liu, Y.; Yan, H. Structural DNA Nanotechnology: State of the Art and Future Perspective. *J. Am. Chem. Soc.* **2014**, *136*, 11198-11211.

(16) Blum, A. P.; Kammeyer, J. K.; Rush, A. M.; Callmann, C. E.; Hahn, M. E.; Gianneschi, N. C. Stimuli-Responsive Nanomaterials for Biomedical Applications. *J. Am. Chem. Soc.* **2015**, *137*, 2140-2154.

(17) Kamiya, Y.; Asanuma, H. Light-Driven DNA Nanomachine with a Photoresponsive Molecular Engine. *Acc. Chem. Res.* **2014**, *47*, 1663-1672.

(18) Liang, X. G.; Nishioka, H.; Takenaka, N.; Asanuma, H. A DNA nanomachine powered by light irradiation. *ChemBioChem* **2008**, *9*, 702-705.

(19) Zhou, M. G.; Liang, X. G.; Mochizuki, T.; Asanuma, H. A Light-Driven DNA Nanomachine for the Efficient Photoswitching of RNA Digestion. *Angew. Chem. Int. Ed.* **2010**, *49*, 2167-2170.

(20) Kuzyk, A.; Yang, Y. Y.; Duan, X.; Stoll, S.; Govorov, A. O.; Sugiyama, H.; Endo, M.; Liu, N. A light-driven three-dimensional plasmonic nanosystem that translates molecular motion into reversible chiroptical function. *Nat. Commun.* **2016**, *7*, 1-6.

(21) Kang, H. Z.; Liu, H. P.; Phillips, J. A.; Cao, Z. H.; Kim, Y.; Chen, Y.; Yang, Z. Y.; Li, J. W.; Tan, W. H. Single-DNA Molecule Nanomotor Regulated by Photons. *Nano Lett.* **2009**, *9*, 2690-2696.

(22) Yang, Y. Y.; Goetzfried, M. A.; Hidaka, K.; You, M. X.; Tan, W. H.; Sugiyama, H.; Endo, M. Direct Visualization of Walking Motions of Photocontrolled Nanomachine on the DNA Nanostructure. *Nano Lett.* **2015**, *15*, 6672-6676.

(23) Yuan, Q.; Zhang, Y.; Chen, Y.; Wang, R.; Du, C.; Yasun, E.; Tan, W. Using silver nanowire antennas to enhance the conversion efficiency of photoresponsive DNA nanomotors. *Proc. Natl. Acad. Sci. U. S. A.* **2011**, *108*, 9331-9336.

(24) Endo, M.; Yang, Y.; Suzuki, Y.; Hidaka, K.; Sugiyama, H. Single-Molecule Visualization of the Hybridization and Dissociation of Photoresponsive Oligonucleotides and Their Reversible Switching Behavior in a DNA Nanostructure. *Angew. Chem. Int. Ed.* **2012**, *51*, 10518-10522.

(25) Yang, Y. Y.; Endo, M.; Hidaka, K.; Sugiyama, H. Photo-Controllable DNA Origami Nanostructures Assembling into Predesigned Multiorientational Patterns. *J. Am. Chem. Soc.* **2012**, *134*, 20645-20653.

(26) Yamazawa, A.; Liang, X. G.; Asanuma, H.; Komiyama, M. Photoregulation of the DNA polymerase reaction by oligonucleotides bearing an azobenzene. *Angew. Chem. Int. Ed.* **2000**, *39*, 2356-2357.

(27) Matsunaga, D.; Asanuma, H.; Komiyama, M. Photoregulation of RNA digestion by RNase H with azobenzene-tethered DNA. *J. Am. Chem. Soc.* **2004**, *126*, 11452-11453.

(28) Kamiya, Y.; Takagi, T.; Ooi, H.; Ito, H.; Liang, X.; Asanuma, H. Synthetic Gene Involving Azobenzene-Tethered T7 Promoter for the Photocontrol of Gene Expression by Visible Light. *ACS Synth. Biol.* **2015**, *4*, 365-370.

(29) Kim, Y. M.; Phillips, J. A.; Liu, H. P.; Kang, H. Z.; Tan, W. H. Using photons to manipulate enzyme inhibition by an azobenzene-modified nucleic acid probe. *Proc. Natl. Acad. Sci. U. S. A.* **2009**, *106*, 6489-6494.

(30) Liang, X. G.; Fujioka, K.; Asanuma, H. Nick Sealing by T4 DNA Ligase on a Modified DNA Template: Tethering a Functional Molecule on D-Threoninol. *Chem. Eur. J.* **2011**, *17*, 10388-10396.

(31) You, M. X.; Wang, R. W.; Zhang, X. B.; Chen, Y.; Wang, K. L.; Peng, L.; Tan, W. H. Photon-Regulated DNA-Enzymatic Nanostructures by Molecular Assembly. *ACS Nano* **2011**, *5*, 10090-10095.

(32) Phillips, J. A.; Liu, H.; O'Donoghue, M. B.; Xiong, X.; Wang, R.; You, M.; Sefah, K.; Tan, W. Using Azobenzene Incorporated DNA Aptamers to Probe Molecular Binding Interactions. *Bioconjug. Chem.* **2011**, *22*, 282-288.

(33) Yu, J. M.; Yang, L. R.; Liang, X. F.; Dong, T. T.; Liu, H. Z. Reversible regulation of thrombin adsorption and desorption based on photoresponsive-aptamer modified gold nanoparticles. *Talanta* **2015**, *144*, 312-317.

(34) Asanuma, H.; Liang, X.; Nishioka, H.; Matsunaga, D.; Liu, M.; Komiyama, M. Synthesis of azobenzene-tethered DNA for reversible photo-regulation of DNA functions: hybridization and transcription. *Nat. Protoc.* **2007**, *2*, 203-212.

(35) Asanuma, H.; Liang, X. G.; Yoshida, T.; Komiyama, M. Photocontrol of DNA duplex formation by using azobenzene-bearing oligonucleotides. *ChemBioChem* **2001**, *2*, 39-44.

(36) Asanuma, H.; Ito, T.; Yoshida, T.; Liang, X. G.; Komiyama, M. Photoregulation of the formation and dissociation of a DNA duplex by using the cis-trans isomerization of azobenzene. *Angew. Chem. Int. Ed.* **1999**, *38*, 2393-2395.

(37) Liang, X. G.; Asanuma, H.; Kashida, H.; Takasu, A.; Sakamoto, T.; Kawai, G.; Komiyama, M. NMR study on the photoresponsive DNA tethering an azobenzene. Assignment of the absolute configuration of two diastereomers and structure determination of their duplexes in the trans-form. *J. Am. Chem. Soc.* **2003**, *125*, 16408-16415.

(38) Nakasone, Y.; Ooi, H.; Kamiya, Y.; Asanuma, H.; Terazima, M. Dynamics of Inter-DNA Chain Interaction of Photoresponsive DNA. *J. Am. Chem. Soc.* **2016**, *138*, 9001-9004.

(39) Yan, Y. Q.; Chen, J. I. L.; Ginger, D. S. Photoswitchable Oligonucleotide-Modified Gold Nanoparticles: Controlling Hybridization Stringency with Photon Dose. *Nano Lett.* **2012**, *12*, 2530-2536.

(40) Bandara, H. M. D.; Burdette, S. C. Photoisomerization in different classes of azobenzene. *Chem. Soc. Rev.* **2012**, *41*, 1809-1825.

(41) Beharry, A. A.; Woolley, G. A. Azobenzene photoswitches for biomolecules. *Chem. Soc. Rev.* **2011**, *40*, 4422-4437.

(42) Mahimwalla, Z.; Yager, K. G.; Mamiya, J.; Shishido, A.; Priimagi, A.; Barrett, C. J. Azobenzene photomechanics: prospects and potential applications. *Polym. Bull.* **2012**, *69*, 967-1006.

(43) Yan, Y.; Wang, X.; Chen, J. I. L.; Ginger, D. S. Photoisomerization Quantum Yield of Azobenzene-Modified DNA Depends on Local Sequence. *J. Am. Chem. Soc.* **2013**, *135*, 8382-8387.

(44) Kingsland, A.; Samai, S.; Yan, Y. Q.; Ginger, D. S.; Maibaum, L. Local Density Fluctuations Predict Photoisomerization Quantum Yield of Azobenzene-Modified DNA. *J. Phys. Chem. Lett.* **2016**, *7*, 3027-3031.

(45) Sengupta, E.; Yan, Y. Q.; Wang, X.; Munechika, K.; Ginger, D. S. Dynamic Force Spectroscopy of Photoswitch-Modified DNA. *ACS Nano* **2014**, *8*, 2625-2631.

(46) Zhang, J.; Yan, Y. Q.; Samai, S.; Ginger, D. S. Dynamic Melting Properties of Photoswitch-Modified DNA: Shearing versus Unzipping. *J. Phys. Chem. B* **2016**, *120*, 10706-10713.

(47) Yan, Y. Q.; Samai, S.; Bischoff, K. L.; Zhang, J.; Ginger, D. S. Photocontrolled DNA Hybridization Stringency with Fluorescence Detection in Heterogeneous Assays. *ACS Sens.* **2016**, *1*, 566-571.

(48) Rau, H.: 1 - Photoisomerization of Azobenzenes A2 - Sekkat, Zouheir. In *Photoreactive Organic Thin Films*; Knoll, W., Ed.; Academic Press: San Diego, 2002.

(49) Zimmerman, G.; Chow, L. Y.; Paik, U. J. The Photochemical Isomerization of Azobenzene1. *J. Am. Chem. Soc.* **1958**, *80*, 3528-3531.

(50) Lefevre, R. J. W.; Northcott, J. The Effects of Substituents and Solvents on the Cis→Trans Change of Azobenzene. *J. Chem. Soc.* **1953**, 867-870.

(51) Talaty, E. R.; Fargo, J. C. Thermal Cis–Trans-Isomerization of Substituted Azobenzenes: A Correction of the Literature. *Chem. Commun.* **1967**, 65-66.

(52) Nishimura, N.; Sueyoshi, T.; Yamanaka, H.; Imai, E.; Yamamoto, S.; Hasegawa, S. Thermal Cis-to-Trans Isomerization of Substituted Azobenzenes II. Substituent and Solvent Effects. *Bull. Chem. Soc. Jpn.* **1976**, *49*, 1381-1387.

(53) Hagen, S.; Kate, P.; Peters, M. V.; Hecht, S.; Wolf, M.; Tegeder, P. Kinetic analysis of the photochemically and thermally induced isomerization of an azobenzene derivative on Au(111) probed by two-photon photoemission. *Appl. Phys. A Mater. Sci. Process* **2008**, *93*, 253-260.

(54) Baba, K.; Ono, H.; Itoh, E.; Itoh, S.; Noda, K.; Usui, T.; Ishihara, K.; Inamo, M.; Takagi, H. D.; Asano, T. Kinetic study of thermal Z to E isomerization reactions of azobenzene and 4-dimethylamino-4 '-nitroazobenzene in ionic liquids 1-R-3-methylimidazolium bis(trifluoromethylsulfonyl)imide with R = butyl, pentyl, and hexyl. *Chem. Eur. J.* **2006**, *12*, 5328-5333.

(55) Crecca, C. R.; Roitberg, A. E. Theoretical study of the isomerization mechanism of azobenzene and disubstituted azobenzene derivatives. *J. Phys. Chem. A* **2006**, *110*, 8188-8203.

(56) Fujino, T.; Arzhantsev, S. Y.; Tahara, T. Femtosecond time-resolved fluorescence study of photoisomerization of trans-azobenzene. *J. Phys. Chem. A* **2001**, *105*, 8123-8129.

(57) Diau, E. W. G. A new trans-to-cis photoisomerization mechanism of azobenzene on the S-1(n,pi*) surface. *J. Phys. Chem. A* **2004**, *108*, 950-956.

(58) Rau, H. Further Evidence For Rotation in the Pi, Pi-star and Inversion in the N, Pi-star Photoisomerization of Azobenzenes. *Journal of Photochemistry* **1984**, *26*, 221-225.

(59) Quick, M.; Dobryakov, A. L.; Gerecke, M.; Richter, C.; Berndt, F.; Ioffe, I. N.; Granovsky, A. A.; Mahrwald, R.; Ernsting, N. P.; Kovalenko, S. A. Photoisomerization Dynamics and Pathways of trans- and cis-Azobenzene in Solution from Broadband Femtosecond Spectroscopies and Calculations. *J. Phys. Chem. B* **2014**, *118*, 8756-8771.

(60) Cembran, A.; Bernardi, F.; Garavelli, M.; Gagliardi, L.; Orlandi, G. On the mechanism of the cis-trans isomerization in the lowest electronic states of azobenzene: S-0, S-1, and T-1. *J. Am. Chem. Soc.* **2004**, *126*, 3234-3243.

(61) Victor, J. G.; Torkelson, J. M. On Measuring the Distribution of Local Free Volume in Glassy Polymers by Photochromic and Fluorescence Techniques. *Macromolecules* **1987**, *20*, 2241-2250.

(62) Mita, I.; Horie, K.; Hirao, K. Photochemistry in Polymer Solids. 9. Photoisomerization of Azobenzene in a Polycarbonate Film. *Macromolecules* **1989**, *22*, 558-563.

(63) Ikegami, T.; Kurita, N.; Sekino, H.; Ishikawa, Y. Mechanism of cis-to-trans isomerization of azobenzene: Direct MD study. *J. Phys. Chem. A* **2003**, *107*, 4555-4562.

(64) Whitten , D. G.; Wildes , P. D.; Pacifici , J. G.; Irick, G. J. Solvent and substituent on the thermal isomerization of substituted azobenzenes. Flash spectroscopic study. *J. Am. Chem. Soc.* **1971**, *93*, 2004–2008.

(65) Asano, T.; Okada, T.; Shinkai, S.; Shigematsu, K.; Kusano, Y.; Manabe, O. Temperature and Pressure Dependences of Thermal Cis-to-Trans Isomerization of Azobenzenes Which Evidence an Inversion Mechanism. *J. Am. Chem. Soc.* **1981**, *103*, 5161-5165.

(66) McCullagh, M.; Franco, I.; Ratner, M. A.; Schatz, G. C. DNA-Based Optomechanical Molecular Motor. *J. Am. Chem. Soc.* **2011**, *133*, 3452-3459.

Chapter 4. REVERSIBLY PHOTORECONFIGURABLE PLASMONIC NANOPARTICLE DIMERS LINKED BY DNA

This chapter is mostly adapted with minor modifications from the manuscript "Plasmonic Nanoparticle Dimers with Reversibly Photoswitchable Interparticle Distances Linked by DNA", Soumyadyuti Samai, Tina Lok Yee Choi, Kathryn N. Guye, Yunqi Yan, David S. Ginger, that has been submitted to the *Journal of Physical Chemistry C* for publication.

4.1 OVERVIEW

We report the assembly and optical characterization of stimulus-responsive gold nanoparticle dimers using azobenzene-modified hairpin DNA. We demonstrate a reversible, light-triggered actuation of the interparticle distance using *trans*-to-*cis* reversible photoisomerization of azobenzene. UV exposure leads to an extension of the dimers, and concomitant blue-shift of their scattering spectra, whereas blue light reverses the process, resulting in a red-shift of the bonding plasmon resonance peak of the dimer. These nanoparticle dimers could serve as prototypes of discrete reprogrammable building blocks in future nanotechnology, nanophotonics and biosensing applications.

4.2 INTRODUCTION

Metal nanoparticles and their assemblies are of widespread interest for applications ranging from photonics,[1-4] super-resolution imaging,[5,6] to sensing.[7-12] Advances in colloidal chemistry have enabled the synthesis of size and shape controlled nanoparticles, permitting the precise tuning of their optical properties. At the same time, near-field coupling in nanoparticle assemblies gives rise to a variety of unique collective properties, including formation of more intense local

electromagnetic hot spots,[13-16] and splitting of the plasmon modes of the individual nanoparticle building blocks.[17-20]

Nanoparticle dimers have been extensively investigated as discrete, well-defined systems that have been used as plasmon rulers,[21-25] sensors,[26-28] and as nanoantennas[29-31] for concentrating fields along the interparticle axis. As such, dynamic control over interparticle couplings[32,33] represents a promising research area with the potential to tailor the optical properties of metal nanostructures that offers applications ranging from nanophotonics,[34-36] robust-label-free sensing,[37-41] to thermally-responsive materials for smart windows.[42-44]

Because its length scale is well-matched to the decay lengths of near-field optical coupling, DNA is a particularly powerful material for assembling plasmonic nanostructures.[45-50] While many authors have been able to reconfigure DNA-assembled nanomaterials using chemical inputs,[38,39,51-53] the advent of photoswitchable, azobenzene-modified DNA[54-57] has opened the door to create optically-reconfigurable DNA-linked nanostructures.[40,58-60] For example, our group has previously used azobenzene photoswitches to control the bulk aggregation state of Mirkin-type gold nanoparticles in solution,[40] while Tan's group has designed optically active DNA nanomotor to photoregulate the near-field fluorescence quenching,[61] and Kuzyk et al.[58] have demonstrated light induced conformational changes of chiral plasmonic nanostructures. Here, we prepare discrete nanoparticle dimers, and use photoswitch-modified DNA to enable the reversible modulation of the interparticle distances, allowing us to remotely control the optical properties of discrete dimers, including their scattering peaks and local field enhancements as validated by single-particle dark field scattering microspectroscopy.

4.3 ASSEMBLY AND CHARACTERIZATION OF AZOBENZENE-MODIFIED HAIRPIN DNA-LINKED GOLD NANOPARTICLE DIMERS

Figure 4.1 depicts the stepwise assembly approach we used to prepare the azobenzene-modified DNA linked gold nanoparticle dimers. Briefly, we adapted the hairpin-linking geometry from our dimer-based sensor work[39] to incorporate four azobenzene photoswitches into the DNA. We constructed model dimers, with interesting spectral properties, and unique structural signatures by forming asymmetric dimers comprising one 100 nm and one 50 nm gold nanoparticle (AuNP). Such asymmetric dimers stand out spectroscopically due to their unique polarized scattering spectra and Fano resonances[19,33,62], and are readily distinguished from accidental aggregates of either the larger or smaller nanoparticles via electron microscopy. First, we anchor the dispersed 100 nm AuNPs on a glass substrate, silanized with (3-Aminopropyl) triethoxysilane (APTES) and then, we attach 5' thiol-modified DNA (Seq1) on the exposed AuNP surfaces (see Experimental Methods in Appendix B). Next, we functionalize the 50 nm AuNP, separately in solution,[63] with azobenzene-modified hairpin DNA sequences (Azo-seq2) and assemble them with the Seq1-functionalized 100 nm AuNP on the glass substrate through DNA hybridization (see Experimental Methods in Appendix B).

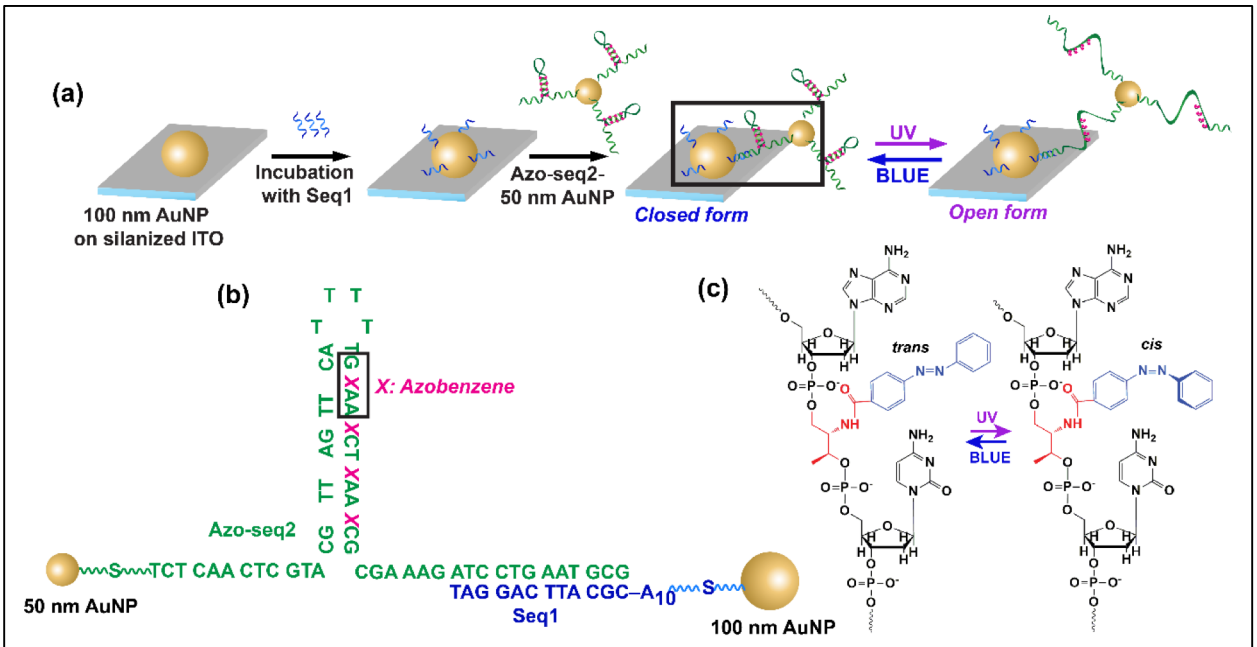

Figure 4.1. Azobenzene-hairpin DNA-linked dimer assembly on ITO substrate. (a) Schematic representation of photoswitchable dimer assembly: 100 nm AuNP is anchored on a silanized ITO and functionalized with DNA sequence, Seq1. The 50 nm AuNP is functionalized with azobenzene-modified hairpin DNA sequence (Azo-seq2) in solution, prior to the assembly process, and then is added to the Seq1-conjugated 100 nm AuNP, fixed to the substrate, to form the dimers through DNA hybridization. (b) Representation of the azobenzene-modified hairpin DNA-linked 100 nm/50 nm AuNP dimer. (c) *Trans*-to-*cis* reversible photoisomerization of azobenzene (blue) incorporated into the DNA strand via D-threoninol linker (red), which causes the reversible reconfiguration of the dimer between its closed and open form.

We verified the dimer assembly process using both dark field spectroscopy and correlated scanning electron microscopy (SEM). Figure 4.2 (a) and (b) show the dark field microscope images of the sample in air before and after dimer formation. Each of the circled green colored particles in the dark field images shown in Figure 4.2 (a) represents single 100 nm gold nanoparticles with Seq1 DNA attached to it and Figure 4.2 (b) shows the same particles after dimer formation with Azo-seq2 functionalized 50 nm AuNP. Dimer formation results in a change in the color from green to orange-green under the dark field illumination. We can distinguish the dimers from residual monomers and non-dimer multimer structures visually in the dark field microscope

by rotating a linear polarizer. When the polarization axis is perpendicular to the dimer's long axis, the transverse scattering mode appears green, whereas a 90° rotation excited the redshifted longitudinal mode, which appears orange-green to the eye in the dark field images for dry dimers (Figure 4.2 (c)).

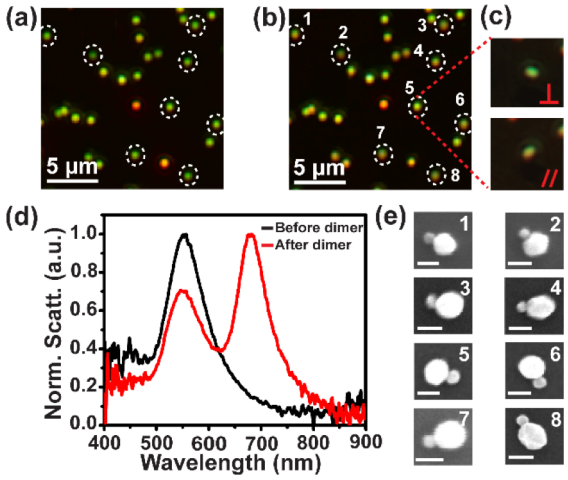

Figure 4.2 Characterization of successful dimer formation showing correlated optical dark field and SEM images. Dark field images of a typical sample in air (a) before and (b) after 100 nm AuNP/50 nm AuNP dimer formation on the substrate. The Seq1 functionalized 100 nm AuNPs appear as green dots under the dark field illumination in (a). The corresponding dimers in (b) are identified by the color change from green to orange-green, as denoted by the white circles. (c) Polarized dark field images of the sample: individual dimers appear green under perpendicular polarization and orange-green under parallel polarization. (d) Single particle dark field scattering spectra before and after dimer formation. The black curve represents the scattering spectrum of a single 100 nm-Seq1 conjugate particle, which exhibits a peak around 540 nm. The red curve is the scattering spectrum of the same particle after dimer formation that exhibits two distinct peaks with varying intensity. The high-energy peak around 540 nm arises due to the transverse plasmon coupling between the two particles and the low energy peak around 680 nm denotes the bonding plasmon resonance mode of the dimer. (e) Correlated Scanning Electron Microscope images of the dimers circled in (b). The scale bar in each image is 100 nm.

We collected dark field scattering spectra of the sample before and after dimer formation and were able to differentiate the dimers from the trimers and larger assemblies with their polarized scattering spectral features. The black trace in Figure 4.2 (d) shows the single particle dark field scattering spectrum of a Seq1-modified 100 nm AuNP in air, before dimer formation, which

exhibits a peak around 540 nm. The red trace in Figure 4.2 (d) represents the unpolarized scattering spectrum of the corresponding 100 nm/50 nm AuNP dimer in air, which exhibits two distinct plasmon resonance peaks. The less intense peak at 540 nm appears due to the weak transverse resonance and more intense peak at 680 nm arises from the longitudinal plasmon resonance of the two coupled particles.[19,32,33] The perpendicular polarized scattering spectrum of the dimer shows only the transverse plasmon resonance peak at 540 nm, whereas all the other polarization angles show both the peaks with different intensity ratios (Figure S1 in Appendix B). For other larger forms of assemblies or aggregates, no polarization angle yields a single peak in the scattering spectra (data not shown).[39] As expected, the polarized dark field scattering spectra provided a rapid and facile means to identify dimers at the single particle level. We also performed correlated scanning electron microscope (SEM) imaging on the samples to further confirm our optical assignment of dimer formation. Figure 4.2 (e) represents the SEM images of the dimers marked in white circles in Figure 4.2 (b).

4.4 Reversible Actuation of Interparticle Distances in the Dimer on *Trans*-to-*Cis* Azobenzene Photoisomerization

After verifying the successful assembly of azobenzene-modified hairpin-DNA-linked nanoparticle dimers, we turned to investigate the effect of illumination on the nanoparticle spectra. Azobenzene-modified DNA can be reversibly photoswitched. Upon exposure to UV-light, the azobenzene photoisomerizes from *trans* to *cis* form and destabilizes the double stranded DNA (dsDNA).[54,56] The *cis* form persists with a thermal half-life of ~31.5 hours at 25 ºC,[64] but can be rapidly converted back to the *trans* form upon exposure to blue light. The goal of our dimer design was, thus to exhibit a shorter interparticle distance in the hairpin form exhibiting the *trans* state,

and to use UV light to unzip the hairpin, therefore increasing the interparticle separation, but in a way, that allows the short distance to be recovered again.

Following dimer assembly, and dry optical dark field imaging in air to confirm the dimer locations, we conducted the photoswitching experiments in buffer to verify that our dimers were operating as intended. After incubating the (previously dried) dimer substrates in 10 mM phosphate buffered saline (PBS) solution containing 0.1 M of NaCl to ensure complete rehydration of the DNA linkers, we acquired single-particle dark field scattering spectra on individual dimers both before, and after UV light irradiation (365 nm, intensity 0.46 mW/cm^2 for 30 minutes), designed to switch the azobenzene modifier from *trans*-to-*cis* form. Followed by exposure to UV illumination, we used blue light (470 nm, intensity, 0.64 mW/cm^2, and duration 30 minutes) to switch the hairpin-linked dimers back to their closed positions. We repeated UV and blue illumination cycles to establish reversibility. The yield of the photo-reconfigurable nanoparticle dimers showing reversible actuation on *trans*-to-*cis* azobenzene photoconversion was ~35-40 % in our experiments. We also encountered dimers that were unable to exhibit reversible light-induced mobility under the same experimental conditions (Figure S2 in Appendix B), and we attribute these fixed particles to inadvertent anchoring of the 50 nm gold nanoparticle to the substrate due to substrate-particle interactions that could be addressed in the future by modification of the substrate, dimer assembly and drying process or choice of buffer solution.

To verify reversible light-induced changes in the plasmon resonance, we measured dark field scattering spectra of ~100 dimer particles from different samples. Figure 4.3 (a) shows the unpolarized normalized scattering intensity from an exemplary photoswitchable dimer in buffer solution before and after reversible photoisomerization of the azobenzene-modified hairpin DNA. This particular dimer exhibits a reversible modulation of ~20 nm in the scattering peak position

upon azobenzene photoswitching. The black curve in Figure 4.3 (a) represents the unpolarized scattering spectrum of the initial closed state of the hairpin DNA-linked dimer. The high intensity peak around 646 nm arises due to the bonding plasmon resonance coupling between the two particles in the closed form of dimer in buffer solution and exhibits a significant blue shift compared to dry condition in air (red curve in Figure 4.2 (d)). This blue shift compared to the dry state of the dimer reflects the decrease in interparticle coupling due to the extension of the DNA length upon hydration in the buffer solution. The red dashed curve in Figure 4.3 (a) shows the scattering spectrum of the same dimer after exposing them to UV light. Upon UV illumination, the main plasmon scattering peak exhibits a blue shift of ~20 nm, which is consistent with an increase in interparticle distance due to extension of the DNA as the *trans*-to-*cis* azobenzene photoisomerization destabilizes the hairpin loop. Upon illumination with blue light, the scattering spectrum red shifts (solid green trace in Figure 4.3 (a)), returning to what it was prior to any UV exposure. This red shift following exposure to blue light is consistent with a reduction in interparticle distance, as is expected due to the *cis*-to-*trans* azobenzene photoisomerization restabilizing the DNA hairpin loop. Figure 4.3 (b) plots the average scattering peak positions measured for 94 photo-reconfigurable dimers following multiple cycles of UV and blue light exposure, and demonstrates the reversibility of the process. The average spectral shift in the longitudinal plasmon peak, calculated over 94 switching dimer particles is 8.3 ± 1.5 nm, from 625.2 ± 2.6 nm to 616.9 ± 1.1 nm, when the dimer structure unfolds on *trans*-to-*cis* photoisomerization of the azobenzenes, achieved by UV irradiation for 30 minutes. For the same set of dimers, we obtain the average red shift in the bonding plasmon resonance peak of the

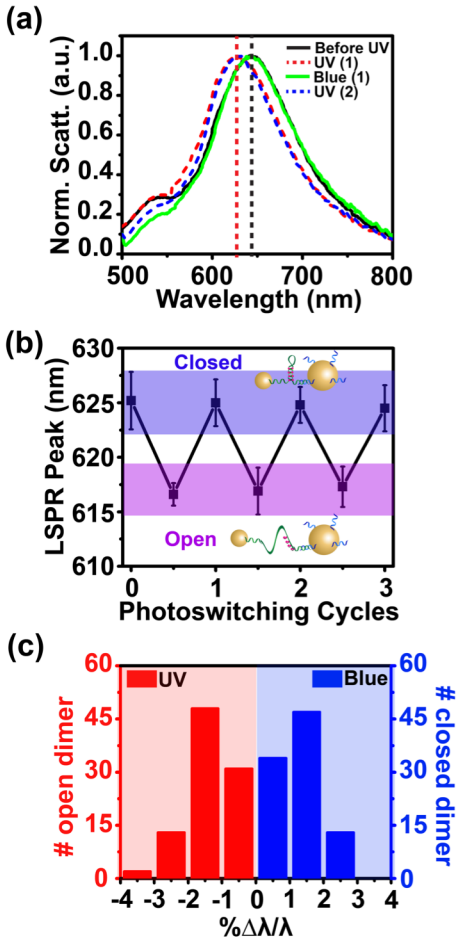

Figure 4.3 Reversible spectral shift of the photoswitchable dimers on *trans*-to-*cis* photoisomerization of azobenzene. (a) Representative dark field scattering spectra of a single 100 nm/50 nm AuNP dimer particle in buffer solution before (black curve) and after multiple UV-Vis photoswitching cycles. The red dashed curve represents the dimer scattering spectrum after UV exposure in the first irradiation cycle, where the bonding plasmon peak blue shifts as the hairpin DNA unzips on *trans*-to-*cis* photoisomerization of azobenzene. The green solid curve shows the dimer spectrum after blue light illumination, where the longitudinal peak red shifts on reverse photoisomerization of azobenzene and overlaps with the spectrum of the initial closed form (black curve). The blue dashed curve represents the scattering spectrum of the same dimer after UV irradiation in the second photoswitching cycle. (b) Reversible change in the scattering spectral peak position of the photoresponsive dimers as the hairpin DNA photomelts and rehybridizes during the multiple azobenzene photoswitching cycles, indicating reversible photo-triggered actuation of the dimers between the closed and the open configuration. The values are obtained by averaging over 94 photoswitching dimers from different samples. The error bars represent the standard errors for each measurement cycles. (c) The histogram plot for the distribution of the relative shifts in the longitudinal plasmon resonance peak for the same set of 94 dimers on azobenzene photoisomerization under UV and blue light illumination.

scattering spectra to be 7.9 ± 1.2 nm on the *cis*-to-*trans* reverse photoisomerization of azobenzene. From the reversibility and the wavelength-dependence of the dimer actuation, and from the fact that dimers functionalized with regular DNA, without any azobenzenes, exhibit no photoresponse under identical conditions (see Section S.1 in Appendix B), we conclude that the reversible reconfiguration of the dimer is due to the incorporation of the azobenzene photoswitches in the hairpin DNA sequence as designed.

Figure 4.3 (c) represents the distribution of the average shifts of the longitudinal plasmon resonance peak for these 94 photo-reconfigurable dimers obtained from the repeating cycles of reversible photoinduced isomerization of azobenzene. Plasmonic nanoparticle dimers have been commonly used as rulers to measure distances and monitor changes in biological structures at nanometer length scales, and the plasmon ruler equation has been derived to correlate the distance between the two nanoparticles in a biological system with spectroscopic shift in the plasmon resonance peak.[21-24] Using the average particle diameter in the plasmon ruler equation,[21] the observed spectral shifts correspond to an extension of the dimer by ~3.4 nm from 14.3 ± 1.7 nm to 17.7 ± 1.5 nm when the *trans*-azobenzenes in the hairpin DNA convert into the *cis* isomer and a decrease in the interparticle separation to 14.5 ± 1.9 nm when the *cis*-azobenzenes isomerize back to the *trans* form. We also performed FDTD calculations to simulate the scattering spectra of a 100 nm/50 nm AuNP dimer (see Section S.3 in Appendix B) and obtained an average distance change of 4 nm, consistent with the plasmon ruler equation.

Even though the average interparticle separation in the closed conformation of the dimer is in good agreement with the DNA sequence length, the change in linker length of ~ 3-4 nm on azobenzene photoswitching is smaller than the difference of ~14.7 nm, we calculate between the length of the DNA linker in its hairpin loop, vs. fully extended single stranded DNA (ssDNA)

configuration.[65,66] We are confident that even setting both particle diameters to 100 nm in the plasmon ruler equation yields a maximum distance change of 4.6 nm, indicating that our dimers are actuating much less than the difference from the closed-hairpin state to fully-extended ssDNA. While a small part of this discrepancy could result from out-of-plane orientations of our dimers, the distance changes are nevertheless smaller than what we previously obtained in a similar hairpin geometry by unzipping with the complementary DNA strand.[39] We speculate that this difference in interparticle distances arises because the single-stranded hairpin is likely not fully extended as compared to experiments where the hairpin is stretched into a linear double-stranded DNA structure by addition of a complementary target sequence,[39] because the single-stranded hairpin is less rigid, and less likely to adopt a fully linear configuration than a double-stranded DNA-linker.[53,67]

4.5 CONCLUSIONS

We have demonstrated the assembly of optically reconfigurable gold nanoparticle dimers using the reversible photoisomerization of azobenzene-modified DNA hairpin linkers. There is currently a great interest in assembling reconfigurable nanoparticle systems for use in photonics, sensing, and other applications.[68] While the first generation of reconfigurable DNA-based materials have predominantly relied on the use of chemical inputs,[10,39,51] the emergence of stimulus-responsive modifiers for DNA now enables reagent-free reconfiguration of interparticle near-field couplings using only an external stimulus, such as light. By measuring the reversible shift in the longitudinal plasmon resonance of discrete single-nanoparticle dimers we have confirmed the photoswitching and reversible actuation of the interparticle near-field coupling. Using the interparticle couplings as plasmon ruler measurements, we determine that the average distance changes on photo-triggered actuation are smaller than those measured for comparable

systems employing complementary unzipping strands, which we propose is likely the result of the flexibility of the single-stranded DNA hairpin structure formed after photomelting. We suggest that future work might increase the change in interparticle coupling achievable using this approach by employing a double-stranded final state, as well as optimizing the length ratio of inactive "linking" DNA sequence to active photoresponsive sequence. Nevertheless, this work points the way towards the use of discrete photoswitchable nanoparticle dimers as reconfigurable nanophotonic elements while also providing a response signature that could be used to differentiate reversible target binding from non-specific binding and interference in DNA and aptamer based sensors.[40,41]

4.6 APPENDIX B

Experimental Methods, Supplementary texts and figures

4.7 ACKNOWLEDGEMENTS

This publication is based primarily on research supported by AFOSR (FA9550-14-1-02509). Part of this work was conducted at the Molecular Analysis Facility, a National Nanotechnology Coordinated Infrastructure site at the University of Washington, which is supported in part by the National Science Foundation (grant ECC-1542101), the University of Washington, the Molecular Engineering & Sciences Institute, the Clean Energy Institute, and the National Institutes of Health. D.S.G. also acknowledges the Alvin L. and Verla R. Kwiram endowed fund and Washington Research Foundation for partial support.

4.8 REFERENCES

(1) Stratakis, E.; Kymakis, E. Nanoparticle-based plasmonic organic photovoltaic devices. *Mater. Today* **2013**, *16*, 133-146.

(2) Stavytska-Barba, M.; Salvador, M.; Kulkarni, A.; Ginger, D. S.; Kelley, A. M. Plasmonic Enhancement of Raman Scattering from the Organic Solar Cell Material P3HT/PCBM by Triangular Silver Nanoprisms. *J. Phys. Chem. C* **2011**, *115*, 20788-20794.

(3) Yao, K.; Salvador, M.; Chueh, C. C.; Xin, X. K.; Xu, Y. X.; deQuilettes, D. W.; Hu, T.; Chen, Y. W.; Ginger, D. S.; Jen, A. K. Y. A General Route to Enhance Polymer Solar Cell Performance using Plasmonic Nanoprisms. *Adv. Energy Mater.* **2014**, *4*.

(4) Kulkarni, A. P.; Noone, K. M.; Munechika, K.; Guyer, S. R.; Ginger, D. S. Plasmon-Enhanced Charge Carrier Generation in Organic Photovoltaic Films Using Silver Nanoprisms. *Nano Lett.* **2010**, *10*, 1501-1505.

(5) Willets, K. A. Super-resolution imaging of interactions between molecules and plasmonic nanostructures. *Phys. Chem. Chem. Phys.* **2013**, *15*, 5345-5354.

(6) Willets, K. A.; Wilson, A. J.; Sundaresan, V.; Joshi, P. B. Super-Resolution Imaging and Plasmonics. *Chem. Rev.* **2017**, *117*, 7538-7582.

(7) Anker, J. N.; Hall, W. P.; Lyandres, O.; Shah, N. C.; Zhao, J.; Van Duyne, R. P. Biosensing with plasmonic nanosensors. *Nat. Mater.* **2008**, *7*, 442-453.

(8) Nam, J. M.; Park, S. J.; Mirkin, C. A. Bio-barcodes based on oligonucleotide-modified nanoparticles. *J. Am. Chem. Soc.* **2002**, *124*, 3820-3821.

(9) Kumar, A.; Kim, S.; Nam, J. M. Plasmonically Engineered Nanoprobes for Biomedical Applications. *J. Am. Chem. Soc.* **2016**, *138*, 14509-14525.

(10) Rosi, N. L.; Mirkin, C. A. Nanostructures in biodiagnostics. *Chem. Rev.* **2005**, *105*, 1547-1562.

(11) Ma, W.; Kuang, H.; Xu, L. G.; Ding, L.; Xu, C. L.; Wang, L. B.; Kotov, N. A. Attomolar DNA detection with chiral nanorod assemblies. *Nat. Commun.* **2013**, *4*.

(12) Willets, K. A.; Van Duyne, R. P. Localized surface plasmon resonance spectroscopy and sensing. *Annu. Rev. Phys. Chem.* **2007**, *58*, 267-297.

(13) Willets, K. A. New Tools for Investigating Electromagnetic Hot Spots in Single-Molecule Surface-Enhanced Raman Scattering. *ChemPhysChem* **2013**, *14*, 3186-3195.

(14) Nam, J. M.; Oh, J. W.; Lee, H.; Suh, Y. D. Plasmonic Nanogap-Enhanced Raman Scattering with Nanoparticles. *Acc. Chem. Res.* **2016**, *49*, 2746-2755.

(15) Ding, S. Y.; Yi, J.; Li, J. F.; Ren, B.; Wu, D. Y.; Panneerselvam, R.; Tian, Z. Q. Nanostructure-based plasmon-enhanced Raman spectroscopy for surface analysis of materials. *Nat. Rev. Mater.* **2016**, *1*.

(16) Zhao, J.; Pinchuk, A. O.; McMahon, J. M.; Li, S. Z.; Ausman, L. K.; Atkinson, A. L.; Schatz, G. C. Methods for Describing the Electromagnetic Properties of Silver and Gold Nanoparticles. *Acc. Chem. Res.* **2008**, *41*, 1710-1720.

(17) Jain, P. K.; El-Sayed, M. A. Plasmonic coupling in noble metal nanostructures. *Chem. Phys. Lett.* **2010**, *487*, 153-164.

(18) Ghosh, S. K.; Pal, T. Interparticle coupling effect on the surface plasmon resonance of gold nanoparticles: From theory to applications. *Chem. Rev.* **2007**, *107*, 4797-4862.

(19) Sheikholeslami, S.; Jun, Y. W.; Jain, P. K.; Alivisatos, A. P. Coupling of Optical Resonances in a Compositionally Asymmetric Plasmonic Nanoparticle Dimer. *Nano Lett.* **2010**, *10*, 2655-2660.

(20) Halas, N. J.; Lal, S.; Chang, W. S.; Link, S.; Nordlander, P. Plasmons in Strongly Coupled Metallic Nanostructures. *Chem. Rev.* **2011**, *111*, 3913-3961.

(21) Jain, P. K.; Huang, W. Y.; El-Sayed, M. A. On the universal scaling behavior of the distance decay of plasmon coupling in metal nanoparticle pairs: A plasmon ruler equation. *Nano Lett.* **2007**, *7*, 2080-2088.

(22) Reinhard, B. M.; Siu, M.; Agarwal, H.; Alivisatos, A. P.; Liphardt, J. Calibration of dynamic molecular rule based on plasmon coupling between gold nanoparticles. *Nano Lett.* **2005**, *5*, 2246-2252.

(23) Sonnichsen, C.; Reinhard, B. M.; Liphardt, J.; Alivisatos, A. P. A molecular ruler based on plasmon coupling of single gold and silver nanoparticles. *Nat. Biotechnol.* **2005**, *23*, 741-745.

(24) Lee, S. E.; Chen, Q.; Bhat, R.; Petkiewicz, S.; Smith, J. M.; Ferry, V. E.; Correia, A. L.; Alivisatos, A. P.; Bissell, M. J. Reversible Aptamer-Au Plasmon Rulers for Secreted Single Molecules. *Nano Lett.* **2015**, *15*, 4564-4570.

(25) Tabor, C.; Murali, R.; Mahmoud, M.; El-Sayed, M. A. On the Use of Plasmonic Nanoparticle Pairs As a Plasmon Ruler: The Dependence of the Near-Field Dipole Plasmon Coupling on Nanoparticle Size and Shape. *J. Phys. Chem. A* **2009**, *113*, 1946-1953.

(26) Guo, L. H.; Ferhan, A. R.; Chen, H. L.; Li, C. M.; Chen, G. N.; Hong, S.; Kim, D. H. Distance-Mediated Plasmonic Dimers for Reusable Colorimetric Switches: A Measurable Peak Shift of More than 60 nm. *Small* **2013**, *9*, 234-240.

(27) Kim, K.; Oh, J. W.; Lee, Y. K.; Son, J.; Nam, J. M. Associating and Dissociating Nanodimer Analysis for Quantifying Ultrasmall Amounts of DNA. *Angew. Chem. Int. Ed.* **2017**, *56*, 9877-9880.

(28) Liu, Y.; Blanchfield, L.; Ma, V. P. Y.; Andargachew, R.; Galior, K.; Liu, Z.; Evavold, B.; Salaita, K. DNA-based nanoparticle tension sensors reveal that T-cell receptors transmit defined pN forces to their antigens for enhanced fidelity. *Proc. Natl. Acad. Sci. U. S. A.* **2016**, *113*, 5610-5615.

(29) Lee, J. H.; You, M. H.; Kim, G. H.; Nam, J. M. Plasmonic Nanosnowmen with a Conductive Junction as Highly Tunable Nanoantenna Structures and Sensitive, Quantitative and Multiplexable Surface-Enhanced Raman Scattering Probes. *Nano Lett.* **2014**, *14*, 6217-6225.

(30) Shegai, T.; Chen, S.; Miljkovic, V. D.; Zengin, G.; Johansson, P.; Kall, M. A bimetallic nanoantenna for directional colour routing. *Nat. Commun.* **2011**, *2*.

(31) Kessentini, S.; Barchiesi, D.; D'Andrea, C.; Toma, A.; Guillot, N.; Di Fabrizio, E.; Fazio, B.; Marago, O. M.; Gucciardi, P. G.; de la Chapelle, M. L. Gold Dimer Nanoantenna with Slanted Gap for Tunable LSPR and Improved SERS. *J. Phys. Chem. C* **2014**, *118*, 3209-3219.

(32) Nordlander, P.; Oubre, C.; Prodan, E.; Li, K.; Stockman, M. I. Plasmon hybridizaton in nanoparticle dimers. *Nano Lett.* **2004**, *4*, 899-903.

(33) Brown, L. V.; Sobhani, H.; Lassiter, J. B.; Nordlander, P.; Halas, N. J. Heterodimers: Plasmonic Properties of Mismatched Nanoparticle Pairs. *ACS Nano* **2010**, *4*, 819-832.

(34) Najafabadi, A. F.; Pakizeh, T. Analytical Chiroptics of 2D and 3D Nanoantennas. *ACS Photonics* **2017**, *4*, 1447-1452.

(35) Albella, P.; de la Osa, R. A.; Moreno, F.; Maier, S. A. Electric and Magnetic Field Enhancement with Ultralow Heat Radiation Dielectric Nanoantennas: Considerations for Surface-Enhanced Spectroscopies. *ACS Photonics* **2014**, *1*, 524-529.

(36) Ma, W.; Kuang, H.; Wang, L. B.; Xu, L. G.; Chang, W. S.; Zhang, H. N.; Sun, M. Z.; Zhu, Y. Y.; Zhao, Y.; Liu, L. Q.; Xu, C. L.; Link, S.; Kotov, N. A. Chiral plasmonics of self-assembled nanorod dimers. *Sci. Rep.* **2013**, *3*.

(37) Homola, J. Surface plasmon resonance sensors for detection of chemical and biological species. *Chem. Rev.* **2008**, *108*, 462-493.

(38) Chen, J. I. L.; Durkee, H.; Traxler, B.; Ginger, D. S. Optical Detection of Protein in Complex Media with Plasmonic Nanoparticle Dimers. *Small* **2011**, *7*, 1993-1997.

(39) Chen, J. I. L.; Chen, Y.; Ginger, D. S. Plasmonic Nanoparticle Dimers for Optical Sensing of DNA in Complex Media. *J. Am. Chem. Soc.* **2010**, *132*, 9600-9601.

(40) Yan, Y. Q.; Chen, J. I. L.; Ginger, D. S. Photoswitchable Oligonucleotide-Modified Gold Nanoparticles: Controlling Hybridization Stringency with Photon Dose. *Nano Lett.* **2012**, *12*, 2530-2536.

(41) Yan, Y. Q.; Samai, S.; Bischoff, K. L.; Zhang, J.; Ginger, D. S. Photocontrolled DNA Hybridization Stringency with Fluorescence Detection in Heterogeneous Assays. *ACS Sens.* **2016**, *1*, 566-571.

(42) Guarrotxena, N.; Quijada-Garrido, I. Optical and Swelling Stimuli-Response of Functional Hybrid Nanogels: Feasible Route to Achieve Tunable Smart Core@Shell Plasmonic@Polymer Nanomaterials. *Chem. Mater.* **2016**, *28*, 1402-1412.

(43) Hamner, K. L.; Maye, M. M. Thermal Aggregation Properties of Nanoparticles Modified with Temperature Sensitive Copolymers. *Langmuir* **2013**, *29*, 15217-15223.

(44) Qian, Z. X.; Guye, K. N.; Masiello, D. J.; Ginger, D. S. Dynamic Optical Switching of Polymer/Plasmonic Nanoparticle Hybrids with Sparse Loading. *J. Phys. Chem. B* **2017**, *121*, 1092-1099.

(45) Nykypanchuk, D.; Maye, M. M.; van der Lelie, D.; Gang, O. DNA-guided crystallization of colloidal nanoparticles. *Nature* **2008**, *451*, 549-552.

(46) Srivastava, S.; Nykypanchuk, D.; Maye, M. M.; Tkachenko, A. V.; Gang, O. Super-compressible DNA nanoparticle lattices. *Soft Matter* **2013**, *9*, 10452-10457.

(47) Kuzyk, A.; Schreiber, R.; Fan, Z.; Pardatscher, G.; Roller, E.-M.; Hoegele, A.; Simmel, F. C.; Govorov, A. O.; Liedl, T. DNA-based self-assembly of chiral plasmonic nanostructures with tailored optical response. *Nature* **2012**, *483*, 311-314.

(48) Schreiber, R.; Luong, N.; Fan, Z. Y.; Kuzyk, A.; Nickels, P. C.; Zhang, T.; Smith, D. M.; Yurke, B.; Kuang, W.; Govorov, A. O.; Liedl, T. Chiral plasmonic DNA nanostructures with switchable circular dichroism. *Nat. Commun.* **2013**, *4*.

(49) Estephan, Z. G.; Qian, Z. X.; Lee, D.; Crocker, J. C.; Park, S. J. Responsive Multidomain Free-Standing Films of Gold Nanoparticles Assembled by DNA-Directed Layer-by-Layer Approach. *Nano Lett.* **2013**, *13*, 4449-4455.

(50) Kumar, A.; Hwang, J. H.; Kumar, S.; Nam, J. M. Tuning and assembling metal nanostructures with DNA. *Chem. Commun.* **2013**, *49*, 2597-2609.

(51) Zhou, C.; Duan, X. Y.; Liu, N. A plasmonic nanorod that walks on DNA origami. *Nat. Commun.* **2015**, *6*.

(52) Urban, M. J.; Zhou, C.; Duan, X. Y.; Liu, N. Optically Resolving the Dynamic Walking of a Plasmonic Walker Couple. *Nano Lett.* **2015**, *15*, 8392-8396.

(53) Maye, M. M.; Kumara, M. T.; Nykypanchuk, D.; Sherman, W. B.; Gang, O. Switching binary states of nanoparticle superlattices and dimer clusters by DNA strands. *Nat. Nanotechnol.* **2010**, *5*, 116-120.

(54) Asanuma, H.; Ito, T.; Yoshida, T.; Liang, X. G.; Komiyama, M. Photoregulation of the formation and dissociation of a DNA duplex by using the cis-trans isomerization of azobenzene. *Angew. Chem. Int. Ed.* **1999**, *38*, 2393-2395.

(55) Asanuma, H.; Liang, X.; Nishioka, H.; Matsunaga, D.; Liu, M.; Komiyama, M. Synthesis of azobenzene-tethered DNA for reversible photo-regulation of DNA functions: hybridization and transcription. *Nat. Protoc.* **2007**, *2*, 203-212.

(56) Asanuma, H.; Liang, X. G.; Yoshida, T.; Komiyama, M. Photocontrol of DNA duplex formation by using azobenzene-bearing oligonucleotides. *ChemBioChem* **2001**, *2*, 39-44.

(57) Nakasone, Y.; Ooi, H.; Kamiya, Y.; Asanuma, H.; Terazima, M. Dynamics of Inter-DNA Chain Interaction of Photoresponsive DNA. *J. Am. Chem. Soc.* **2016**, *138*, 9001-9004.

(58) Kuzyk, A.; Yang, Y. Y.; Duan, X.; Stoll, S.; Govorov, A. O.; Sugiyama, H.; Endo, M.; Liu, N. A light-driven three-dimensional plasmonic nanosystem that translates molecular motion into reversible chiroptical function. *Nat. Commun.* **2016**, *7*, 6.

(59) Blum, A. P.; Kammeyer, J. K.; Rush, A. M.; Callmann, C. E.; Hahn, M. E.; Gianneschi, N. C. Stimuli-Responsive Nanomaterials for Biomedical Applications. *J. Am. Chem. Soc.* **2015**, *137*, 2140-2154.

(60) Zhang, J.; Yan, Y. Q.; Samai, S.; Ginger, D. S. Dynamic Melting Properties of Photoswitch-Modified DNA: Shearing versus Unzipping. *J. Phys. Chem. B* **2016**, *120*, 10706-10713.

(61) Kang, H. Z.; Liu, H. P.; Phillips, J. A.; Cao, Z. H.; Kim, Y.; Chen, Y.; Yang, Z. Y.; Li, J. W.; Tan, W. H. Single-DNA Molecule Nanomotor Regulated by Photons. *Nano Lett.* **2009**, *9*, 2690-2696.

(62) Pena-Rodriguez, O.; Pal, U.; Campoy-Quiles, M.; Rodriguez-Fernandez, L.; Garriga, M.; Alonso, M. I. Enhanced Fano Resonance in Asymmetrical Au:Ag Heterodimers. *J. Phys. Chem. C* **2011**, *115*, 6410-6414.

(63) Hurst, S. J.; Lytton-Jean, A. K. R.; Mirkin, C. A. Maximizing DNA loading on a range of gold nanoparticle sizes. *Anal. Chem.* **2006**, *78*, 8313-8318.

(64) Samai, S.; Bradley, D. J.; Choi, T. L. Y.; Yan, Y. Q.; Ginger, D. S. Temperature-Dependent Photoisomerization Quantum Yields for Azobenzene-Modified DNA. *J. Phys. Chem. C* **2017**, *121*, 6997-7004.

(65) Tinland, B.; Pluen, A.; Sturm, J.; Weill, G. Persistence length of single-stranded DNA. *Macromolecules* **1997**, *30*, 5763-5765.

(66) Chi, Q. J.; Wang, G. X.; Jiang, J. H. The persistence length and length per base of single-stranded DNA obtained from fluorescence correlation spectroscopy measurements using mean field theory. *Physica a-Statistical Mechanics and Its Applications* **2013**, *392*, 1072-1079.

(67) Chi, C.; Vargas-Lara, F.; Tkachenko, A. V.; Starr, F. W.; Gang, O. Internal Structure of Nanoparticle Dimers Linked by DNA. *ACS Nano* **2012**, *6*, 6793-6802.

(68) Qian, Z. X.; Ginger, D. S. Reversibly Reconfigurable Colloidal Plasmonic Nanomaterials. *J. Am. Chem. Soc.* **2017**, *139*, 5266-5276.

Chapter 5. ASSEMBLY AND OPTICAL CHARACTERIZATION OF THERMO-RESPONSIVE POLYMER/SILVER NANOPRISM HYBRIDS

This chapter is mostly adapted with minor modifications from the manuscript "Optical Properties of Reconfigurable Polymer/Silver Nanoprism Hybrids: Tunable Color and IR Scattering Contrast", Soumyadyuti Samai, Zhaoxia Qian, Jian Ling, Kathryn N. Guye, David S. Ginger, that has been submitted to the *ACS Applied Materials and Interfaces* for publication.

5.1 OVERVIEW

We synthesize and characterize stimulus-responsive nanocomposites consisting of poly(N-isopropylacrylamide) (PNIPAM) with controlled loadings of plate-like silver nanoprisms. We use UV-Vis-NIR spectroscopy and dynamic light scattering to characterize the hybrids and show that both the loading density of the silver nanoprisms in the polymer and the size of the nanoprisms are the factors that can be used to tailor the optical response of the composites, extending the range of colors beyond that previously reported with PNIPAM/plasmonic nanoparticle composites. These composites show strong, reversible switching of their optical extinction and scattering properties in response to temperature cycling. In addition, we show that these composites can exhibit very large ratiometric changes in scattering in the NIR with temperature, which could open applications for related materials in thermal management, and NIR labeling and taggants.

5.2 INTRODUCTION

Reconfigurable plasmonic nanomaterials have received attention due to their dynamically tunable physical properties and potential applications in sensing,[1-4] photonics,[5,6] energy harvesting,[7-10]and drug delivery.[11-13] Such responsive nanomaterials can be made from hybrid

composites of plasmonic nanoparticles with linker materials that are responsive to external stimuli such as light, temperature, or pH.[14-18] Changes in the environment can then be used to modulate the near-field coupling between the plasmonic particles, resulting in changes in the optical properties of the composite.

Poly(N-isopropylacrylamide) (PNIPAM) is a popular stimulus-responsive polymer with reliable syntheses and well-characterized physical properties,[19-22] and has been extensively used as a temperature-responsive material that can serve as a scaffold to control the distance and coupling of plasmonic nanoparticles.[23-26] The most commonly studied plasmonic particles in PNIPAM composites are Au nanospheres.[27-32] As such, typical PNIPAM/Au nanoparticle composites exhibit the classic ruby-red color that has been associated with gold colloids since the time of Faraday, until they are heated, either thermally, or photothermally, resulting in final-state optical properties that depend on the details of the assembly and aggregation state of the polymer/nanoparticle composite.[33-36]

Other nanoparticles have also been coupled with PNIPAM with an effort to expand the range of wavelengths/colors and optical properties that can be easily accessed. For example, PNIPAM/gold nanorod composites have been explored for thermoresponsive surface-enhanced Raman scattering (SERS) activity,[37-39] targeted drug release,[40,41] and smart switching materials,[42] while silver nanospheres have been studied due to their high affinity to PNIPAM and wide applications ranging from photonics[43], catalysis,[44-46] to sensing[47,48] and drug delivery.[49] However, most PNIPAM/silver nanoparticle (PNIPAM/AgNP) hybrids incorporate silver nanospheres, or quasi-spheres, which are synthesized by in-situ reduction of silver ions in PNIPAM matrix to stabilize the silver nanoparticles from aggregation.[50] Typically, these PNIPAM/AgNP

nanocomposites produce a shift in their extinction spectrum by 10-30 nm upon thermal cycling.[46,51,52]

Here, we explore the optical properties of reconfigurable nanocomposites synthesized by incorporating plate-like silver nanoprisms (Ag nanoprisms) into the PNIPAM microspheres. We provide an easy fabrication method for these PNIPAM/Ag nanoprism hybrid microgels that allows us to control nanoprism loading density in the polymer. Ag nanoprisms have strong localized surface plasmon bands, and their comparatively narrow LSPR[53] are tunable throughout the visible and near-infrared (NIR) regions of the spectrum by controlling the nanoprism size and shape.[54-56] Furthermore, in contrast to spherical nanoparticles, Ag nanoprisms are anisotropic nanomaterials, which exhibit different forms of interparticle plasmon couplings.[57,58] Face-to-face, edge-to-edge and face-to-edge coupling of the nanoprisms can induce different changes or shifts of the spectral features of their assemblies.[59] Thus, the tethering of Ag nanoprisms on PNIPAM provides an opportunity to construct temperature-responsive three-dimensional plasmonic nanostructures exhibiting a wider range of spectral features and color tunability that can be controlled by both the size and loading ratio of the nanoprisms.

In this paper, we study these polymer/silver nanoprism hybrids with UV-Vis-NIR spectroscopy and dynamic light scattering (DLS) to correlate the temperature-induced changes in their optical properties with concomitant changes in their structures. The polymer/nanoprism composites exhibit redshifts of up to 180 nm in their extinction peak when heated from 25 °C to 50 °C, which are ~5-10 times larger than those reported for comparable structures prepared with silver nanospheres, or quasi-spheres.[46,51,52] As a result, these composites demonstrate reversible and easily visible color switching with temperature, which can be potentially useful for thermochromic sensing applications. We also measure large changes in the near-IR scattering ratio between the

two thermally-switchable states, which may open doors to applications for thermal management or IR scattering labels.

5.3 Assembly and Characterization of PNIPAM/Nanoprism Hybrid Microgels

We prepare thermally-responsive polymer/nanoparticle composites by mixing appropriate ratios of solutions of PNIPAM microgels (typical particle diameter ~ 500−530 nm) with solutions of silver nanoprisms of different sizes as explained in detail in the experimental methods. Compared to the common synthetic protocols for forming silver particles inside PNIPAM hydrogels,[46,51,52] which involve in-situ reduction of silver ions, this simple process of assembling the hybrids enables an easy modulation of the loading density and independent synthetic control over the size of the nanoprisms.

Figure 5.1 (a) and (b) show sample solutions of the resulting, vibrantly colored polymer/nanoprism hybrids prepared from combining PNIPAM microgels with Ag nanoprisms of two different sizes (edge lengths ~ 30 nm in (a) and ~55 nm in (b)) at relatively low loading density as they were cycled between 25 ºC and 50 ºC. At room temperature, the spectrum of each hybrid solution prepared with only a small number of nanoprisms per polymer particle closely matches the spectrum of the isolated nanoprism solution from which it was assembled (Figure S2 in Appendix C). At elevated temperatures, each solution exhibits a clear, reversible color change obvious to the naked eye. At these elevated temperatures (above the lower critical solution temperature (LCST) of 39 ºC at which the PNIPAM collapses), the color change reflects increased interparticle near-field coupling, and the final colors achieved can be tailored by choice of both initial particle type, and loading density. In either case, the expansion of the color palette achieved by using silver nanoprisms in this context is readily apparent, as compared with more conventional

spherical gold[33,34] and silver nanoparticles.[46,52] The electron micrographs in Figure 5.1 show the morphology of the resulting composites, which consist of tens to nearly a hundred nanoprisms per polymer particle (depending on the chosen loading ratio). The micrographs show that these structures closely resemble the structures resulting from spherical gold nanoparticles loaded into PNIPAM microgels,[33] with the anisotropic shape of the silver nanoparticles being the key difference. With these simple experiments demonstrating the wider color palette and reversibility of the thermally-induced color changes, we turn to explore the optical and structural changes of these PNIPAM/Ag nanoprism hybrids in more detail.

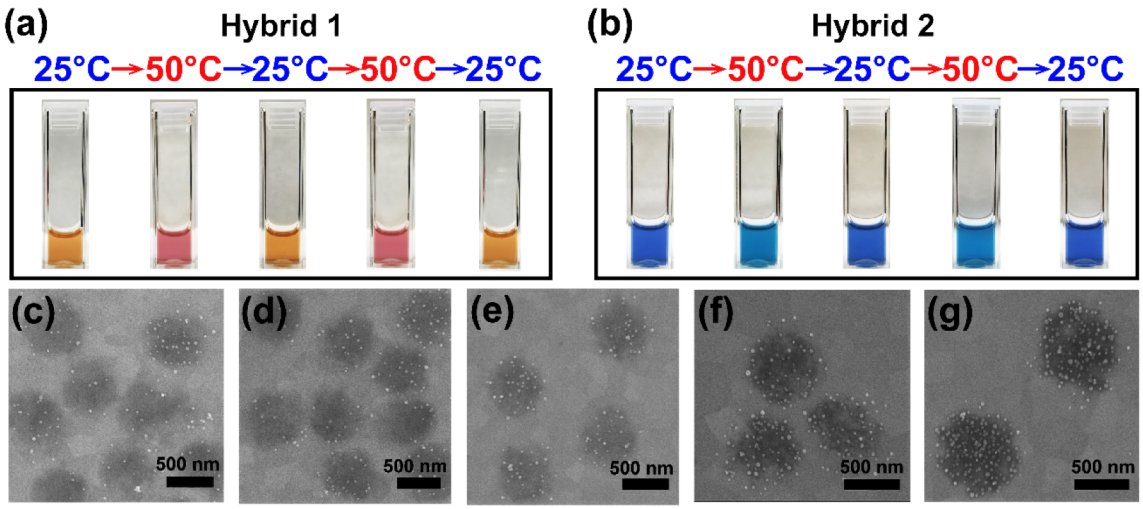

Figure 5.1 (a)-(b) Tunable optical bandwidth and reversible thermochromic switching of two different hybrid microgels, as we cycle the solution temperature between 25 ºC and 50 ºC repetitively. Hybrids 1 and 2 are obtained by mixing two different sizes of silver nanoprisms with the PNIPAM microgels in equal volume parts. (c)-(g) SEM images of hybrid 1 with increasing loading density of the silver nanoprisms (method 1). The darker area in each image denotes the PNIPAM microsphere and the white particles denote the nanoprisms. The hybrid samples are prepared by mixing 600 µL of silver nanoprisms with varying amount of PNIPAM microgels (different volume ratios): (c) 600 µL (1:1), (d) 300 µL (2:1), (e) 150 µL (4:1), (f) 75 µL (8:1) and (g) 37.5 µL (16:1). The density of nanoprisms on the polymer microgel increases as we increase the volume ratio of the nanoprisms to polymer. The average number of particles are measured to be 10 ± 3, 16 ± 6, 30 ± 6, 54 ± 15, 118 ± 15 per PNIPAM sphere in (c)-(g), respectively.

5.4 THERMALLY RESPONSIVE OPTICAL PROPERTIES OF THE HYBRID MICROGELS WITH VARYING LOADING DENSITY OF NANOPRISMS

While the nanoparticle size and shape are primarily responsible for the initial color at lower temperature, we next explore the effect of nanoparticle loading density on the optical properties at elevated temperatures. Figures 5.2 (a) and (b) show the PNIPAM/Ag nanoprism hybrid solutions with the lowest ($V_{Ag\ nanoprism}/V_{PNIPAM}$ = 1:1) and highest ($V_{Ag\ nanoprism}/V_{PNIPAM}$ =16:1) nanoprism loading densities at 25 °C and 50 °C, demonstrating a dramatic color change of the solution from orange to pink (low loading) and brown to pale blue/gray (high loading), respectively, when heated from 25 °C to 50 °C. These photographs show how the temperature-dependent change in the optical properties of these hybrid microgels vary significantly with the nanoprism loading, and that the difference is visible to the naked eye. Figure 5.2 (c) and (d) show the temperature-dependent extinction spectra of the same hybrid solutions as measured by UV-Vis spectroscopy (also see Figure S3 in Appendix C for other hybrids with intermediate nanoprism loading). At 25 °C, the extinction spectrum of the PNIPAM/Ag nanoprism hybrids with low loading densities exhibits only a small red shift of 11 nm and a slightly broader LSPR peak at 489 nm, compared to the pure nanoprisms. As we raise the temperature from 25 °C to 50 °C, the wavelength of the extinction peak changes from 489 nm to 535 nm for the hybrids with the lowest loading ratio of the nanoprisms (Figure 5.2 (c)), while it shifts by 186 nm, from 500 to 686 nm, for the hybrids with higher loadings (Figure 5.2 (d)). Notably this temperature-induced change in the plasmon band is significantly (5-10X) greater than those previously reported for silver nanoparticle containing PNIPAM nanocomposite materials.[46,51,52]

Figure 5.2 (e) and (f) show that the nanoprism loading also affects the temperature at which the most dramatic changes in optical properties are observed. Despite being assembled from the same PNIPAM and same nanoprisms, composites with higher nanoprism loadings yield greater changes at lower temperature. At both low and high temperatures, the increased red shift and linewidth broadening of the LSPR peak we observe with increasing nanoprism loading density is consistent with increased near-field coupling between the particles as the separation between them decreases at higher loadings and higher temperatures.[33] For the sample shown in Figures 5.2 (b), (d) and (f) the effect on the color change is pronounced: while the spectrum continues to red-shift

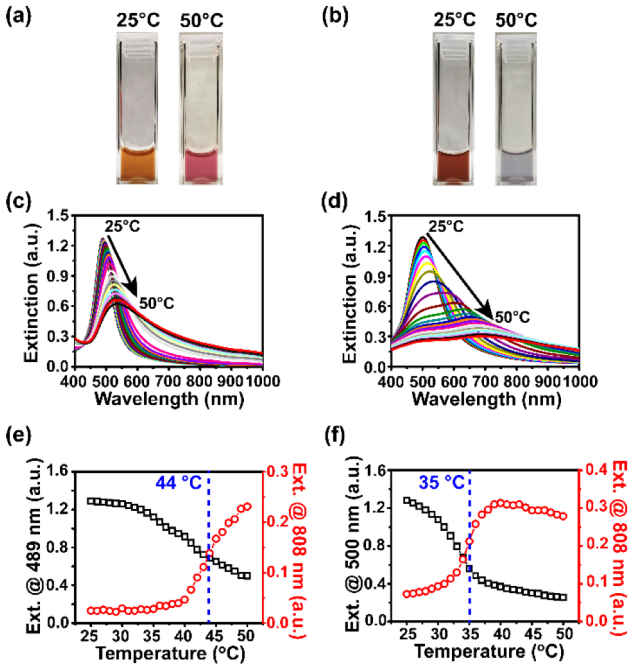

Figure 5.2 The thermal-responsivity of the optical behavior changes with the loading density of the silver nanoprisms on the PNIPAM microgel. The photographs of the hybrid microgels with (a) lowest ($V_{Ag\ nanoprism}/V_{PNIPAM}$ = 1:1) and (b) highest ($V_{Ag\ nanoprism}/V_{PNIPAM}$ = 16:1) loading density of the Ag nanoprisms at 25 °C and 50 °C. Temperature-dependent modulation of the extinction spectra of the hybrid solutions with (c) lowest and (d) highest loading density of the nanoprisms. The extinction maximum shifts only from 489 nm at 25 °C to 535 nm at 50 °C for the hybrids in (c), whereas it changes from 500 nm to 686 nm for the hybrids in (d) on going from 25 °C to 50 °C. The corresponding changes in the extinction at 489 nm and 500 nm (black squares) and 808 nm (red circles) of the hybrids with temperature are shown for (e) lowest and (f) highest nanoprism loadings. The blue dashed line denotes the temperature at which maximum change in the extinction is observed (calculated from the first derivative) for the solution.

and broaden with increasing temperature, the extinction peak moves into the NIR and the spectrum becomes so broad that, instead of turning red like the solution at lower loading, it turns a neutral blue/gray.

5.5 THERMALLY REVERISBLE OPTICAL PROPERTIES OF PNIPAM/ NANOPRISM HYBRID MICROGELS

Next, we examine the reversibility of both the optical and structural properties of these PNIPAM/Ag nanoprism hybrids at various loading densities. Figure 5.3 (a) and (b) show the extinction spectra of the nanocomposites with minimum and maximum loading density of nanoprisms, respectively, as we subject the hybrid solutions to repeated heating-cooling cycles by changing the temperature between 25 °C and 50 °C. The plasmon resonance peak position of the nanocomposites with minimum loading density ($V_{Ag\ nanoprism}/V_{PNIPAM}$ = 1:1) changes from 489 nm to 527 nm when the solution is heated from 25 °C to 50 °C and then changes back to 494 nm on cooling down to 25 °C, giving a small red shift of 5 nm and a slight broadening after the first thermal switching cycle. On the other hand, the plasmon resonance band for the hybrid with maximum nanoparticle loading ($V_{Ag\ nanoprism}/V_{PNIPAM}$ = 16:1) shifts from 500 nm to 640 nm, as shown in Figure 5.3 (b), when temperature is raised to 50 °C in the first cycle, and it goes back to 508 nm after the first cycle with the plasmon band at 25 °C being somewhat broader than it was at 25 °C before cycling (also see Figure S5 in Appendix C for the hybrids with intermediate nanoprism loading densities). Even though we observe a gradual broadening in the extinction spectra of all the hybrids and a small drift in the resonance peak position both at 25 °C and 50 °C in the following heating-cooling cycles (Figure 5.3 (c)), the change in the optical responses of the hybrids is largely reversible with temperature (Figure S6 in Appendix C), with a gradual red-shifting over time observed for the higher-loading density samples. We speculate that this gradual

red shift and the broadening of the plasmon peak over time after cycling may occur because the nanoprisms slowly change their initial positions over time, gradually migrating inward into the polymer sphere during repeated cyclings.[33]

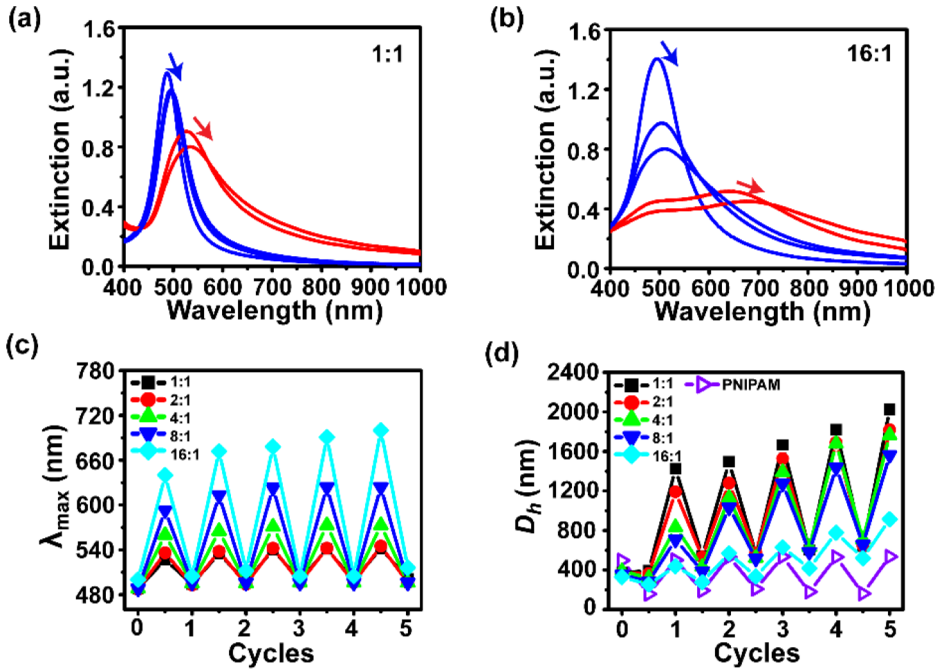

Figure 5.3 Extinction spectra of the hybrid microgels with (a) lowest and (b) highest loading of nanoprisms as the solution temperature is switched between 25 °C (blue spectra) and 50 °C (red spectra), repetitively. The arrows indicate increasing number of heating/cooling cycles. (c) Change in plasmon resonance peak positions of all the hybrids with various loading densities of the nanoprisms during the thermal cycling process. The hybrids demonstrate reversible switching of their optical properties with a gradual broadening and red shift in the plasmon peak with consecutive heating-cooling cycles. (d) Change in the hydrodynamic diameter of the hybrids with various nanoprism loading ratios, as we cycle the temperature between 25 °C and 50 °C for multiple times. While pure PNIPAM microgel undergoes a thermally reversible volume-phase transition without any aggregation, the hybrids show a reversible swelling-shrinking along with heat-induced aggregation over time. Even though the polydispersity indexes of the aggregated hybrids were measured to be in the range of 0.2-0.6, we expect them to be non-spherical and hence the hydrodynamic diameters measured by DLS might not be accurate.

5.6 THERMALLY REVERSIBLE STRUCTURAL PROPERTIES OF PNIPAM/NANOPRISM HYBRID MICROGELS

We also examine the thermally reversible swelling-deswelling behavior of the nanocomposites as we switch the temperature between 25 °C and 50 °C. Figure 5.3 (d) reveals that the hybrids microgels undergo thermally reversible phase transition, much like pure PNIPAM microgels, but can begin to exhibit gradual heat-induced aggregation over time (see Section S.1 in Appendix C), which is not a phenomena reported previously for either gold or silver nanosphere containing PNIPAM composites. The change in the hydrodynamic diameter during the thermal switching cycles is consistent with the change in the extinction properties of the hybrids as described above. The red-shifting and broadening of the extinction spectra of the hybrids after multiple temperature cycles would be consistent both with some aggregation, and with inward migration of the metal nanoparticles in the PNIPAM microgel particles as has previously been described for gold nanospheres.[33] The hydrodynamic diameter and swelling-deswelling behavior is noticeably reduced for microgels with the highest nanoprisms loading, which is consistent with previous reports.[46,64,65]

5.7 TEMPERATURE-RESPONSIVE NIR SCATTERING OF THE HYBRID MICROGELS

Due to their fairly narrow plasmon peaks, and ability to achieve relatively blue initial peak positions of the hybrids, it is possible to prepare polymer/Ag nanoprism hybrids that have very little, if any, NIR scattering at low temperature. From a ratiometric standpoint, heating above the LCST can be used to drive a dramatic increase in NIR scattering of the hybrids, which we speculate could be useful for NIR color switching materials in bio-imaging or as smart materials in

nanophotonics or thermal management applications. To examine these properties in more detail, we also specifically study the NIR scattering properties of these composites.

Figure 5.4 (a) shows the NIR scattering images of the different PNIPAM/Ag nanoprism hybrid microgels at various temperatures when illuminated with an 808 nm laser diode. This set of images demonstrates that the range of scattering intensities of the hybrids increases as a function of temperature as well as with loading density of the nanoprisms. The enhancement in the NIR scattering at higher temperatures is consistent with the increasing interparticle plasmonic coupling due to the collapse of the PNIPAM microspheres during its volume-phase transition. With increasing loading densities of nanoprisms, larger nanoparticle clusters with greater scattering cross-section area are formed when the hybrids shrink, resulting in brighter NIR scattering images at higher temperatures.

Figure 5.4 (a) also reveals that the heat-induced change in the NIR scattering intensity (Figure S9 in Appendix C) follows a similar trend as the change in their extinction at 808 nm shown in Figure 5.2 (e) and (f) (and Figure S3 (g), (h), and (i) in Appendix C). Figure 5.4 (b) and (c) quantify the reversible modulation of the NIR scattering intensity and the corresponding images of the nanocomposites at the lowest and highest nanoprism loadings we studied, as we thermally switch them between the expanded and collapsed states by changing the temperature between 25 °C and 50 °C (also see Figure S10 in Appendix C). We find that while the hybrid microgels with maximum nanoprism density exhibit the highest NIR scattering as a function of temperature, the nanocomposites with lowest nanoprism density show the greatest relative enhancement in the NIR scattering (by ~7 times) on going from 25 °C to 50 °C. These findings are relevant for the potential use of these nanocomposites as smart switching materials in NIR imaging applications with

various purposes, either to obtain the maximum contrast in the images with the temperature change or to achieve the highest NIR scattering at any temperature.

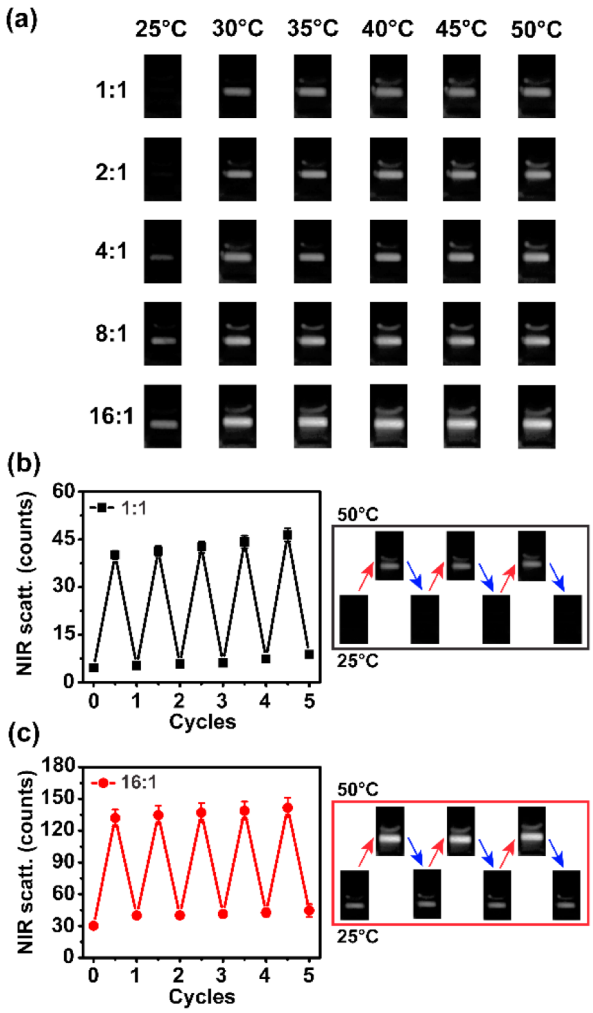

Figure 5.4 (a) NIR images of the PNIPAM/Ag nanoprism hybrids at different temperatures as we heat them up from 25 °C to 50 °C and expose them to an 808 nm laser diode. The NIR scattering intensity of the solution increases as we increase the temperature and the loading density of the nanoprisms on the PNIPAM microgels. Reversibility of the NIR scattering intensity of the hybrids with (b) lowest and (c) highest loading ratios of the Ag nanoprisms and the corresponding NIR images of the solutions as we thermally switch them between 25 °C and 50 °C.

5.8 CONCLUSIONS

In conclusion, we have assembled reconfigurable PNIPAM nanocomposites incorporating Ag nanoprisms and demonstrated tailorability of the composites' optical properties by controlling both the nanoprism size and the loading density in the polymer microparticles. The resulting nanocomposites exhibited reversible thermochromic behavior with easily observed changes in color. Notably, we demonstrated a >180 nm shift of the extinction peak of the hybrid microgels upon increasing the temperature from 25 °C to 50 °C, which is significantly greater than the range reported in the literature for similar PNIPAM nanocomposites containing silver nanospheres. In addition, we exhibited large changes in NIR scattering ratios, with composites exhibiting an eight-fold increase in scattering at 808 nm upon heating. Our results also show that the NIR scattering intensity of these hybrids increases with the loading density of the nanoprisms and can be reversibly modulated with the temperature. This work provides a promising pathway to construct reconfigurable plasmonic materials with reversible color switching and significant enhancement in the NIR scattering. We anticipate that such plasmonic-hybrid materials will find promising applications in various fields ranging from bio-imaging and color changing technologies to smart materials in nanophotonics. We believe that further improvements in response and stability could be obtained by tuning the polymer/nanoparticle interactions, perhaps with specific attachment chemistries, to assert chemical control over loading density and particle position that can be preserved during temperature cycling, or incorporating photochemistry[14] or photothermal effects[66] to extend the stimulus response behavior into the optical domain.

5.9 APPENDIX C

Experimental Methods, Supplementary texts and figures

5.10 ACKNOWLEDGMENTS

This publication is in part on work initially supported by AFOSR (FA9550-14-1-02509). Part of this work was conducted at the Molecular Analysis Facility, a National Nanotechnology Coordinated Infrastructure site at the University of Washington, which is supported in part by the National Science Foundation (grant ECC-1542101), the University of Washington, the Molecular Engineering & Sciences Institute, the Clean Energy Institute, and the National Institutes of Health. D.S.G. also acknowledges the Alvin L. and Verla R. Kwiram endowed fund and Washington Research Foundation for partial support. S.S and Z.Q. also acknowledge Prof. Miqin Zhang and her group in the Department of Materials Science and Engineering, University of Washington, for Malvern Zetasizer instrument used for all the dynamic light scattering measurements.

5.11 REFERENCES

(1) Yan, Y. Q.; Chen, J. I. L.; Ginger, D. S. Photoswitchable Oligonucleotide-Modified Gold Nanoparticles: Controlling Hybridization Stringency with Photon Dose. *Nano Lett.* **2012**, *12*, 2530-2536.

(2) Joshi, G. K.; Blodgett, K. N.; Muhoberac, B. B.; Johnson, M. A.; Smith, K. A.; Sardar, R. Ultrasensitive Photoreversible Molecular Sensors of Azobenzene-Functionalized Plasmonic Nanoantennas. *Nano Lett.* **2014**, *14*, 532-540.

(3) Kuzyk, A.; Yang, Y.; Duan, X.; Stoll, S.; Govorov, A. O.; Sugiyama, H.; Endo, M.; Liu, N. A light-driven three-dimensional plasmonic nanosystem that translates molecular motion into reversible chiroptical function. *Nat. Commun.* **2016**, *7*, 10591.

(4) Nam, J. M.; Park, S. J.; Mirkin, C. A. Bio-barcodes based on oligonucleotide-modified nanoparticles. *J. Am. Chem. Soc.* **2002**, *124*, 3820-3821.

(5) Karg, M.; Hellweg, T.; Mulvaney, P. Self-Assembly of Tunable Nanocrystal Superlattices Using Poly-(NIPAM) Spacers. *Adv. Funct. Mater.* **2011**, *21*, 4668-4676.

(6) Schafer, C. G.; Winter, T.; Heidt, S.; Dietz, C.; Ding, T.; Baumberg, J. J.; Gallei, M. Smart polymer inverse-opal photonic crystal films by melt-shear organization for hybrid core-shell architectures. *J. Mater. Chem. C* **2015**, *3*, 2204-2214.

(7) Shim, T. S.; Estephan, Z. G.; Qian, Z. X.; Prosser, J. H.; Lee, S. Y.; Chenoweth, D. M.; Lee, D.; Park, S. J.; Crocker, J. C. Shape changing thin films powered by DNA hybridization. *Nat. Nanotechnol.* **2017**, *12*, 41-47.

(8) Kim, K.; Xu, X. B.; Guo, J. H.; Fan, D. L. Ultrahigh-speed rotating nanoelectromechanical system devices assembled from nanoscale building blocks. *Nat. Commun.* **2014**, *5*.

(9) Baffou, G.; Quidant, R. Thermo-plasmonics: using metallic nanostructures as nano-sources of heat. *Laser Photon. Rev.* **2013**, *7*, 171-187.

(10) Estephan, Z. G.; Qian, Z. X.; Lee, D.; Crocker, J. C.; Park, S. J. Responsive Multidomain Free-Standing Films of Gold Nanoparticles Assembled by DNA-Directed Layer-by-Layer Approach. *Nano Lett.* **2013**, *13*, 4449-4455.

(11) Mura, S.; Nicolas, J.; Couvreur, P. Stimuli-responsive nanocarriers for drug delivery. *Nat. Mater.* **2013**, *12*, 991-1003.

(12) Karimi, M.; Zangabad, P. S.; Ghasemi, A.; Amiri, M.; Bahrami, M.; Malekzad, H.; Asl, H. G.; Mandieh, Z.; Bozorgomid, M.; Boyuk, M.; Hamblin, M. R. Temperature-Responsive Smart Nanocarriers for Delivery Of Therapeutic Agents: Applications and Recent Advances. *ACS Appl. Mater. Interfaces* **2016**, *8*, 21107-21133.

(13) Kang, H. Z.; Trondoli, A. C.; Zhu, G. Z.; Chen, Y.; Chang, Y. J.; Liu, H. P.; Huang, Y. F.; Zhang, X. L.; Tan, W. H. Near-Infrared Light-Responsive Core-Shell Nanogels for Targeted Drug Delivery. *ACS Nano* **2011**, *5*, 5094-5099.

(14) Qian, Z.; Ginger, D. S. Reversibly Reconfigurable Colloidal Plasmonic Nanomaterials. *J. Am. Chem. Soc.* **2017**, *139*, 5266-5276.

(15) Wang, J. Y.; Song, K.; Wang, L.; Liu, Y. J.; Liu, B.; Zhu, J. T.; Xie, X. L.; Nie, Z. H. Formation of hybrid core-shell microgels induced by autonomous unidirectional migration of nanoparticles. *Mater. Horizons* **2016**, *3*, 78-82.

(16) Liu, Y.; Liu, Y. J.; Yin, J. J.; Nie, Z. H. Self-Assembly of Amphiphilic Block Copolymer-Tethered Nanoparticles: a New Approach to Nanoscale Design of Functional Materials. *Macromol. Rapid Commun.* **2015**, *36*, 711-725.

(17) Stuart, M. A. C.; Huck, W. T. S.; Genzer, J.; Muller, M.; Ober, C.; Stamm, M.; Sukhorukov, G. B.; Szleifer, I.; Tsukruk, V. V.; Urban, M.; Winnik, F.; Zauscher, S.; Luzinov, I.; Minko, S. Emerging applications of stimuli-responsive polymer materials. *Nat. Mater.* **2010**, *9*, 101-113.

(18) Karg, M.; Hellweg, T. Smart inorganic/organic hybrid microgels: Synthesis and characterisation. *J. Mater. Chem.* **2009**, *19*, 8714-8727.

(19) Schild, H. G. Poly (N-isopropylacrylamide) - Experiment, Theory and Application. *Prog. Polym. Sci.* **1992**, *17*, 163-249.

(20) Pelton, R. Temperature-sensitive aqueous microgels. *Adv. Colloid Interface Sci.* **2000**, *85*, 1-33.

(21) Shimizu, H.; Wada, R.; Okabe, M. Preparation and Characterization of Micrometer-Sized Poly(N-isopropylacrylamide) Hydrogel Particles. *Polym. J.* **2009**, *41*, 771-777.

(22) Osa, M. Aqueous Solution Properties of Poly(N-isopropylacrylamide). *Kobunshi Ronbunshu* **2009**, *66*, 273-288.

(23) Honold, T.; Volk, K.; Rauh, A.; Fitzgerald, J. P. S.; Karg, M. Tunable plasmonic surfaces via colloid assembly. *J. Mater. Chem. C* **2015**, *3*, 11449-11457.

(24) Karg, M. Functional Materials Design through Hydrogel Encapsulation of Inorganic Nanoparticles: Recent Developments and Challenges. *Macromol. Chem. Phys.* **2016**, *217*, 242-255.

(25) Perez-Juste, J.; Pastoriza-Santos, I.; Liz-Marzan, L. M. Multifunctionality in metal@microgel colloidal nanocomposites. *J. Mater. Chem. A* **2013**, *1*, 20-26.

(26) Karg, M.; Hellweg, T. New "smart" poly(NIPAM) microgels and nanoparticle microgel hybrids: Properties and advances in characterisation. *Curr. Opin. Colloid Interface Sci.* **2009**, *14*, 438-450.

(27) Ding, T.; Ruttiger, C.; Zheng, X. Z.; Benz, F.; Ohadi, H.; Vandenbosch, G. A. E.; Moshchalkov, V. V.; Gallei, M.; Baumberg, J. J. Fast Dynamic Color Switching in Temperature-Responsive Plasmonic Films. *Adv. Opt. Mater.* **2016**, *4*, 877-882.

(28) Ding, T.; Rudrum, A. W.; Herrmann, L. O.; Turek, V.; Baumberg, J. J. Polymer-assisted self-assembly of gold nanoparticle monolayers and their dynamical switching. *Nanoscale* **2016**, *8*, 15864-15869.

(29) Gawlitza, K.; Turner, S. T.; Polzer, F.; Wellert, S.; Karg, M.; Mulvaney, P.; von Klitzing, R. Interaction of gold nanoparticles with thermoresponsive microgels: influence of the cross-linker density on optical properties. *Phys. Chem. Chem. Phys.* **2013**, *15*, 15623-15631.

(30) Jaber, S.; Karg, M.; Morfa, A.; Mulvaney, P. 2D assembly of gold-PNIPAM core-shell nanocrystals. *Phys. Chem. Chem. Phys.* **2011**, *13*, 5576-5578.

(31) Murphy, S.; Jaber, S.; Ritchie, C.; Karg, M.; Mulvaney, P. Laser Flash Photolysis of Au-PNIPAM Core-Shell Nanoparticles: Dynamics of the Shell Response. *Langmuir* **2016**, *32*, 12497-12503.

(32) Dulle, M.; Jaber, S.; Rosenfeldt, S.; Radulescu, A.; Forster, S.; Mulvaney, P.; Karg, M. Plasmonic gold-poly(N-isopropylacrylamide) core-shell colloids with homogeneous density profiles: a small angle scattering study. *Phys. Chem. Chem. Phys.* **2015**, *17*, 1354-1367.

(33) Qian, Z. X.; Guye, K. N.; Masiello, D. J.; Ginger, D. S. Dynamic Optical Switching of Polymer/Plasmonic Nanoparticle Hybrids with Sparse Loading. *J. Phys. Chem. B* **2017**, *121*, 1092-1099.

(34) Lim, S.; Song, J. E.; La, J. A.; Cho, E. C. Gold Nanospheres Assembled on Hydrogel Colloids Display a Wide Range of Thermoreversible Changes in Optical Bandwidth for Various Plasmonic-Based Color Switches. *Chem. Mater.* **2014**, *26*, 3272-3279.

(35) Contreras-Caceres, R.; Pacifico, J.; Pastoriza-Santos, I.; Perez-Juste, J.; Fernandez-Barbero, A.; Liz-Marzan, L. M. Au@pNIPAM Thermosensitive Nanostructures: Control over Shell Cross-linking, Overall Dimensions, and Core Growth. *Adv. Funct. Mater.* **2009**, *19*, 3070-3076.

(36) Lian, X. M.; Jin, J.; Tian, J.; Zhao, H. Y. Thermoresponsive Nanohydrogels Cross-Linked by Gold Nanoparticles. *ACS Appl. Mater. Interfaces* **2010**, *2*, 2261-2268.

(37) Fernandez-Lopez, C.; Polavarapu, L.; Solis, D. M.; Taboada, J. M.; Obelleiro, F.; Contreras-Caceres, R.; Pastoriza-Santos, I.; Perez-Juste, J. Gold Nanorod-pNIPAM Hybrids with Reversible Plasmon Coupling: Synthesis, Modeling, and SERS Properties. *ACS Appl. Mater. Interfaces* **2015**, *7*, 12530-12538.

(38) Karg, M.; Lu, Y.; Carbo-Argibay, E.; Pastoriza-Santos, I.; Perez-Juste, J.; Liz-Marzan, L. M.; Hellweg, T. Multiresponsive Hybrid Colloids Based on Gold Nanorods and Poly(NIPAM-co-allylacetic acid) Microgels: Temperature- and pH-Tunable Plasmon Resonance. *Langmuir* **2009**, *25*, 3163-3167.

(39) Karg, M.; Pastoriza-Santos, I.; Perez-Juste, J.; Hellweg, T.; Liz-Marzan, L. M. Nanorod-coated PNIPAM microgels: Thermoresponsive optical properties. *Small* **2007**, *3*, 1222-1229.

(40) Kawano, T.; Niidome, Y.; Mori, T.; Katayama, Y.; Niidome, T. PNIPAM Gel-Coated Gold Nanorods, for Targeted Delivery Responding to a Near-Infrared Laser. *Bioconjug. Chem.* **2009**, *20*, 209-212.

(41) Gorelikov, I.; Field, L. M.; Kumacheva, E. Hybrid microgels photoresponsive in the near-infrared spectral range. *J. Am. Chem. Soc.* **2004**, *126*, 15938-15939.

(42) Zhang, C. L.; Cao, F. H.; Wang, J. L.; Yu, Z. L.; Ge, J.; Lu, Y.; Wang, Z. H.; Yu, S. H. Highly Stimuli-Responsive Au Nanorods/Poly(N-isopropylacrylamide) (PNIPAM) Composite Hydrogel for Smart Switch. *ACS Appl. Mater. Interfaces* **2017**, *9*, 24857-24863.

(43) Xu, S. Q.; Zhang, J. G.; Paquet, C.; Lin, Y. K.; Kumacheva, E. From hybrid microgels to photonic crystals. *Adv. Funct. Mater.* **2003**, *13*, 468-472.

(44) Lu, Y.; Mei, Y.; Ballauff, M.; Drechsler, M. Thermosensitive core-shell particles as carrier systems for metallic nanoparticles. *J. Phys. Chem. B* **2006**, *110*, 3930-3937.

(45) Zhang, J. T.; Wei, G.; Keller, T. F.; Gallagher, H.; Stotzel, C.; Muller, F. A.; Gottschaldt, M.; Schubert, U. S.; Jandt, K. D. Responsive Hybrid Polymeric/Metallic Nanoparticles for Catalytic Applications. *Macromol. Mater. Eng.* **2010**, *295*, 1049-1057.

(46) Liu, Y. Y.; Liu, X. Y.; Yang, J. M.; Lin, D. L.; Chen, X.; Zha, L. S. Investigation of Ag nanoparticles loading temperature responsive hybrid microgels and their temperature controlled catalytic activity. *Colloids Surf. A -Physicochemical and Engineering Aspects* **2012**, *393*, 105-110.

(47) Tang, F.; Ma, N.; Tong, L. Y.; He, F.; Li, L. D. Control of Metal-Enhanced Fluorescence with pH- and Thermoresponsive Hybrid Microgels. *Langmuir* **2012**, *28*, 883-888.

(48) Wu, W.; Shen, J.; Li, Y.; Zhu, H.; Banerjee, P.; Zhou, S. Specific glucose-to-SPR signal transduction at physiological pH by molecularly imprinted responsive hybrid microgels. *Biomaterials* **2012**, *33*, 7115-7125.

(49) Wu, W. T.; Mitra, N.; Yan, E. C. Y.; Zhou, S. Q. Multifunctional Hybrid Nanogel for Integration of Optical Glucose Sensing and Self-Regulated Insulin Release at Physiological pH. *ACS Nano* **2010**, *4*, 4831-4839.

(50) Begum, R.; Naseem, K.; Farooqi, Z. H. A review of responsive hybrid microgels fabricated with silver nanoparticles: synthesis, classification, characterization and applications. *J. Sol-Gel Sci. Technol.* **2016**, *77*, 497-515.

(51) Dong, Y.; Ma, Y.; Zhai, T.; Shen, F.; Zeng, Y.; Fu, H.; Yao, J. Silver Nanoparticles Stabilized by Thermoresponsive Microgel Particles: Synthesis and Evidence of an Electron Donor-Acceptor Effect. *Macromol. Rapid Commun.* **2007**, *28*, 2339-2345.

(52) Liu, X. Y.; Wang, X. Q.; Zha, L. S.; Lin, D. L.; Yang, J. M.; Zhou, J. F.; Zhang, L. Temperature- and pH-tunable plasmonic properties and SERS efficiency of the silver nanoparticles within the dual stimuli-responsive microgels. *J. Mater. Chem. C* **2014**, *2*, 7326-7335.

(53) Munechika, K.; Smith, J. M.; Chen, Y.; Ginger, D. S. Plasmon line widths of single silver nanoprisms as a function of particle size and plasmon peak position. *J. Phys. Chem. C* **2007**, *111*, 18906-18911.

(54) Jin, R.; Cao, Y.; Mirkin, C. A.; Kelly, K. L.; Schatz, G. C.; Zheng, J. G. Photoinduced Conversion of Silver Nanospheres to Nanoprisms. *Science* **2001**, *294*, 1901-1903.

(55) Sherry, L. J.; Jin, R.; Mirkin, C. A.; Schatz, G. C.; Van Duyne, R. P. Localized Surface Plasmon Resonance Spectroscopy of Single Silver Triangular Nanoprisms. *Nano Lett.* **2006**, *6*, 2060-2065.

(56) Kelly, K. L.; Coronado, E.; Zhao, L. L.; Schatz, G. C. The Optical Properties of Metal Nanoparticles: The Influence of Size, Shape, and Dielectric Environment. *J. Phys. Chem. B* **2003**, *107*, 668-677.

(57) Bae, Y.; Kim, N. H.; Kim, M.; Lee, K. Y.; Han, S. W. Anisotropic Assembly of Ag Nanoprisms. *J. Am. Chem. Soc.* **2008**, *130*, 5432-5433.

(58) Murphy, C. J.; Sau, T. K.; Gole, A. M.; Orendorff, C. J.; Gao, J.; Gou, L.; Hunyadi, S. E.; Li, T. Anisotropic Metal Nanoparticles: Synthesis, Assembly, and Optical Applications. *J. Phys. Chem. B* **2005**, *109*, 13857-13870.

(59) Rosen, D. A.; Tao, A. R. Modeling the Optical Properties of Bowtie Antenna Generated By Self-Assembled Ag Triangular Nanoprisms. *ACS Appl. Mater. Interfaces* **2014**, *6*, 4134-4142.

(60) Metraux, G. S.; Mirkin, C. A. Rapid thermal synthesis of silver nanoprisms with chemically tailorable thickness. *Adv. Mater.* **2005**, *17*, 412-415.

(61) Wang, H.; Cui, X.; Guan, W.; Zheng, X.; Zhao, H.; Wang, Z.; Wang, Q.; Xue, T.; Liu, C.; Singh, D. J.; Zheng, W. Kinetic effects in the photomediated synthesis of silver nanodecahedra and nanoprisms: combined effect of wavelength and temperature. *Nanoscale* **2014**, *6*, 7295-7302.

(62) Jin, R. C.; Cao, Y. C.; Hao, E. C.; Metraux, G. S.; Schatz, G. C.; Mirkin, C. A. Controlling anisotropic nanoparticle growth through plasmon excitation. *Nature* **2003**, *425*, 487-490.

(63) Xue, C.; Mirkin, C. A. pH-switchable silver nanoprism growth pathways. *Angew. Chem. Int. Ed.* **2007**, *46*, 2036-2038.

(64) Pich, A.; Karak, A.; Lu, Y.; Ghosh, A. K.; Adler, H. J. P. Preparation of hybrid microgels functionalized by silver nanoparticles. *Macromol. Rapid Commun.* **2006**, *27*, 344-350.

(65) Farooqi, Z. H.; Siddiq, M. Temperature-Responsive Poly(N-Isopropylacrylamide-Acrylamide-Phenylboronic Acid) Microgels for Stabilization of Silver Nanoparticles. *J. Dispersion Sci. Technol.* **2015**, *36*, 423-429.

(66) Ding, T.; Valev, V. K.; Salmon, A. R.; Forman, C. J.; Smoukov, S. K.; Scherman, O. A.; Frenkel, D.; Baumberg, J. J. Light-induced actuating nanotransducers. *Proc. Natl. Acad. Sci. U. S. A.* **2016**, *113*, 5503-5507.

Chapter 6. SUMMARY AND FUTURE WORK

6.1 SUMMARY

This dissertation focuses on the assembly and characterization of stimuli-responsive reconfigurable plasmonic nanomaterials. In particular, the thesis explores the optical properties of azobenzene-modified DNA-linked gold nanoparticle dimers on photo-triggered structural reconfiguration, and the thermally-induced optical and plasmonic behavior of silver nanoprism composites with PNIPAM microgels.

The performance of photoresponsive DNA-linked nanoparticles is governed by the *trans*-to-*cis* photoisomerization efficiency as well as thermal relaxation rate of azobenzene photoswitches embedded in the DNA backbone. Chapter 3 describes that the photoisomerization quantum yields of azobenzene in different DNA sequences show a temperature-dependent behavior, which can be tuned by the melting temperature of the host DNA. This study suggests that the neighboring DNA base pairs constrict the free volume available to the azobenzene and hinders the broader motion (rotation or hula-twist) associated with *trans*-to-*cis* photoconversion mechanism. As the DNA duplex starts to dehybridize on increasing the temperature, it creates larger free volume and flexibility around the azobenzene that facilitates the twisting motion and results in higher photoisomerization quantum yields. Thus, the change in the quantum yield with temperature is governed by the melting transition of the host DNA. In contrast to the photoisomerization process, the reverse *cis*-to-*trans* thermal isomerization of azobenzene does not show any sequence-dependent behavior, suggesting that the reverse thermal relaxation occurs through an inversion pathway, probably in a locally dehybridized pocket in the DNA, and so, is not affected by the nearby base pairs. These findings allow us to tune the DNA sequence-specific

designs of the nanostructures to enhance their efficiency as photoresponsive reconfigurable materials.

Followed by the study on fundamental photophysical properties of azobenzene-modified DNAs, we turned to study discrete optically reconfigurable nanostructures by employing the azobenzene-modified DNA chemistry. Chapter 4 demonstrates the assembly of asymmetric plasmonic dimer consisting of a 100 nm and a 50 nm gold nanoparticle connected with an azobenzene-modified hairpin DNA motif that shows a light-induced reversible actuation of the near-field plasmonic coupling upon UV and blue light exposure. Reversible photoisomerization of the azobenzene units that are incorporated in the stem part of the hairpin DNA sequence results in photoreconfigurable interparticle distances that gives rise to a reversible plasmonic shift in longitudinal resonance peak of the single nanoparticle dimer scattering spectra. The DNA-linked nanoparticle dimers can be potentially used as building blocks in optically reprogrammable nanomaterials to achieve a remote control of structural and functional properties without chemical reagents.

Chapter 5 describes the assembly and characterization of another stimuli-responsive reconfigurable plasmonic nanomaterial that combines anisotropic silver nanoprisms with thermally sensitive PNIPAM microgels. Thermally reversible swelling-shrinking of the PNIPAM microgels leads to a temperature-induced conformational switch of the nanomaterials between the expanded and collapsed states exhibiting significantly distinct extinction and scattering features at low and high temperatures. The thermo-responsive optical properties of the nanocomposites can be tuned in the visible and near IR region of the spectra by varying the size and the loading density of the nanoprisms on the PNIPAM microgel. Moreover, temperature-induced large reversible

thermochromic shifts and substantial change in the NIR scattering intensity of the hybrid materials make them potentially useful in sensing and imaging applications.

6.2 FUTURE WORK

Assembly of One-Dimensional Photoswitchable Nanostructures

Chapter 4 discovers that azobenzene-modified DNAs can be successfully used to design photoswitchable gold nanoparticle dimers. It would be worth to use these discrete dimers as building blocks to design optically reprogrammable one-dimensional plasmonic nanostructures. The DNA-functionalized gold nanoparticles can be used to create Janus-type particles and the sequence complementarity of the DNAs will be used to organize the particles in a controlled fashion to create one dimensional arrangement of reconfigurable shapes and size. The azobenzene-modified DNAs will act as the photo-triggered units, such that the reversible *trans*-to-*cis* photoisomerization would lead to an opening and closing of the ring/ loop structure of the nanoparticles assembly. Dark field optical microscopy and electron microscopy can be used to characterize these nanostructures before and after photoswitching. The distinct optical signatures associated with the assembly and disassembly process of the nanostructure can be potentially useful in bio-sensing applications and diagnostic assays.

To further advance the characterization of such reconfigurable plasmonic nanostructures, we can also investigate the dynamic evolution of DNA-linked nanoparticle assemblies at a single particle level and directly image the intrinsic dynamic motion along with the photo-triggered motion of the structural transformation of the optically reconfigurable nanostructures using dynamic TEM and liquid cell electron microscopy. Hopefully, my research work on the photoswitchable DNA-linked dimers in combination with these future advanced studies on similar

materials can be used in the long run to improve the application of optically reprogrammable DNA-nanomaterials in constructing regenerative low cost sensors, taggants and biomarkers.

Photoresponsive Polymer/Nanoparticle Hybrids

The research on thermally responsive PNIPAM/nanoparticle hybrid microgels in Chapter 5 can be further extended to achieve a wider range of color change and tunability with temperature by varying the size, shape and composition of the nanoparticles.

More importantly, we can also design similar hybrid plasmonic nanostructures that allow tailorability of the optical responses through exposure to light. We propose fabrication of photosensitive polymer microgels by introducing a photoacid (e.g. ortho nitrobenzaldehyde) in the poly(N-isopropylacrylamide) copolymerized with poly(acrylicacid) (PNIPAM-coPAA) microgels. Light-induced deprotonation of the photoacid will change the pH of the microgel environment causing it to deswell into a collapsed state. Combining optically active plasmonic nanoparticles of various sizes and shapes with such photo-responsive microgels will allow us to remotely modulate their plasmonic properties on reconfiguration of the structure with light, instead of temperature and pH.

APPENDIX A

Supporting Information for Chapter 3

Experimental Methods

Materials

Unmodified oligonucleotides and azobenzene-modified oligonucleotides (see Table 3.1 in for sequences) were synthesized and purified with HPLC technique by Integrated DNA Technologies Inc. (Coralville, IA). ACS grade reagents like sodium chloride (NaCl), disodium hydrogen phosphate (Na_2HPO_4), potassium dihydrogen phosphate (KH_2PO_4), sodium azide (NaN_3) were purchased from Sigma Aldrich (St. Louis, MO) and were used without any further purification. Water used in the experiments were deionized to 18.2 MΩ using a Millipore filtration system.

Preparation of double-stranded DNA (dsDNA) solutions for quantum yield measurement

To prepare the DNA solutions for the experiments, freshly-prepared 10mM phosphate buffer solution containing 100mM of NaCl and 0.05% of sodium azide was added to dissolve the required amount of lyophilized DNA and adjust the solution to ~30μM of oligonucleotide concentration. The absorbance of the DNA solution at 260 nm was measured at room temperature with an Agilent 8453 UV-Vis spectrometer to obtain the exact concentration. To prepare the dsDNA solution, equal molar amounts of the azobenzene-modified DNA and the unmodified (complementary or mismatched) DNA solutions were mixed at room temperature. The mixture was then heated up to 95°C, allowed to sit for 5 minutes and then slowly cooled down to room temperature for annealing. All the DNA solutions were stored at 4°C before use.

***Trans*-to-*cis* photoisomerization quantum yield measurements**

We have followed the same experimental set up and method from our previous work[1] to measure the *trans*-to-*cis* photoisomerization quantum yield of azobenzene in the DNA sequences shown in Table 1 at different temperatures. Typically, the DNA solution was irradiated with 330 nm UV LEDs in a home-made aluminum sample chamber with light accessible windows. The temperature of the DNA solution was raised by using a heating stage attached to the chamber and then was maintained using a calibrated temperature controller connected to the stage. The temperature of the DNA solution as a function of the temperature controller set point was calibrated using a thermometer.

Three 330 nm UV LEDs (UVTOP325HS, fwhm < 10 nm, Sensor Electronic Technology, Inc.) were aligned at ~4 cm away from the cuvette holder and warmed up to equilibrate for about an hour (see Figure 3.1(c)). The irradiation intensity was measured by a calibrated silicon photodiode and was set to 0.26-0.30 mW/cm^2 at the position of the cuvette. The aluminum stage was heated up to the desired temperature prior to the measurement. The DNA solution in a quartz fluorescence micro cuvette with a 1 cm optical path length was then placed on the sample stage in the dark for an hour to allow thermal equilibration before UV irradiation. The solution was constantly stirred during the experiment with a magnetic stir bar. During UV illumination, UV-Vis absorbance spectra of the DNA solution were measured every 1 minute for the first 20 minutes, every 2 minutes for next 20 minutes and then every 5 minutes till two hours with an Agilent 8453 UV-Vis spectrometer. The low intensity radiation from the spectrometer light source does not significantly perturb the photoisomerization of the azobenzene under these conditions.[1] The calculation of the temperature dependent azobenzene photoisomerization quantum yields at 330 nm (ϕ_{trans}) for different sequences is discussed in the Supplementary Text below.

Cis-to-*trans* reverse thermal isomerization study

In order to study the *cis*-to-*trans* thermal isomerization of azobenzene in different DNA sequences as a function of temperature, we used the experimental set up described above to bring the *trans*-to-*cis* photoreaction to photostationary state by irradiating the DNA solution with 330 nm UV LEDs for typically about two hours. UV-Vis absorbance spectra of the solution were recorded before and after the photostationary state was attained. The UV light source was then turned off and the absorbance at 330 nm was measured every 20 minutes while the solution was sitting in the dark till two hours. The determination of the first order rate constants (k_{therm}) and the activation energies (E_a) of the thermal back reaction kinetics for the DNA sequences at different temperatures is described in the Supplementary Text.

Melting temperature (T_m) measurements

We used thermal denaturation mode in an Agilent 8453 UV-Vis spectrometer coupled with a Peltier temperature controller to measure the melting temperature of the azobenzene-modified dsDNA solutions. The solution was heated from 10°C to 96°C, at increments of 2°C with a hold time of 5 minutes and absorbance spectra were taken at each step. Melting curves were obtained by plotting the absorbance at 260 nm as a function of temperature of the solution and T_m was calculated from the maximum in the first derivative of the melting curve (see Figure S4).

Supplementary Text

Trans-to-*Cis* Photoisomerization Quantum Yield Calculation

We use equation 1 from Chapter 1 to obtain the azobenzene photoisomerization quantum yields for the azobenzene-modified DNAs.[1,2]

$$\frac{\mathbf{d}[\boldsymbol{cis}]_{\mathbf{t}}}{\mathbf{dt}}$$

$$= \frac{\mathbf{I}^{\boldsymbol{\lambda}}\,\mathbf{l}\left(\mathbf{1}-\mathbf{10}^{-\mathbf{abs}_{\mathbf{t}}^{\boldsymbol{\lambda}}}\right)\phi_{\boldsymbol{trans}}^{\boldsymbol{\lambda}}\boldsymbol{\varepsilon}_{\boldsymbol{trans}}^{\boldsymbol{\lambda}}}{\mathbf{V}\,\mathbf{abs}_{\mathbf{t}}^{\boldsymbol{\lambda}}}\left([\boldsymbol{trans}]_{\mathbf{0}}-[\boldsymbol{cis}]_{\mathbf{t}}\right)-\frac{\mathbf{I}^{\boldsymbol{\lambda}}\mathbf{l}\left(\mathbf{1}-\mathbf{10}^{-\mathbf{abs}_{\mathbf{t}}^{\boldsymbol{\lambda}}}\right)\phi_{\boldsymbol{cis}}^{\boldsymbol{\lambda}}\boldsymbol{\varepsilon}_{\boldsymbol{cis}}^{\boldsymbol{\lambda}}}{\mathbf{V}\,\mathbf{abs}_{\mathbf{t}}^{\boldsymbol{\lambda}}}[\boldsymbol{cis}]_{\mathbf{t}}$$

$$-\mathbf{k}_{\mathbf{therm}}[\boldsymbol{cis}]_{\mathbf{t}} \qquad (\mathbf{S1})$$

For our studies we followed two different approaches to obtain the quantum yields of the azobenzene-modified DNA sequences at different temperatures. The first method ignores the *cis*-to-*trans* thermal isomerization of azobenzene even at higher temperatures and the second approach includes the effect of the thermal isomerization to calculate the photoisomerization quantum yields at various temperatures. Below we discuss the calculation of the photoisomerization quantum yield of azobenzene using these two methods.

We define the photokinetic factor $\mathbf{F_t}$ as

$$\mathbf{F_t} = \frac{\left(\mathbf{1}-\mathbf{10}^{-\mathbf{abs}_{\mathbf{t}}^{\boldsymbol{\lambda}}}\right)}{\mathbf{abs}_{\mathbf{t}}^{\boldsymbol{\lambda}}} \qquad (\mathbf{S2})$$

which takes into account the change in the solution absorbance during photoisomerization and expresses the irradiation time in terms of photons absorbed by the solution. We rewrite the equation $(\mathbf{1})$ as

$$\frac{\mathbf{d}[\boldsymbol{cis}]_{\mathbf{t}}}{\mathbf{dt}} = \frac{\mathbf{I}^{\boldsymbol{\lambda}}\,\mathbf{l}\,\mathbf{F_t}\,\phi_{\boldsymbol{trans}}^{\boldsymbol{\lambda}}\,\boldsymbol{\varepsilon}_{\boldsymbol{trans}}^{\boldsymbol{\lambda}}}{\mathbf{V}}\left([\boldsymbol{trans}]_{\mathbf{0}}-[\boldsymbol{cis}]_{\mathbf{t}}\right)-\frac{\mathbf{I}^{\boldsymbol{\lambda}}\mathbf{l}\,\mathbf{F_t}\,\phi_{\boldsymbol{cis}}^{\boldsymbol{\lambda}}\,\boldsymbol{\varepsilon}_{\boldsymbol{cis}}^{\boldsymbol{\lambda}}}{\mathbf{V}}[\boldsymbol{cis}]_{\mathbf{t}}$$

$$-\mathbf{k}_{\mathbf{therm}}[\boldsymbol{cis}]_{\mathbf{t}} \qquad (\mathbf{S3})$$

At the photostationary state $(\mathbf{t}=\infty)$ the photochemical rate of *trans*-to-*cis* conversion is equal to the sum of the photochemical and thermal rate of *cis*-to-*trans* isomerization. Therefore,

$$\frac{\mathbf{d}[\boldsymbol{cis}]_{\infty}}{\mathbf{dt}} = \mathbf{0} \qquad (\mathbf{S4})$$

where, $[\boldsymbol{cis}]_\infty$ is the concentration of *cis*-azobenzene at the photostationary state. Solving for $\phi_{\boldsymbol{cis}}^{\boldsymbol{\lambda}}$ we get the following

$$\phi_{\boldsymbol{cis}}^{\boldsymbol{\lambda}} = \frac{\phi_{\boldsymbol{trans}}^{\boldsymbol{\lambda}}\boldsymbol{\varepsilon}_{\boldsymbol{trans}}^{\boldsymbol{\lambda}}}{\boldsymbol{\varepsilon}_{\boldsymbol{cis}}^{\boldsymbol{\lambda}}} \frac{[\boldsymbol{trans}]_0 - [\boldsymbol{cis}]_\infty}{[\boldsymbol{cis}]_\infty} - \frac{\mathbf{k_{therm}\, V}}{\mathbf{I^{\lambda}\, l\, F_\infty}\boldsymbol{\varepsilon}_{\boldsymbol{cis}}^{\boldsymbol{\lambda}}} \quad (\mathbf{S5})$$

By neglecting the thermal back reaction term in the equation

$$\phi_{\boldsymbol{cis}}^{\boldsymbol{\lambda}} = \frac{\phi_{\boldsymbol{trans}}^{\boldsymbol{\lambda}}\boldsymbol{\varepsilon}_{\boldsymbol{trans}}^{\boldsymbol{\lambda}}}{\boldsymbol{\varepsilon}_{\boldsymbol{cis}}^{\boldsymbol{\lambda}}} \frac{[\boldsymbol{trans}]_0 - [\boldsymbol{cis}]_\infty}{[\boldsymbol{cis}]_\infty} \quad (\mathbf{S6})$$

Putting the above expression of $\phi_{\boldsymbol{cis}}^{\boldsymbol{\lambda}}$ from equation (**6**) into equation (**3**) and replacing the fraction of *cis*-azobenzene $\frac{[\boldsymbol{cis}]_t}{[\mathbf{trans}]_0}$ as $\mathbf{y_t}$ we get the following solution after integrating the rate expression

$$\ln\frac{\mathbf{y}_\infty - \mathbf{y_t}}{\mathbf{y}_\infty - \mathbf{y_0}} = -\frac{\mathbf{I^{\lambda}\, l}\, \phi_{\boldsymbol{trans}}^{\boldsymbol{\lambda}}\boldsymbol{\varepsilon}_{\boldsymbol{trans}}^{\boldsymbol{\lambda}}}{\mathbf{V\, y}_\infty}\int_{t_0}^{t}\mathbf{F_t}\,\mathbf{dt}$$

$$= -\frac{\mathbf{I^{\lambda}\, l}\, \phi_{\boldsymbol{trans}}^{\boldsymbol{\lambda}}\boldsymbol{\varepsilon}_{\boldsymbol{trans}}^{\boldsymbol{\lambda}}}{\mathbf{V\, y}_\infty}\int_{t_0}^{t}\frac{\left(\mathbf{1} - \mathbf{10}^{-\mathbf{abs}_t^{\lambda}}\right)}{\mathbf{abs}_t^{\lambda}}\mathbf{dt} \quad (\mathbf{S7})$$

$$\mathbf{y_t} = (\mathbf{y_0} - \mathbf{y}_\infty)\,\mathbf{exp}(-\mathbf{Ax_t}) + \mathbf{y}_\infty \quad (\mathbf{S8})$$

where, $\mathbf{x_t} = \int_{t_0}^{t}\frac{\left(\mathbf{1}-\mathbf{10}^{-\mathbf{abs}_t^{\lambda}}\right)}{\mathbf{abs}_t^{\lambda}}\mathbf{dt}$ is the integrated photokinetic factor (IPF) at time $\mathbf{t}$, which takes care of the fact that all the molecules absorbs at the irradiation wavelength and the absorbance changes as a function of time.$\mathbf{A} = \frac{\mathbf{I^{\lambda}\, l}\, \phi_{\boldsymbol{trans}}^{\boldsymbol{\lambda}}\boldsymbol{\varepsilon}_{\boldsymbol{trans}}^{\boldsymbol{\lambda}}}{\mathbf{V\, y}_\infty}$ is a pre-factor that relates to *trans*-to-*cis* photoisomerization quantum yield. We measure the absorbance of the solution at 330 nm as a function of time and use the values for $\boldsymbol{\varepsilon}_{\boldsymbol{trans}}^{\mathbf{330}}$ and $\boldsymbol{\varepsilon}_{\boldsymbol{cis}}^{\mathbf{330}}$ from the literature[2] to determine the concentration of the *cis*-azobenzene at those time points. We plot the fraction of *cis*-azobenzene as a function of the integrated photokinetic factor and fit the experimental data with equation (**S8**)

(same as the equation $(\mathbf{1})$ in the main text) using Igor Pro 6.3.6.4. The quantum yield value is then calculated from the values of $\mathbf{A}$ and $\mathbf{y}_\infty$ obtained from the fit.

$$\phi^{\lambda}_{trans} = \frac{\mathbf{V}\,\mathbf{y}_\infty \mathbf{A}}{\mathbf{I}^{\lambda}\,\mathbf{l}\,\boldsymbol{\varepsilon}^{\lambda}_{trans}} \qquad (\mathbf{S9})$$

We extract the rate constant for *trans*-to-*cis* photoisomerization process, $\mathbf{k_{photo}}$, from the quantum yield values using the following relation:

$$\mathbf{k_{photo}} = \boldsymbol{\varepsilon}^{\lambda}_{trans}\,\mathbf{I}^{\lambda}\,\phi^{\lambda}_{trans} \qquad (\mathbf{S10})$$

Calculation of the rate constant for *cis*-to-*trans* thermal isomerization of azobenzene

The thermal relaxation of azobenzene follows a first order kinetics,

$$\frac{\mathbf{d}[cis]_{\mathbf{t}}}{\mathbf{dt}} = -\mathbf{k_{therm}}[cis]_{\mathbf{t}} \qquad (\mathbf{S11})$$

$$\frac{\mathbf{d}}{\mathbf{dt}}\left(\frac{[cis]_t}{[trans]_0}\right) = -\mathbf{k_{therm}}\frac{[cis]_t}{[trans]_0} \qquad (\mathbf{S12})$$

Substituting the fraction of *cis*-azobenzene $\frac{[cis]_t}{[trans]_0}$ at time t during thermal isomerization as $\mathbf{y}$ in the above equation,

$$\frac{\mathbf{dy}}{\mathbf{dt}} = -\mathbf{k_{therm}}\,\mathbf{y} \qquad (\mathbf{S13})$$

$$\frac{\mathbf{dy}}{\mathbf{y}} = -\mathbf{k_{therm}}\,\mathbf{dt} \qquad (\mathbf{S14})$$

Integrating the above differential rate equation, we get

$$\ln\frac{\mathbf{y}}{\mathbf{y_0}} = -\mathbf{k_{therm}}\,\mathbf{t} \qquad (\mathbf{S15})$$

where $\mathbf{y_0}$ is the initial fraction of *cis*-azobenzene. During the thermal isomerization we calculate the fraction of *cis*-azobenzene from the absorbance of the solution at 330 nm as a function of time.

We plot $\mathbf{ln}\frac{\mathbf{y}}{\mathbf{y_0}}$ against time ($\mathbf{t}$) and fit the data with the linear equation ($\mathbf{S15}$) in Igor Pro 6.3.6.4 to obtain the thermal isomerization rate constant from the slope of the straight line.

The kinetics of the thermal isomerization of azobenzene linked to the DNA sequences at 27°C is too slow to be measured accurately using our experimental approach. So, we determine rate constants for different azobenzene-modified DNA sequences at 37°C, 45°C, 55°C, 65°C and 75°C. To prevent the *cis*-to-*trans* reverse photo-induced isomerization caused by the visible radiation from the spectrometer while measuring the thermal isomerization rate constant, absorbance spectra of the solution were taken only after every 20 minutes. We observed that collecting the absorbance spectra more frequently (every 5 or 10 minutes) resulted in a higher thermal isomerization rate of *cis*-azobenzene during our measurements (steeper slopes for the red and yellow lines in Figure S2.), indicating that reverse photoisomerization is induced by the spectrometer light. However, when the absorbance was measured every 30 minutes, the rate did not change any further (equal slopes for green and blue lines in Figure S2). Although this effect is significant at lower temperature, more frequent exposure to the spectrometer radiation does not affect the measurement at higher temperature (Figure S2.) due to a faster thermal isomerization kinetics of azobenzene.

The *cis*-to-*trans*-thermal isomerization kinetics follows an Arrhenius behavior and we determine the activation energy ($\mathbf{E_a}$) and frequency factor ($\mathbf{A}$) for the process by plotting $\mathbf{ln(k_{therm})}$ versus $\mathbf{1/T}$ for all the sequences.

$$\mathbf{ln(k_{therm})} = \mathbf{ln\,A} - \frac{\mathbf{E_a}}{\mathbf{RT}} \qquad (\mathbf{S16})$$

Once we obtain the $\mathbf{k_{therm}}$ values of the DNA sequences at different temperatures we use the expression of ϕ_{cis}^{λ} from equation ($\mathbf{S5}$) to include the thermal back reaction into the differential rate equation ($\mathbf{S3}$) which is then solved numerically using a variable step size ordinary differential equation (ODE) integrator in scipy for Python. The numerical solution to equation ($\mathbf{S3}$) is fit to

the experimental data by varying the parameters $\phi_{trans}^{\lambda}$and $\mathbf{y}_{\infty}$. The initial guess for $\phi_{trans}^{\lambda}$was determined by the value already obtained from the respective fits using equation (**S8**) that neglects the effect of reverse thermal isomerization. The initial guess for $\mathbf{y}_{\infty}$ was set as the average value of the fraction of *cis*-azobenzene that was determined from the region of the data where the decay rate is approximately zero and boundaries on $\mathbf{y}_{\infty}$ were constrained within the standard deviation. We find that the fit and the fitting parameters, that includes ϕ_{trans}^{λ} and $\mathbf{y}_{\infty}$, obtained in this numerical method is practically the same as the fit and values obtained using equation (**S8**) in Igor Pro, even at higher temperatures. Thus, we observe that the *trans*-to-*cis* photoisomerization quantum yield of azobenzene-modified DNAs is not affected by the *cis*-to-*trans* thermal isomerization process within the temperature range of 27°C-85°C under the UV irradiation intensity of 0.26-0.30 mW/cm^2. It is also worth mentioning that under the UV irradiation intensity we used in our experiments, the photoisomerization rate constants, which are extracted from the quantum yield values, are significantly higher compared to the first order thermal rate constants for the *cis*-to-*trans* isomerization at all the temperatures we have studied (Figure S3 (b)). So, we can ignore the thermal isomerization process while calculating the photoisomerization quantum yield even at higher temperatures for our purposes. However, if the intensity of the UV exposure is below the limit of 0.04-0.05 mW/cm^2 under the same experimental conditions, the thermal isomerization of azobenzene cannot be neglected anymore, especially at higher temperatures.

Supplementary Figures

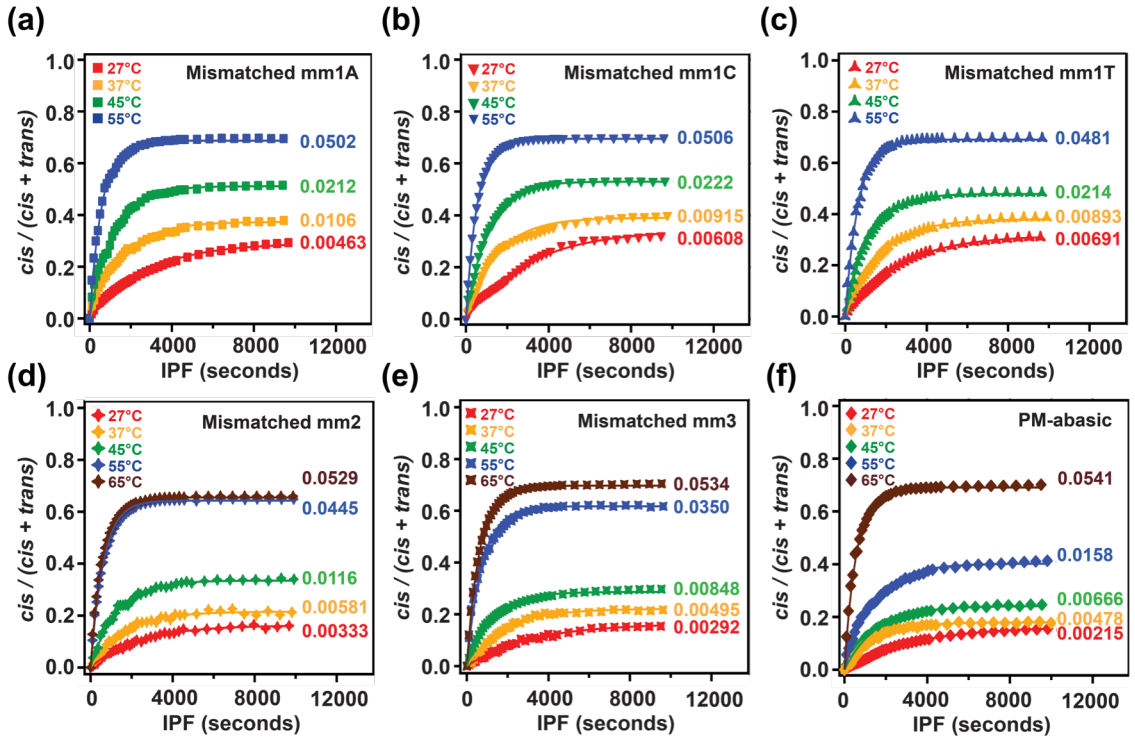

Figure S1. Plot of fraction of *cis*-azobenzene as a function of integrated photokinetic factor (IPF) for the mismatched ds-DNA sequences with the following non-complementary base pair located next to the azobenzene: (a) *C*-*A* mismatch (squares), (b) *C*-*C* mismatch (inverted triangle) and (c) *C*-*T* mismatch (triangular star) at 27°C (red), 37°C (yellow), 45°C (green) and 55°C (blue). The solid traces are the experimental fits to equation (**8**) and the average quantum yield values are written next to the respective curves. Similar plots are shown for dsDNA sequences (d) mm2 and (e) mm3, where the mismatched base pair is located second and third to the azobenzene respectively, and (f) PM-abasic where an abasic site is located directly across the azobenzene at 27°C (red), 37°C (yellow), 45°C (green), 55°C (blue) and 65°C (brown).

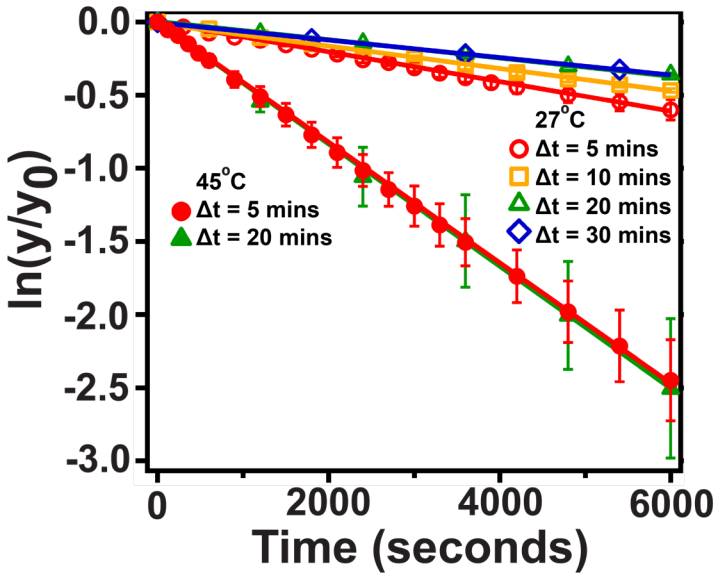

Figure S2. Plot of $\ln(y/y_0)$ vs. time to determine the first order rate constants for *cis*-to-*trans* thermal isomerization of azobenzene in isooctane showing the effect of the reverse *cis*-to-*trans* photoreaction caused by the visible radiation from the spectrometer. We monitor the rate of the thermal back reaction of free azobenzene solution in different experiments by taking the absorbance measurements at different time intervals (Δt). At 27°C, the reverse thermal isomerization appears to be faster (greater slope) when we measure the absorbance every 5 minutes (red trace through circles) compared to every 10 minutes (yellow trace through squares) which indicates that frequent exposure to the visible radiation from the UV-vis spectrometer causes reverse photoisomerization and results in a higher calculated thermal isomerization rate constant. The rate of the thermal back reaction is not affected by the spectrometer light if we take absorbance spectra at every 20 minutes or more. At higher temperature (45ºC), since the thermal isomerization is faster, the effect of reverse photoisomerization induced by the spectrometer radiation becomes negligible.

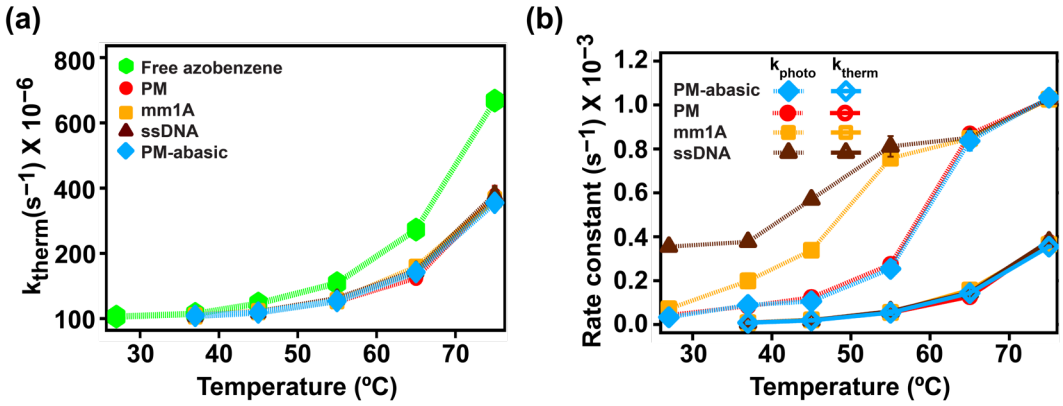

Figure S3. (a) Plot of thermal isomerization rate constants vs. temperature for free azobenzene in isooctane and azobenzene attached to different DNA sequences (PM, PM-abasic, mm1A, and ssDNA) which indicates that free azobenzene thermal isomerization is always faster than the azobenzene in DNA sequences. (b) Plot of rate constants of *trans*-to-*cis* photoisomerization (solid symbols) and the *cis*-to-*trans* thermal isomerization (hollow symbols) of azobenzene for the same set of DNA sequences at various temperatures showing that the kinetics of photoisomerization is always faster than that of the thermal isomerization under our experimental conditions.

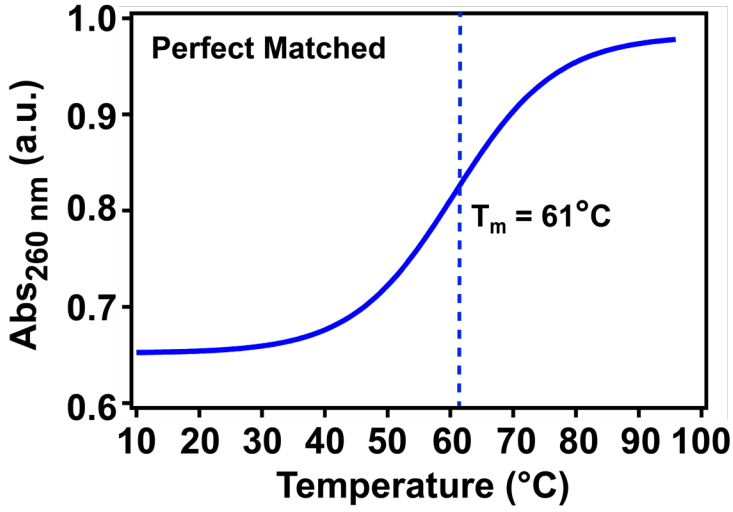

Figure S4. An example of DNA melting curve: plot of the absorbance at 260 nm as a function of temperature to obtain the melting temperature (T_m) of azobenzene-modified dsDNA. The plot shown here corresponds to the perfect complementary dsDNA (PM) with T_m = 61 ˚C.

Table S1: List of experimental values for *trans*-to-*cis* photoisomerization quantum yields (ϕ_{trans}) at 330 nm and rate constants of *cis*-to-*trans* thermal isomerization ($\mathbf{k_{therm}}$), half-life of the *cis* isomer ($\mathbf{t_{1/2}}$ **(*cis*))** of azobenzene in different DNA sequences at different temperatures

Sequence	**t (°C)**	ϕ_{trans}	$\mathbf{k_{therm}}$	$\mathbf{t_{1/2}}$ **(*cis*) in hrs**
ssDNA	27	0.0221 ± 0.000101	--	--
	37	0.0260 ± 0.000161	$(8.39 \pm 0.178) \times 10^{-6}$	23.0
	45	0.0377 ± 0.000121	$(1.94 \pm 0.104) \times 10^{-5}$	9.94
	55	0.0507 ± 0.000194	$(6.02 \pm 0.615) \times 10^{-5}$	3.20
	65	0.0544 ± 0.00185	$(1.46 \pm 0.0812) \times 10^{-4}$	1.32
	75	0.0617 ± 0.00154	$(3.79 \pm 0.264) \times 10^{-4}$	0.508
	85	0.0695 ± 0.00148	--	--
PM	27	0.00272 ± 0.000175	--	--
	37	0.00513 ± 0.000121	$(8.77 \pm 0.283) \times 10^{-6}$	22.0
	45	0.00787 ± 0.00214	$(2.11 \pm 0.0728) \times 10^{-5}$	9.14
	55	0.0173 ± 0.00136	$(5.35 \pm 0.438) \times 10^{-5}$	3.60
	65	0.0534 ± 0.00103	$(1.27 \pm 0.127) \times 10^{-4}$	1.52
	75	0.0614 ± 0.00142	$(3.75 \pm 0.317) \times 10^{-4}$	0.513
	85	0.0686 ± 0.00216	--	--
PM-abasic	27	0.00215 ± 0.000106	--	--
	37	0.00478 ± 0.000145	$(8.38 \pm 0.643) \times 10^{-6}$	23.0
	45	0.00666 ± 0.000161	$(1.85 \pm 0.156) \times 10^{-5}$	10.4

	55	0.0158 ± 0.00232	$(5.38 \pm 0.113) \times 10^{-5}$	3.58
	65	0.0541 ± 0.00305	$(1.43 \pm 0.262) \times 10^{-4}$	1.35
	75	0.0626 ± 0.00152	$(3.55 \pm 0.0293) \times 10^{-4}$	0.542
mm1A	27	0.00463 ± 0.000137	--	--
	37	0.0106 ± 0.000144	$(8.40 \pm 0.143) \times 10^{-6}$	22.9
	45	0.0212 ± 0.00175	$(2.12 \pm 0.0847) \times 10^{-5}$	9.09
	55	0.0502 ± 0.00106	$(5.47 \pm 0.173) \times 10^{-5}$	3.52
	65	0.0546 ± 0.00104	$(1.57 \pm 0.167) \times 10^{-4}$	1.22
	75	0.0615 ± 0.00144	$(3.65 \pm 0.0607) \times 10^{-4}$	0.527
	85	0.0696 ± 0.00215	--	--
mm1C	27	0.00608 ± 0.000521	--	--
	37	0.00915 ± 0.00105	--	--
	45	0.0222 ± 0.00194	--	--
	55	0.0506 ± 0.00232	--	--
mm1T	27	0.00691 ± 0.000633	--	--
	37	0.00893 ± 0.000501	--	--
	45	0.0214 ± 0.00157	--	--
	55	0.0481 ± 0.00244	--	--
mm2	27	0.00333 ± 0.000107	--	--
	37	0.00581 ± 0.000116	--	--
	45	0.0116 ± 0.000105	--	--
	55	0.0445 ± 0.000375	--	--

	65	0.0529 ± 0.00329	--	--
	75	0.0621 ± 0.000695	--	--
mm3	27	0.00292 ± 0.000105	--	--
	37	0.00495 ± 0.000105	--	--
	45	0.00848 ± 0.000861	--	--
	55	0.0350 ± 0.00181	--	--
	65	0.0534 ± 0.00309	--	--
	75	0.0626 ± 0.00142	--	--
Azobenzene in isooctane	27	0.112 ± 0.0114	$(6.12 \pm 0.382) \times 10^{-6}$	31.5
	37	--	$(1.46 \pm 0.881) \times 10^{-5}$	13.2
	45	0.109 ± 0.00912	$(4.63 \pm 0.143) \times 10^{-5}$	4.16
	55	--	$(1.09 \pm 0.251) \times 10^{-4}$	1.77
	65	0.118 ± 0.0131	$(2.73 \pm 0.143) \times 10^{-4}$	0.705
	75	--	$(6.68 \pm 0.0628) \times 10^{-4}$	0.288

Supplementary References

(1) Yan, Y.; Wang, X.; Chen, J. I. L.; Ginger, D. S. Photoisomerization Quantum Yield of Azobenzene-Modified DNA Depends on Local Sequence. *JACS* **2013**, *135*, 8382-8387.

(2) Zimmerman, G.; Chow, L. Y.; Paik, U. J. The Photochemical Isomerization of Azobenzene1. *JACS* **1958**, *80*, 3528-3531.

APPENDIX B

Supporting Information for Chapter 4

Experimental Methods

Materials

The following modified DNA sequences were synthesized and HPLC-purified by Integrated DNA Technologies, Coralville, IA.

Seq1: 5'--S-S-AAA AAA AAA ACG CAT TCA GGA T-3'

Azo-seq2: 5'--S-S-TCT CAA CTC GTA CGT TAG TTC ATT TTT G***X***AA ***X***CT***X***A A***X***CG CGA AAG ATC CTG AAT GCG-3' (***X*****:** azobenzene)

Colloidal solutions of 50 nm and 100 nm diameter gold nanoparticles (AuNP) were purchased from BBI Solutions and used without any further purification. Molecular biology reagents like dithiothreitol (DTT, > 99.0%), Tris-EDTA buffer (pH 7.4), phosphate buffered saline solution (10 X concentrate), sodium dodecyl sulfate solution (10 % in H_2O) and ACS grade reagents like sodium chloride (NaCl), sodium azide (NaN_3), (3-Aminopropyl) triethoxysilane (99 %) were purchased from Sigma Aldrich (St. Louis, MO).

All water used in the solutions was deionized to 18 MΩ using Millipore filtration system. All the solutions were filtered through 0.2-micron cellulose acetate filters prior to all experiments and the buffer solutions were prepared right before use.

Reduction of the dithiol linkage in the DNA sequences

The thiol-modified oligonucleotides, purchased from IDT DNA were obtained in a protected form, where the Sulphur atom is oxidized to S=S bond, that was reduced by dithiothreitol (DTT) to attach them onto the gold nanoparticle surface. Prior to gold nanoparticle functionalization, a

100 μM solution of the oligonucleotide was prepared in 0.01 M of Tris-EDTA (TE) buffer solution, containing 10 mM of DTT, and was left for 20 minutes with constant stirring. The reduced oligonucleotide was then separated through a Micro Bio-Spin 6 column (Bio-Rad Laboratories, Inc.) and was used immediately.

Assembly of gold nanoparticle dimers on a glass substrate

The dimer assembly procedure is adapted from our previous work.[39] 100 nm gold nanoparticles were first anchored on a silanized ITO glass substrate, followed by functionalization with the DNA sequence, Seq1. 50 nm gold nanoparticles were separately functionalized with the azobenzene-modified hairpin DNA sequence (Azo-seq2) in solution and were assembled with the Seq1-functionalized 100 nm AuNPs on the glass substrate through hybridization between the two DNA sequences.

1. **Seq1 functionalization of 100 nm AuNP on ITO substrate**

ITO glass substrates were cleaned by sonicating in ethanol, dried with nitrogen stream, and plasma treated with oxygen for 5 minutes. They were immersed in a 1% ethanolic solution (by volume) of (3-Aminopropyl)triethoxysilane (3-APTES) for an hour to silanize. To remove the excess amount of silane, the ITOs were thoroughly rinsed with ethanol and sonicated in ethanol for three minutes, three times. The silanized ITOs were then annealed at 95°C for at least 2 hours under a continuous nitrogen flow. 60 μL of colloidal 100 nm AuNP solution was dropped onto the silanized substrate and left for 5 minutes, rinsed by water and dried with nitrogen. The ITO substrates were then plasma treated in oxygen for about 1 minute. Next, the 100 nm AuNPs were functionalized with Seq1 DNA. 35 μL of 0.01 M phosphate buffered saline (PBS) containing 1 M NaCl and 0.1% of sodium dodecyl sulfate (SDS) was placed on the substrate, followed by addition of 25 μL of 6 μM Seq1 solution in the same buffer. The nanoparticles were incubated in the DNA

solution for about an hour. The ITO substrate was then rinsed with 0.01 M solution of PBS containing 0.05% of SDS, then with 0.3 M solution of ammonium acetate and dried in nitrogen stream.

2. Functionalization of 50 nm AuNP in solution with azobenzene-modified DNA[63]

300 µL of 50 nm colloidal gold nanoparticle solution was added to 10 µL solution of Azo-seq2 hairpin DNA (OD = 0.7 at 260 nm after dithiol bond cleavage by DTT), sonicated, vortexed and was incubated overnight on a thermomixer set at 25˚C and 700 rpm as stirrer speed. The solution was adjusted to a concentration of 0.01 M of phosphate buffered saline and 0.01% of SDS using stock solutions of 0.1 M PBS and 1% SDS, respectively. The NaCl concentration was gradually brought up to 0.3 M, at an increment of 0.05 M, by step wise addition of 2 M NaCl stock solution, while maintaining the same concentration of PBS and SDS in the solution. The solution was sonicated, vortexed well and allowed to equilibrate for 15-20 minutes after each addition of the NaCl solution and finally incubated overnight on the thermomixer at 25˚C and 700 rpm stirring speed. The DNA-functionalized nanoparticles were then separated from the excess DNA and washed by centrifuging them down at 14500 rpm for 20 minutes, followed by redispersing in 300 µL of 0.01% SDS solution. After three successive washes, the particles were resuspended in 300 µL solution of 0.01 M PBS containing 0.3 M NaCl, 0.01% SDS and 0.02% sodium azide solution and stored at 4˚C in the dark.

3. Assembly of the 100 nm/50 nm AuNP dimer through DNA hybridization.

35 µL of 0.01 M PBS solution containing 0.3 M NaCl and 0.01% SDS was added on the Seq1-functionalized 100 nm AuNP attached to the silanized ITO, followed by addition of 25 µL of Azo-seq2 functionalized 50 nm AuNP in it. The solution was left to stand for 5 minutes to allow DNA

hybridization. The substrate was then rinsed with 0.01 M solution of PBS containing 0.05% of SDS, and by 0.3 M ammonium acetate solution and dried with nitrogen stream.

Identification and characterization of the dimer particles

Dark field microscopy and spectroscopy was performed to analyze the samples before and after dimer formation using a Nikon inverted microscope (Eclipse TE2000-U) fitted with a transmitted dark field condenser (T-CHA, Dry, NA 0.95-0.80). An objective lens of 50X (Nikon Plan RT, NA 0.7, CC 0-1.2) with an intermediate lens magnification of 1.5X was used to obtain a total magnification 75X. A standard tungsten halogen lamp was used as the transmission light source for dark field illumination. The dark field optical images were captured by thermoelectrically cooled colored CCD camera (Diagnostics Instruments, FX 1520, Software SpotView) coupled with the microscope. The single particle scattering spectra were collected through Ocean Optics fiber cable (diameter = 100 μm, UV-VIS-NIR transmission) coupled to a CCD spectrometer (USB 2000). The single particle scattering spectra of each dimer were obtained by averaging the signal over 50 scans with integration time of 500 ms per scan. The sample stage was controlled using a digital piezo controller (Physik Instrumente E-710).

The dimers were distinguished from any larger gold nanoparticle assemblies by collecting dark field images and scattering spectra at different polarization angle of the scattered light using a linear polarizer fitted into a home-made rotating stage. Correlated scanning electron microscopy (SEM) was performed on the samples by using Dual-Beam-SEM-FIB--FEI-XL830 at an accelerating voltage of 15.0 kV (Molecular Analysis Facility, University of Washington), after all the experiments were done with the sample.

Photo-triggered actuation of the dimer

The dimers were incubated in 0.01 M solution of PBS containing 0.1 M NaCl in a SecureSeal adhesive hybridization chamber (# 621101, SA8R-1.0- 8-9mm Diameter X 1.0 mm Depth, 26 mm X 51 mm OD, 1.5 mm Diameter Ports, Grace Bio-Labs) at room temperature for at least three hours prior to photoswitching experiments. To achieve the *trans*-to-*cis* photoisomerization of azobenzene-modified DNA, the dimers were illuminated with a collimated 365 nm UV LED (M365L2-C5, total beam power 80 mW, 700 mA, Thorlabs) hooked up to the inverted microscope, for 30 minutes. The irradiation intensity of the LED on the sample was measured to be 0.46 mW/cm^2, using a calibrated silicon photodiode. We kept the UV light source on in between collecting two consecutive dimer spectra, and put a shutter in front of it to block the illumination while measuring the scattering spectra. The *cis*-azobenzenes were converted back to the *trans* form by irradiating the sample with a 470 nm blue LED (M470L3-C5, total beam power 300 mW, 1600 mA, Thorlabs) at an intensity of 0.64 mW/cm^2 for 30 minutes. In this way, the *trans*-to-*cis* azobenzene photoswitching cycle was repeated three times and single particle scattering spectra for the same set of dimers were measured after each photoisomerization process in every cycle.

Data analysis

The individual dimer scattering spectra were corrected by subtracting the dark spectra (background noise from the buffer solution on silanized ITO and stray light) and dividing by the reference spectrum of the tungsten-halogen light source. The normalized scattering efficiency of each dimer was plotted as a function of wavelength and was fitted with the Lorentzian function near the region of peak of interest, using the Igor Pro 6.36, to obtain the peak position of the plasmon resonances. The reported errors in the peak positions are the standard error of mean.

Supplementary Figures and Text

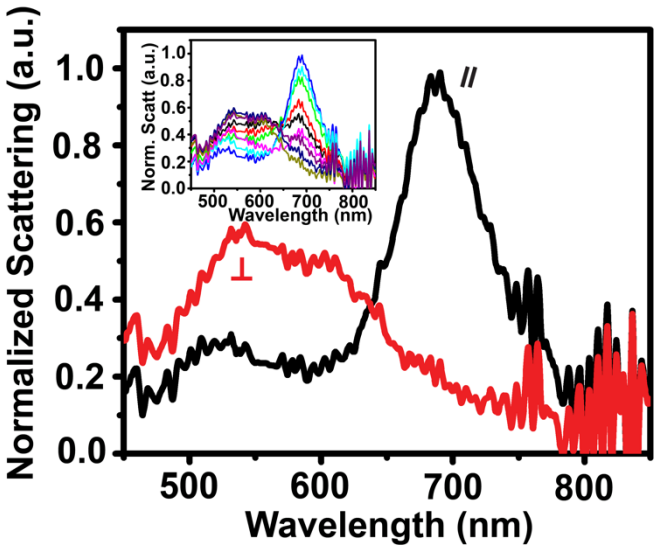

Figure S1. Polarized dark field scattering spectra of an azobenzene-modified hairpin DNA-linked 100 nm/50 nm AuNP dimer in air. Under parallel polarization, the dimer exhibits both longitudinal and transverse resonance peaks at 680 nm and 540 nm, respectively (black trace), whereas it exhibits only the high energy transverse resonance peak around 540 nm under perpendicular polarization (red curve). The inset represents scattering spectra of the dimer under various polarization angle, which exhibit both the peaks with different intensity ratios.

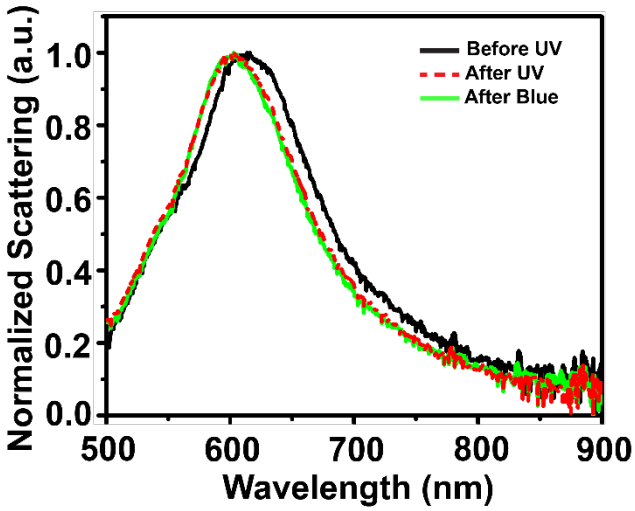

Figure S2. Dark field scattering spectra of a 100 nm/50 nm AuNP dimer linked with azobenzene-modified hairpin DNA in buffer solution, that exhibits an irreversible blue shift of the bonding

plasmon resonance peak upon UV illumination, indicating an extension of the dimer when *trans*-azobenzene converts into the *cis* configuration. No red shift of the resonance peak was observed following the blue light irradiation, suggesting that *cis*-to-*trans* reverse photoisomerization is unable to restore the closed state of the dimer.

Reversible spectral shift of plasmon resonance peak occurs due to reconfiguration of dimer structure on azobenzene photoisomerization and *not* due to DNA release on photothermal heating of nanoparticles

We note that previous studies have reported light-induced release of DNA from the surface of the nanoparticles due to their photothermal heating effect of under laser illumination.[1-3] Thus, one might argue that the release of the DNA strands from the nanoparticle dimers could lead to a decrease in the local refractive index near the nanoparticle surface that results in the observed blue shift of the bonding plasmon resonance peak of the scattering spectra in our experiments (Figure 3 (a) in main text). To confirm that the plasmonic shift in the scattering spectra occurs only due to a structural reconfiguration of the dimer on *trans*-to-*cis* photoisomerization of azobenzene molecules in the hairpin DNA, we used the same hairpin DNA sequence but without any azobenzene molecules embedded in it to fabricate the dimers, and exposed them to UV and blue LEDs under the same experimental conditions and set up. Figure S3 shows no light-induced change in the single particle scattering spectra of the non-azobenzene hairpin DNA-linked dimer after light illumination, which proves that the reversible spectral shift in the plasmon resonance peak of the azobenzene-modified hairpin-linked dimer occurs only due to its photo-triggered actuation on reversible isomerization of the azobenzene between its *trans* and *cis* conformation and *not* due to photoheating effect of AuNPs.

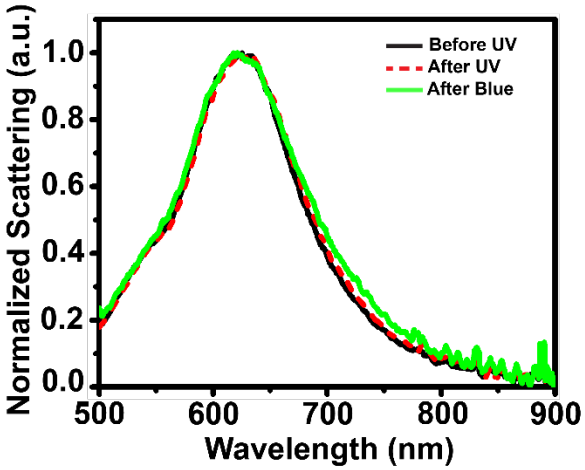

Figure S3. Dark field scattering spectra of an *unmodified* hairpin DNA-linked 100 nm/50 nm AuNP dimer in buffer solution. The plasmon resonance peak shows no change in position after UV and blue light illumination, which indicates that for the azobenzene-modified hairpin-linked dimers, the spectral shift arises only due to the reversible *trans*-to-*cis* photoswitching of azobenzenes.

We also calculate the increase in the temperature on the nanoparticle surface under UV and blue light illumination using the following equation:[4]

$$\Delta T = \frac{\sigma_{abs} I}{4\pi R_{eq} \beta \kappa_{water}} \qquad (S1)$$

σ_{abs} is the absorption cross section (m^2) of the nanoparticle, I is the irradiation intensity (W/m^2), R_{eq} is the radius of the spherical nanoparticle (m), β is thermal capacitance coefficient, which is equal to 1 for spherical gold nanoparticles, and κ_{water} is the thermal conductivity of water (0.6 W/m·K). For 100 nm and 50 nm gold nanoparticles we obtain $\sigma_{abs,100\ nm\ AuNP} \sim 1.8\times10^{-14}$ m^2 and $\sigma_{abs,50\ nm\ AuNP} \sim 6.5\times10^{-15}$ m^2.[5] So under UV irradiation (intensity 4.6 W/m^2), the change in temperature is estimated to be $\sim2.2\times10^{-7}$ K and $\sim1.6\times10^{-7}$ K for the 100 nm and 50 nm AuNP, respectively and upon blue light exposure (intensity 6.4 W/m^2) the calculated changes are

$\Delta T_{100\ nm\ AuNP} = 3.1\times10^{-7}$ K, and $\Delta T_{50\ nm\ AuNP} = 2.2\times10^{-7}$ K. This insignificant rise in temperature of the nanoparticle surface upon light illumination stands in contrast to the argument that release of DNA strands from the nanoparticle surface by photothermal heating causes the plasmonic shift in the scattering spectra of the dimer and hence supports the azobenzene photoisomerization induced dimer reconfiguration.

Plasmon ruler equation to measure interparticle distances

The shift in the bonding plasmon resonance peak in the individual dimer scattering spectra is measured for each *trans*-to-*cis* reversible photoisomerization cycle of azobenzene and the corresponding interparticle separation between the 100 nm and 50 nm gold nanoparticles on photo-triggered actuation of the dimer is calculated by using the plasmon ruler equation reported in literature.[6] For a symmetric pair of spherical gold nanoparticles in biological systems

$$\frac{\Delta\lambda}{\lambda_0} \approx 0.18 * \exp\left(-\frac{\left(\frac{x}{D}\right)}{0.23}\right) \qquad (S2)$$

where $\frac{\Delta\lambda}{\lambda_0}$ is the fractional shift of the plasmon resonance peak and x is the interparticle edge-to-edge distance. For the asymmetric 100 nm/50 nm AuNP dimers in our case, we used the average particle diameter as D = 75 nm and obtained an interparticle distance change of 3.4 nm between the closed and the open configuration of the dimer on azobenzene photoswitching. The value lies in between the lowest limit of 1.1 nm for a symmetric 50 nm AuNP dimer and the highest limit of 4.6 nm for a pair of 100 nm AuNPs.

Finite-Difference Time-Domain simulation

FDTD simulations were performed on a 100 nm/50 nm gold nanoparticle dimer with varying distances between the two nanoparticles using the FDTD package in Lumerical Solutions,

Inc (version 8.18) to simulate the dimer scattering spectra and correlate to our experimental observations obtained by dark field spectroscopic measurements and also to the interparticle distances predicted from the plamson ruler equation. A simulation box with 1.25 nm mesh was used for all the calculations to ensure convergence. The permittivity of both 50 nm and 100 nm gold nanoparticles were modelled after the dielectric function provided by Johnson and Christy,[7] while the DNA layers on both the gold nanoparticles were modeled as thin dielectric shells with refractive index of $n_{ssDNA} = 1.7$. A broadband total-field scattered-field (TFSF) source was chosen for the simulations, primarily to compute the scattering of the nanoparticles. Two perfectly matched layers (PML) were used as absorbing materials, arranged inside and outside the source to determine the absorption and scattering coefficients, respectively. The ITO substrate was modelled as a rectangular material of refractive index obtained from literature[8] and the dielectric constant of the medium in the simulation box was set as 1.33 for buffer solution. In all the simulations, the 100 nm AuNP was held fixed on the ITO surface and the position of the 50 nm AuNP was moved inside the simulation box to vary the edge-to-edge separation between the two nanoparticles. To probe both longitudinal and transverse plasmon coupling modes between the two nanoparticles, two sets of incident plane waves (both normal to the surface) were used, one parallel and one perpendicular to the dimer axis.

The simulated spectra for a dimer with interparticle edge-to-edge separation as 14 nm (black curve) and 18 nm (red curve) match very closely to the dark field scattering spectra of the closed and open state of an average dimer particle, respectively, as shown in Figure S4. Thus, the change in interparticle distance by 4 nm, obtained from the FDTD simulations, agrees well with the results calculated from the plasmon ruler equation on reversible photoreconfiguration of the dimer.

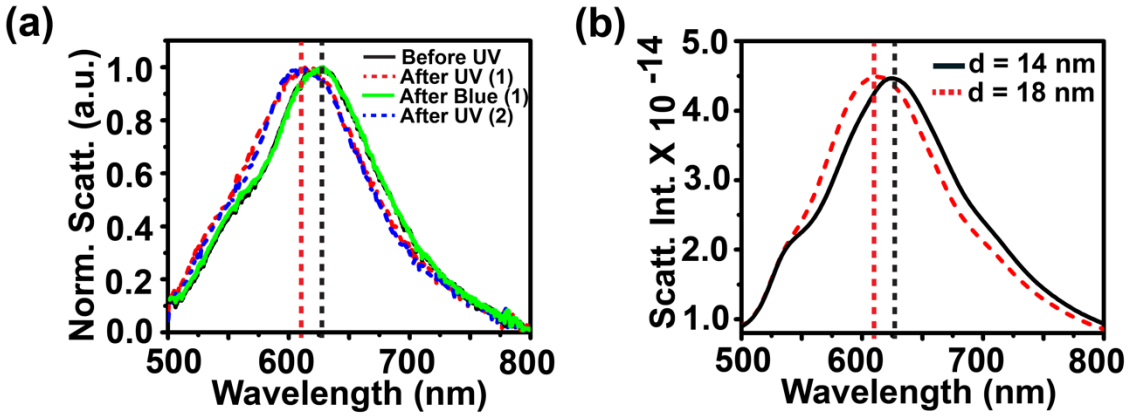

Figure S4. (a) Dark field scattering spectra of an average 100 nm/50 nm AuNP dimer before and after azobenzene photoswitching, showing a reversible shift in the bonding plasmon resonance peak by ~8.3 nm. The spectral shift corresponds to a change in the interparticle separation by 3.4 nm between the closed and open state of the dimers. (b) FDTD simulated scattering spectra of a 100 nm/50 nm AuNP dimer with edge-to-edge interparticle distances d = 14 nm (black curve) and 18 nm (red curve), which closely resemble with the experimental scattering spectra for the closed (black and green solid traces in (a)) and open state (red and blue dashed traces in (a)) of the dimer, respectively, and thus, give a change in the interparticle separation of 4 nm between the two configurations of the dimer structure, consistent with the values obtained from plasmon ruler equation.

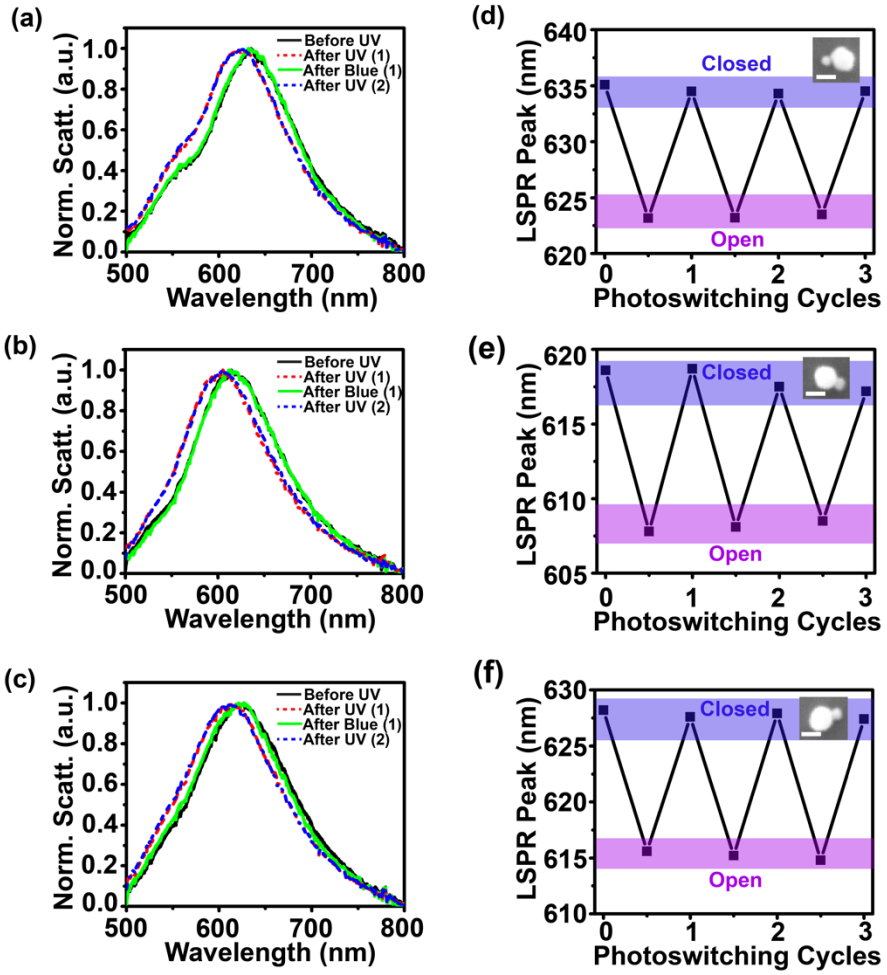

Figure S5. (a-c) Single particle dark field scattering spectra of three different representative dimers in buffer solution before and after multiple photoswitching cycles. (d-f) Reversible change in the scattering spectral peak position of the corresponding dimers in (a-c) as the hairpin DNA unzips and reforms during reversible azobenzene photoisomerization under UV and blue light illumination. This indicates the reversibility of photo-induced reconfiguration of the azobenzene-modified hairpin DNA-linked AuNP dimers. Insets in (d-f) represent the correlated SEM images of the respective dimers. Scale bar = 100 nm.

Supplementary References

(1) Link, S.; El-Sayed, M. A. Shape and size dependence of radiative, non-radiative and photothermal properties of gold nanocrystals. *Int. Rev. Phys. Chem.* **2000**, *19*, 409-453.

(2) Richardson, H. H.; Carlson, M. T.; Tandler, P. J.; Hernandez, P.; Govorov, A. O. Experimental and Theoretical Studies of Light-to-Heat Conversion and Collective Heating Effects in Metal Nanoparticle Solutions. *Nano Lett.* **2009**, *9*, 1139-1146.

(3) Huschka, R.; Zuloaga, J.; Knight, M. W.; Brown, L. V.; Nordlander, P.; Halas, N. J. Light-Induced Release of DNA from Gold Nanoparticles: Nanoshells and Nanorods. *J. Am. Chem. Soc.* **2011**, *133*, 12247-12255.

(4) Baffou, G.; Quidant, R.; de Abajo, F. J. G. Nanoscale Control of Optical Heating in Complex Plasmonic Systems. *ACS Nano* **2010**, *4*, 709-716.

(5) Jain, P. K.; Lee, K. S.; El-Sayed, I. H.; El-Sayed, M. A. Calculated absorption and scattering properties of gold nanoparticles of different size, shape, and composition: Applications in biological imaging and biomedicine. *J. Phys. Chem. B* **2006**, *110*, 7238-7248.

(6) Jain, P. K.; Huang, W. Y.; El-Sayed, M. A. On the universal scaling behavior of the distance decay of plasmon coupling in metal nanoparticle pairs: A plasmon ruler equation. *Nano Lett.* **2007**, *7*, 2080-2088.

(7) Johnson, P. B.; Christy, R. W. Optical Constants of The Noble Metals. *Phys. Rev. B* **1972**, *6*, 4370-4379.

(8) Konig, T. A. F.; Ledin, P. A.; Kerszulis, J.; Mahmoud, M. A.; El-Sayed, M. A.; Reynolds, J. R.; Tsukruk, V. V. Electrically Tunable Plasmonic Behavior of Nanocube-Polymer Nanomaterials Induced by a Redox-Active Electrochromic Polymer. *ACS Nano* **2014**, *8*, 6182-6192.

APPENDIX C

Supporting Information for Chapter 5

Experimental Methods

Materials

N-Isopropylacrylamide (NIPAM, ≥ 99 %), allylamine (≥ 99 %), N,N′-methylene bis(acrylamide) (≥ 99.5 %), potassium persulfate (≥ 99 %), silver nitrate (≥ 99.99 %), sodium borohydride ($NaBH_4$, ≥ 99.99 %), bis(p-sulfonatophenyl)phenylphosphine dihydrate dipotassium salt (BSPP, 97%), and sodium citrate tribasic dihydrate (≥ 99.5 %) were purchased from Sigma Aldrich. Hydrogen peroxide (30 %, ACS reagent) was obtained from J. T. Baker Chemical Co.. All water used in the experiments were deionized to 18.2 MΩ.

Synthesis of PNIPAM Microgels

PNIPAM microgels were synthesized by free-radical polymerization using N-isopropylacrylamide (NIPAM) and allylamine as monomers and N,N′-methylenebis(acrylamide) (BIS) as the crosslinking agent in presence of potassium persulfate as the initiator.[33,34] Briefly, 50 mL of aqueous solution containing 0.25 g of NIPAM and 0.01 g of N,N′-methylenebis(acrylamide) (BIS) was heated up to 80 °C while purging with N_2 gas for 30 minutes in a 100 mL three-neck flask. This was followed by sequential injection of 70 μL allylamine and 250 μL aqueous solution of potassium persulfate (0.025 g/mL). The reaction was continued for 2 hours under constant stirring at 800 rpm at 80 °C under N_2 protection. The PNIPAM product was washed by centrifuging the reaction solution at 8000 rpm for 30 minutes and redispersing the precipitate into Millipore water. After repeating the same washing procedure for two additional times, the final product was dissolved in a total volume of 40 mL of Millipore water and stored at 4 °C for future use. The as-synthesized PNIPAM microgels have hydrodynamic diameters ranging from 498 nm to 531 nm with a mean of 517.5 ± 6.5 nm, and exhibit a deswelling ratio of 0.04 with a lower critical solution temperature (LCST) at 39 °C (see Figure S1).

Synthesis of the Silver Nanoprisms

We synthesized two different sizes of silver nanoprisms using either of two slightly different photochemical methods as described below.

1. Ag nanoprism Method 1: In this route, Ag nanoprisms were prepared by a photomediated reduction of silver nitrate ($AgNO_3$) based on the published methods[60,61] with some modifications. Briefly, an aqueous solution of silver nitrate (0.2 mM, 25 mL), sodium citrate (100 mM, 500 μL), hydrogen peroxide (30 wt. %, 60 μL) were mixed thoroughly under magnetic stirring at room temperature. Then, 180 μL of freshly prepared 100 mM $NaBH_4$ solution was rapidly injected to the above mixture. The color of the mixture immediately changed from colorless to pale yellow, and then to wine-red. After that, the solution was illuminated with a 460 nm LED (LED Engin, Inc.) for 72 hours, at which point the solution was yellow-brown in color. The as-synthesized Ag nanoprisms were washed and purified by centrifugation and redispersed in 5 mM sodium citrate solution. The same purification step was repeated three times after which the nanoprisms were stored in 5 mM sodium citrate solution at 4 °C for future use. The average edge length of the nanoprisms were typically ~ 30 ± 5 nm with a thickness of roughly 8 ± 2 nm, as obtained from the scanning electron microscope images. The final plasmon resonance peak of the silver nanoprisms were in the range of 474 - 480 nm (see Figure S2).

2. Ag nanoprism Method 2:[62,63] 2 mL of 5 mM $AgNO_3$ solution and 1 mL of 30 mM sodium citrate solution were added to 95 mL water in a 250 mL round bottom flask placed in ice. The mixture was purged with nitrogen and stirred with a magnetic stirrer for an hour. Then, 1.4 mL of freshly prepared ice-cold 50 mM $NaBH_4$ solution was added in a stepwise manner to yield a pale-yellow solution, indicating the formation of spherical silver nanoparticles. A few minutes later, a mixture containing 1 mL of 5 mM bis(p-sulfonatophenyl)phenylphosphine dihydrate dipotassium (BSPP) and 500 μL of the 50 mM $NaBH_4$ solution was gradually injected into the solution. After aging this precursor solution in the dark for 15 hours, pH of the solution was adjusted to 11.0 and the spherical silver particles were then photochemically converted into flat prisms by exposing the solution to a 590 nm LED (LED

Engin, Inc.) for 24 hours. The resulting nanoprisms had an average edge length of 55 ± 14 nm, thickness of 10 ± 2 nm and exhibit an LSPR peak near 570 nm (see Figure S2).

Fabrication of PNIPAM/Ag nanoprism Hybrids

To demonstrate the variety of colors accessible in the initial and final states of these thermochromic nanocomposites, we prepared PNIPAM/Ag nanoprism hybrid microgel composites by mixing the different types of as-synthesized Ag nanoprisms with the PNIPAM solution in equal volumes.

To study the effect of the nanoprism loading on the thermoresponsivity of the optical properties, five different hybrid microgels were prepared, each by taking 600 μL solution of Ag nanoprisms (Method 1) and adding different amounts of the PNIPAM solution, 600 μL, 300 μL, 150 μL, 75 μL and 37.5 μL (i.e. in volume ratios ($V_{Ag\ nanoprism}/V_{PNIPAM}$) of 1:1, 2:1, 4:1, 8:1 and 16:1, respectively), to achieve increasing nanoprism loadings. All the hybrid solutions were allowed to equilibrate for 30 minutes at room temperature before any optical measurements and structural characterization.

Material Characterization

1. Scanning Electron Microscopy: Typically, ~ 30-50 μL of the hybrid solutions were deposited on a clean ITO slide, left for ~ 5-10 minutes and blown dry with a nitrogen stream. SEM images of the samples were collected with a FEI Sirion XL30 SEM at a 5 kV accelerating voltage to verify the formation of the PNIPAM/Ag nanoprism hybrids with varying loading densities.

2. UV-Vis spectroscopy: Temperature-dependent change in the optical properties of the hybrids were measured using an Agilent 8453 UV-Vis spectroscopic system coupled to a Peltier temperature controller. Using thermal denaturation mode in the instrument, the hybrid solutions were heated from 25 °C to 50 °C, at a step size of 1 °C with equilibration time of 2 minutes at each step and extinction spectra were collected at each temperature. For thermal switching experiments, the temperature of the hybrid solutions was cycled between 25 °C and 50 °C and the extinction spectra were obtained after equilibrating the solution for 5 mins in each heating and cooling step during the process. All the extinction spectra were plotted using OriginPro 9.

3. Dynamic light scattering (DLS) measurements: The temperature-dependent changes in the hydrodynamic diameter of the PNIPAM microspheres and the PNIPAM/Ag nanoprism hybrids were measured using a Malvern Zetasizer with a 633 nm laser. The average hydrodynamic diameter was obtained from 20 scans at 10 seconds/scan rate.

4. NIR scattering images: The hybrid solutions with different nanoprism loading densities were heated on a calibrated hot plate from 25 °C to 50 °C and illuminated by an 808 nm laser diode (5 mW output power). NIR scattering images and videos were recorded using a CCD camera (Monoprice Inc.) with an exposure time of 0.5 ms (see Figure S8 for experimental set up). The NIR scattering intensities of the hybrids at different temperatures were calculated by analyzing these images using ImageJ.

Supplementary Text and Figures

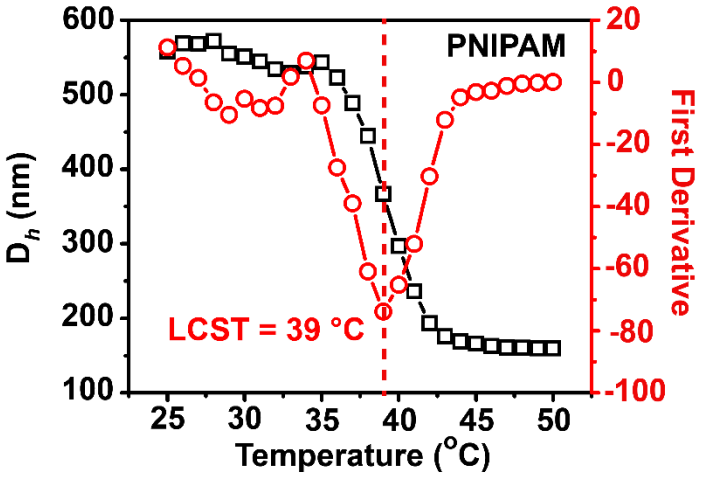

Figure S1. Change in the hydrodynamic diameter (black squares) with temperature and first derivative plot (red circles) to obtain the LCST of PNIPAM. The sample was heated from 25 °C to 50 °C at an increment of 1 °C and equilibrated for 2 minutes at each temperature. The LCST of the PNIPAM was measured to be 39 °C.

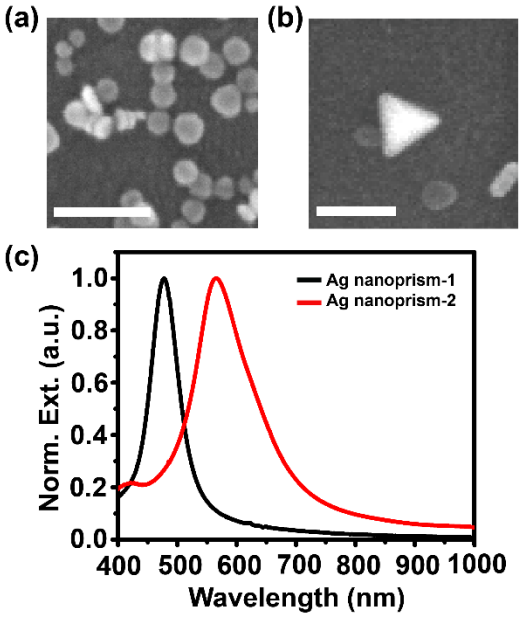

Figure S2. SEM images of (a) Ag nanoprisms-1 and (b) Ag nanoprisms-2, used to fabricate hybrid 1 and hybrid 2 (in Figure 1), respectively, with PNIPAM microgels. Scale bars in the images are 100 nm. (c) Normalized extinction spectra of the two nanoprisms at 25 °C.

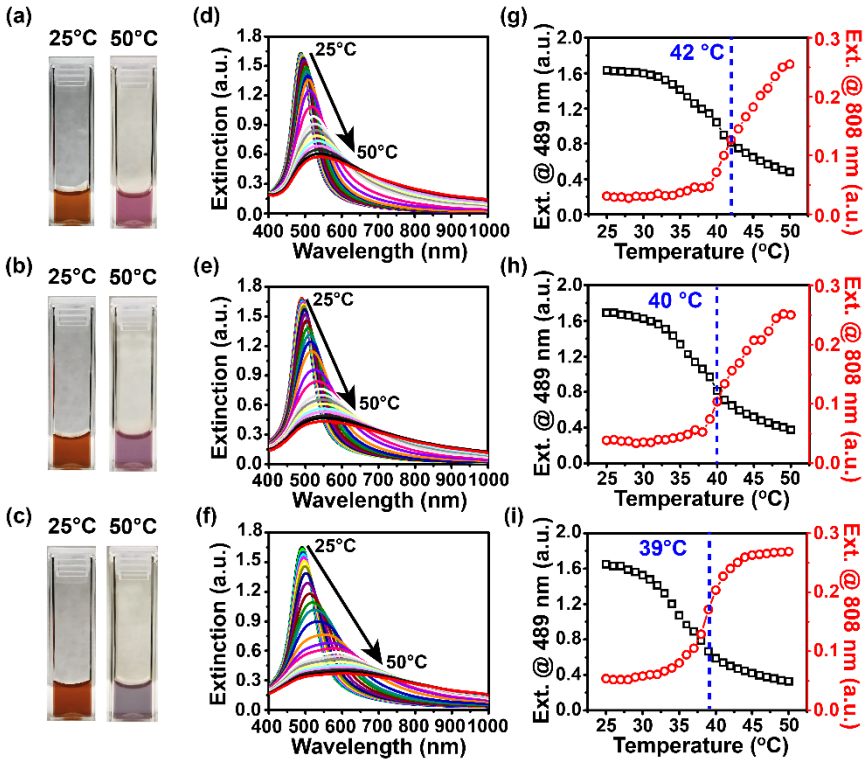

Figure S3. (a)-(c) Photographs of the PNIPAM/Ag nanoprism hybrids with intermediate nanoprism loadings at 25 °C and 50 °C showing a tunable color switching of the hybrids with nanoprism loading

density. (d)-(f) Temperature-dependent change in the extinction spectra of the hybrids, and (g)-(i) corresponding changes in the extinction at 489 nm (black squares) and 808 nm (red circles) with the rise in temperature from 25 °C to 50 °C indicating a variation of the thermal-sensitivity of the hybrids with nanoprism loading density. The blue dashed lines in (g)-(i) denote the temperature at which the maximum change in the extinction is observed. The volume ratio of the Ag nanoprism and PNIPAM solutions ($V_{Ag\ nanoprism}/V_{PNIPAM}$) in these hybrids are 2:1 in (a), (d), (g), 4:1 in (b), (e), (h) and 8:1 in (c), (f), (i).

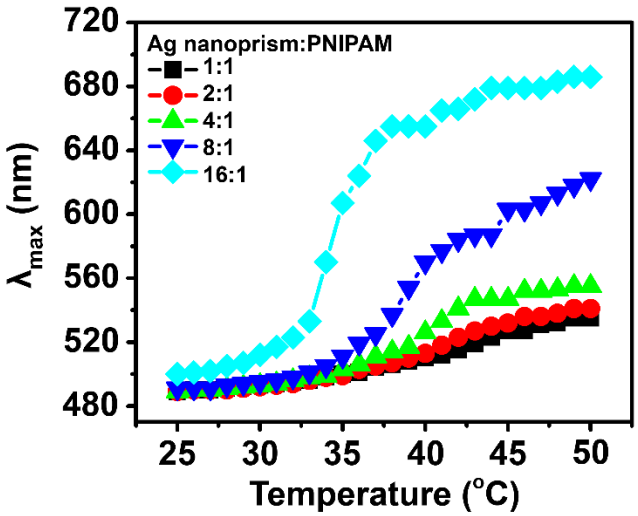

Figure S4. Temperature-dependent change in the extinction peak of the hybrids microgels with different nanoprism loading ratios, as the solution is heated from 25 °C to 50 °C. The shift in the extinction peak becomes greater with increasing nanoprism loading density.

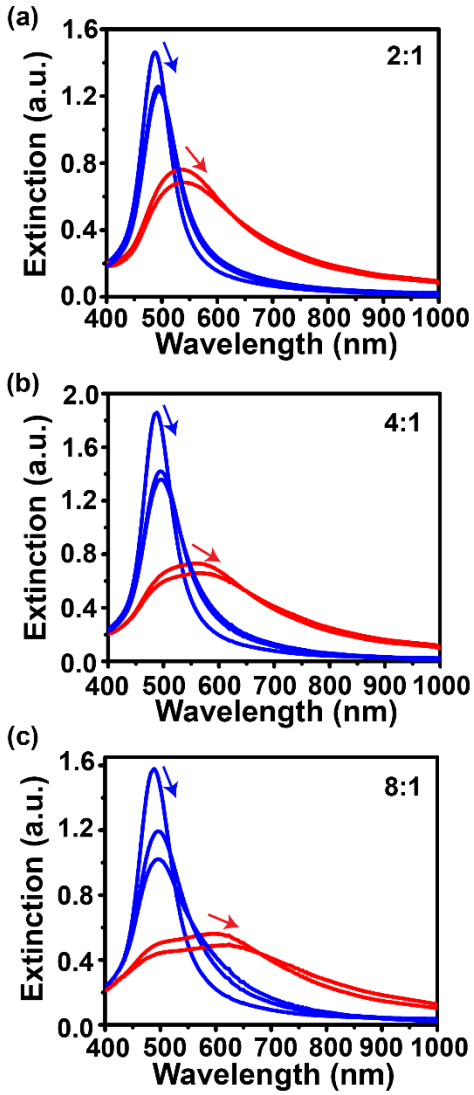

Figure S5. Change in the extinction spectra of the PNIPAM/Ag nanoprism hybrids with intermediate loading densities of nanoprisms as the temperature of the hybrid solutions is cycled between 25 °C (blue spectra) and 50 °C (red spectra). The arrows indicate increasing number of heating/cooling cycles. The volume ratio of the Ag nanoprisms and PNIPAM ($V_{Ag\ nanoprism}/V_{PNIPAM}$) in these hybrids are (a) 2:1, (b) 4:1, (c) 8:1.

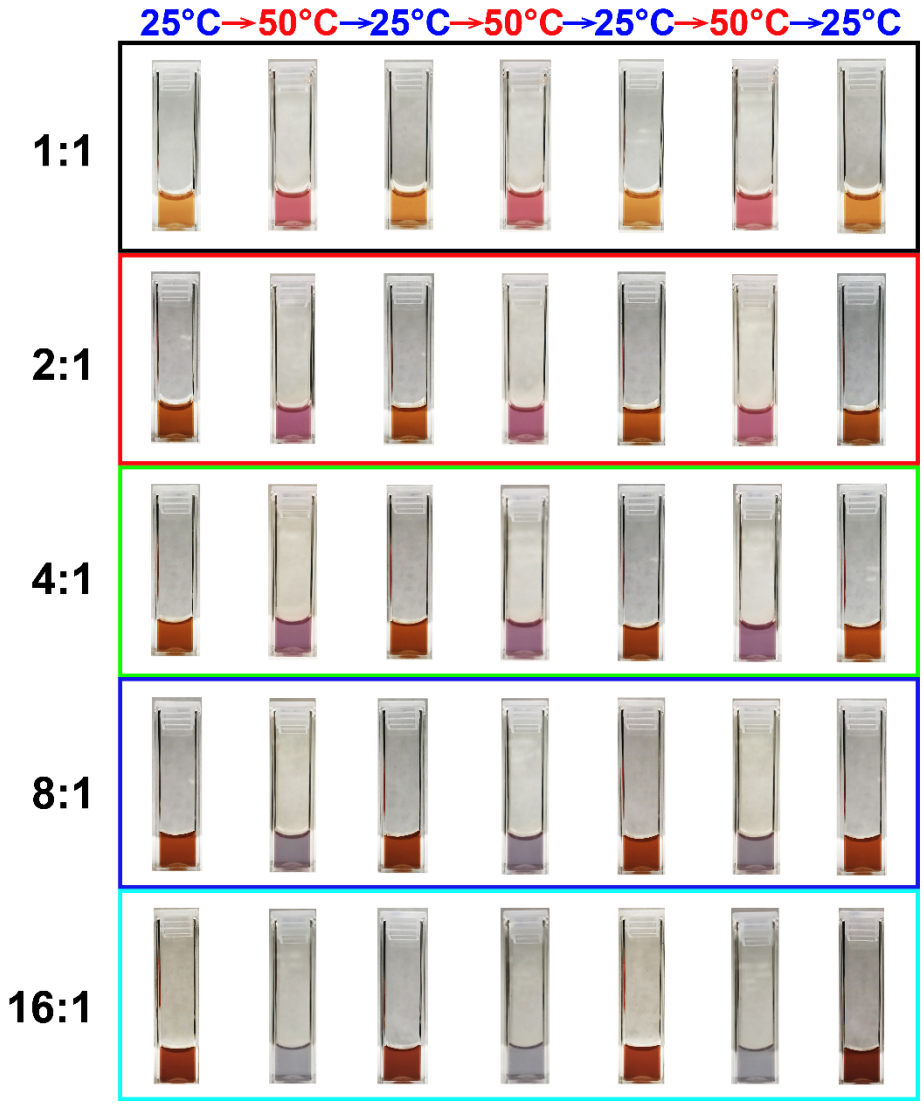

Figure S6. Thermally reversible color switching of different PNIPAM/Ag nanoprism hybrid microgels with increasing loading densities (from top to bottom). The Ag nanoprism:PNIPAM volume ratios in these hybrids are 1:1, 2:1, 4:1, 8:1 and 16:1. The photos were taken with an iPhone 7 camera.

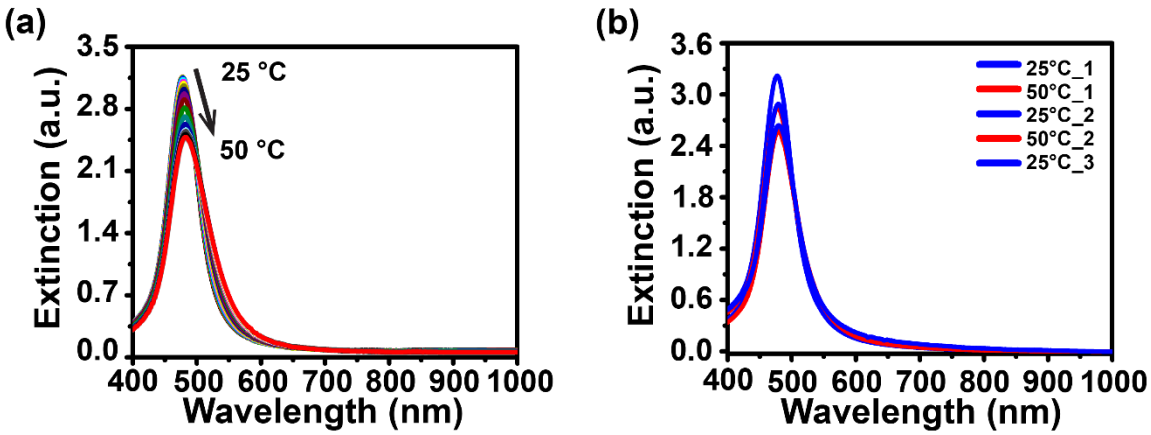

Figure S7. Change in the extinction spectra of the silver nanoprisms as (a) the temperature is increased from 25 °C to 50 °C, at an increment of 1 °C and (b) the temperature is cycled between 25 °C (blue spectra) and 50 °C (red spectra). In both cases, we see a minor change in the linewidth and a small decrease in the extinction at 478 nm, which probably implies an oxidation of the silver particles at higher temperature.

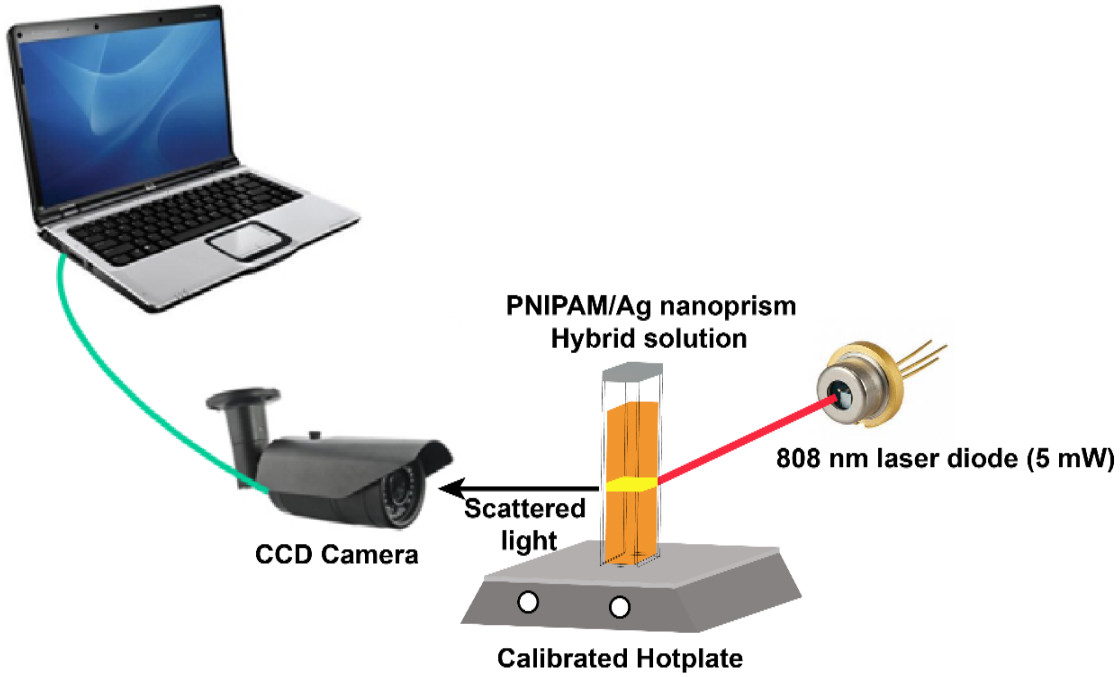

Figure S8. Instrument set-up for near-infrared scattering imaging of the hybrid solutions. The incident light source is an 808 nm (5 mW) laser diode and the detector is a CCD camera. The temperature of the solution was controlled by a calibrated hot plate. The detector was positioned to collect scattered light at a 90° angle to the incident light.

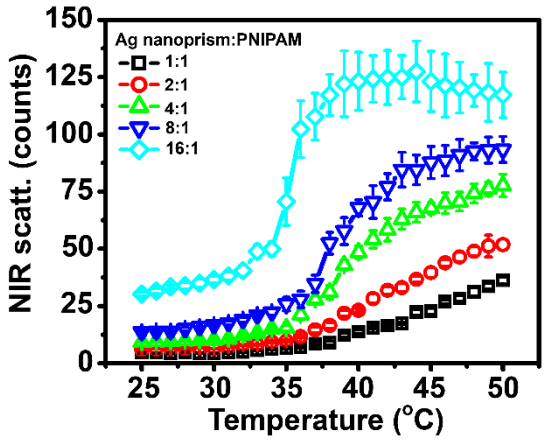

Figure S9. Temperature-dependent change in the NIR scattering of the hybrids with different Ag nanoprism loading densities (i.e. different volume ratios of Ag nanoprisms to PNIPAM as indicated in the legend).

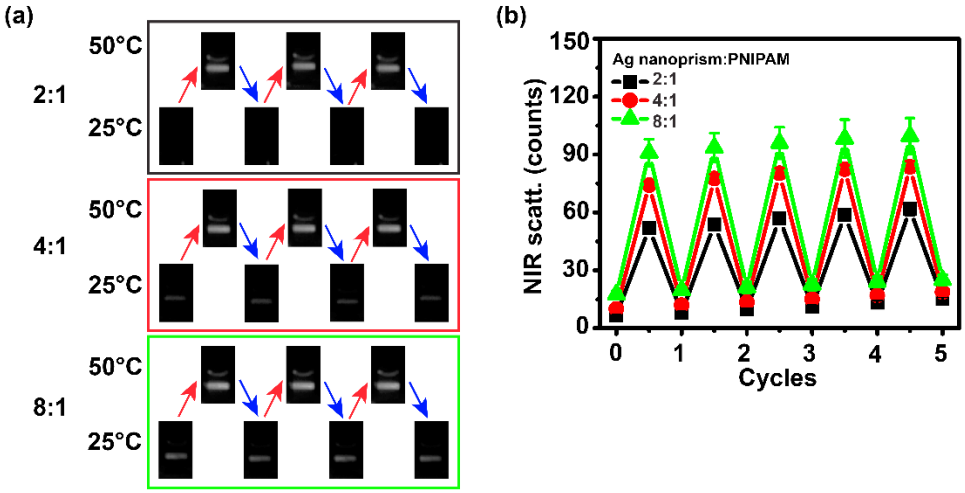

Figure S10. Thermally reversible change in (a) NIR scattering images and (b) the scattering intensities (gray counts extracted from the NIR images) of the hybrid solutions with Ag nanoprism and PNIPAM volume ratios 2:1, 4:1, 8:1 (intermediate loading densities) as we cycle the solution temperature between 25 °C and 50 °C, repeatedly.

S.1 Discussion on heat-induced aggregation of the PNIPAM/Ag nanoprism hybrid microgels

We study the variation of the heat-induced swelling-deswelling behavior of these hybrids and correlate that with their temperature-dependent optical responses. Figure S11 shows the change in the hydrodynamic diameter (D_h) of the PNIPAM/Ag nanoprism hybrid solutions as a function of temperature, measured by dynamic light scattering technique. Consistent with the previously reported results,[1,2] the hydrodynamic diameters of the nanocomposite particles are much smaller than the PNIPAM microspheres at 25 °C, as the interaction between the silver nanoparticles and PNIPAM molecules crosslinks the polymer network and alters the hydrophilicity of the polymer. Even though the pure PNIPAM microgels (Figure S1) display a sharp decrease in the hydrodynamic diameter from 522.1 ± 7.4 nm to 178.1 ± 9.2 nm beyond its LCST (39 °C), the hybrids show a temperature-induced aggregation at higher temperatures, as indicated by the sharp increase in the hydrodynamic diameter, after an initial decrease in the lower temperature range. The volume transition temperatures calculated from the change in the hydrodynamic diameter (first derivative) of the hybrids (Figure S11) are in good agreement with the optical transition temperatures measured from the change in the extinction of the solutions (blue dashed lines in Figure 2 (e) and (f) in main text and Figure S3 (g)-(i)). We predict that this temperature-induced aggregation results in a significant enhancement of the interparticle plasmonic coupling of the nanoprisms, and causes the sharp change in the extinction of these hybrids with increasing temperature.

Previous studies[3-5] have shown that aggregation of PNIPAM and PNIPAM-based nanocomposite materials occurs at higher temperature due to intermolecular hydrogen bonding and strong hydrophobic interactions between the polymers. Interestingly, our results demonstrate that the temperature-induced aggregation occurs only for the hybrid microgels, but not for pure PNIPAM microspheres. The variation in the thermal aggregation rate and the concomitant increase in the hydrodynamic size of the hybrids with the nanoprism loading ratio can be attributed to the difference in the free surface area on the microgels to form hydrophobic interactions, the availability of the intermolecular hydrogen bonding formation sites in the hybrids, or a combination of both.

In contrast to the previous aggregation studies on PNIPAM,[5-8] our work demonstrates an irreversible association of the hybrid microgels on heating. These aggregated microgels do not undergo any dissociation upon cooling down the temperature from 50 °C to 25 °C; instead, all the composite microgel particles in the cluster rehydrate and reswell, giving a larger hydrodynamic diameter at 25 °C than the initial state (Figure 3 (d) in main text). Scheme 1 illustrates the heat-induced aggregation process for the PNIPAM/Ag nanoprism hybrid microgels. The difference in the hydrodynamic diameter of the hybrids at 50 °C between Figure 3(d) and Figure S11 indicates that the aggregation process is kinetically controlled and thus, depends on the rate of heating. A slow, stepwise increment of the temperature from 25 °C to 50 °C leads to formation of larger clusters of the hybrids whereas smaller aggregates are formed during rapid heating/cooling cycles. Such kinetically controlled thermal aggregation of PNIPAM has also been reported by Ding et al[9] in their microcalorimetric studies on aggregation/dissolution of PNIPAM.

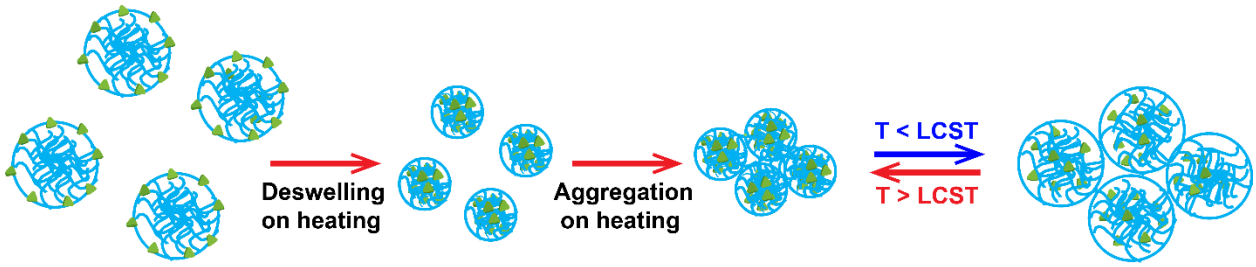

Scheme 1. Thermal aggregation of the PNIPAM/Ag nanoprism hybrid microgels showing reversible swelling-shrinking behavior.

Consistent with previous reports,[1,2,10] we observed that the swelling-deswelling of the hybrid microgels is significantly reduced compared to the pure PNIPAM microgels and deswelling ratio (ratio of the hydrodynamic volume of the collapsed state to the swollen state) of the composite materials increases (i.e. less shrinking) with higher packing density of the nanoprisms on the polymer microgels. This happens due to a strong interaction between the silver nanoprisms and the polymer that increases intrachain crosslinking of the microgel, and reduces hydrogen bonding formation with water. Thus, it alters the hydrophilic/hydrophobic interactions of the microgel in the composite materials.

Finally, we aim to investigate the origin of the irreversible aggregation of the PNIPAM/Ag nanoprism hybrid microgels at high temperatures, which has not been previously observed for similar

hybrids with gold or silver nanospheres. As the PNIPAM microgels containing silver nanospheres (60 nm, Ted Pella, Inc.) of various loading densities exhibit reversible swelling-shrinking without any aggregation during thermal switching cycles under the same experimental conditions (Figure S14), we speculate that the aggregation of the microgels in our studies might be caused by the silver nanoprisms or some undesired residual compound in the silver nanoprisms solution that irreversibly associates the hybrid microgels. However, the PNIPAM microgels do not show any the heat-induced aggregation when mixed with only the supernatant of the silver nanoprisms (Figure S14). These observations strongly suggest that it is the silver nanoprisms that are responsible for the thermal aggregation of the hybrids. We suspect that oxidation of the silver nanoprisms at higher temperature could irreversibly crosslink the PNIPAM microgels at their collapsed state.

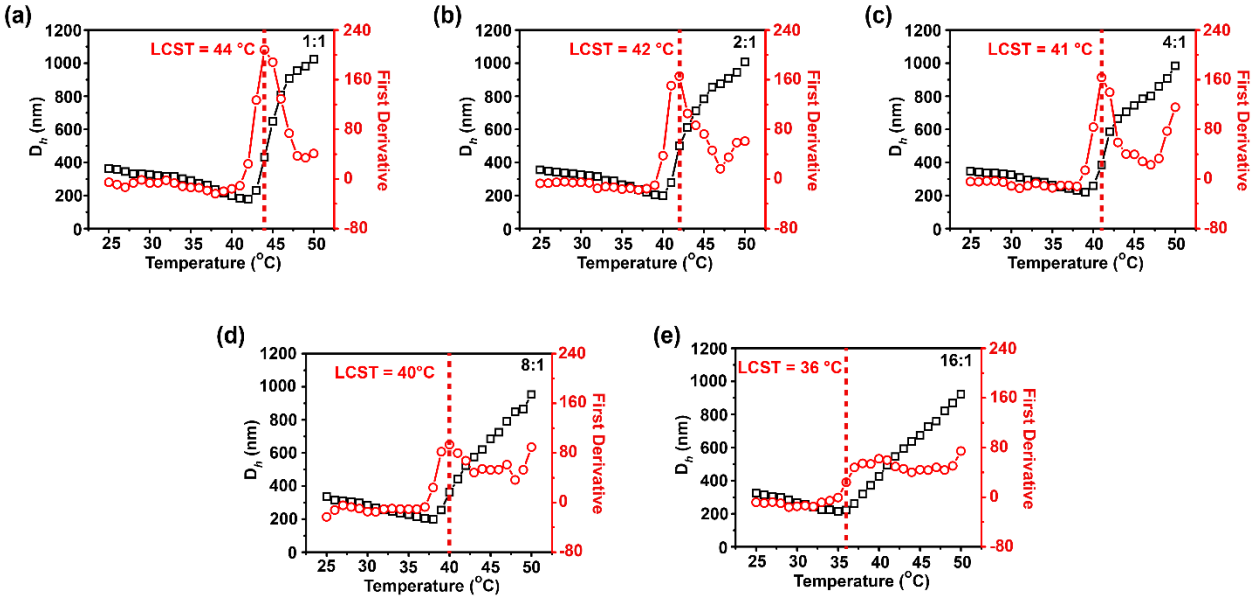

Figure S11. Change in the hydrodynamic diameter (black squares) with temperature and first derivative plot (red circles) of the PNIPAM/Ag nanoprism hybrid microgels with different nanoprism loading densities. The red dashed lines denote the temperature at which the maximum change in the hydrodynamic size is observed. These temperatures also correlate to the maximum change in the extinction of the hybrids. The volume ratios of Ag nanoprisms to PNIPAM ($V_{Ag\ nanoprism}/V_{PNIPAM}$) in these samples are (a) 1:1, (b) 2:1, (c) 4:1, (d) 8:1, (e) 16:1. The samples were heated from 25 °C to 50 °C at an increment of 1 °C and equilibrated for 2 minutes before taking the measurement.

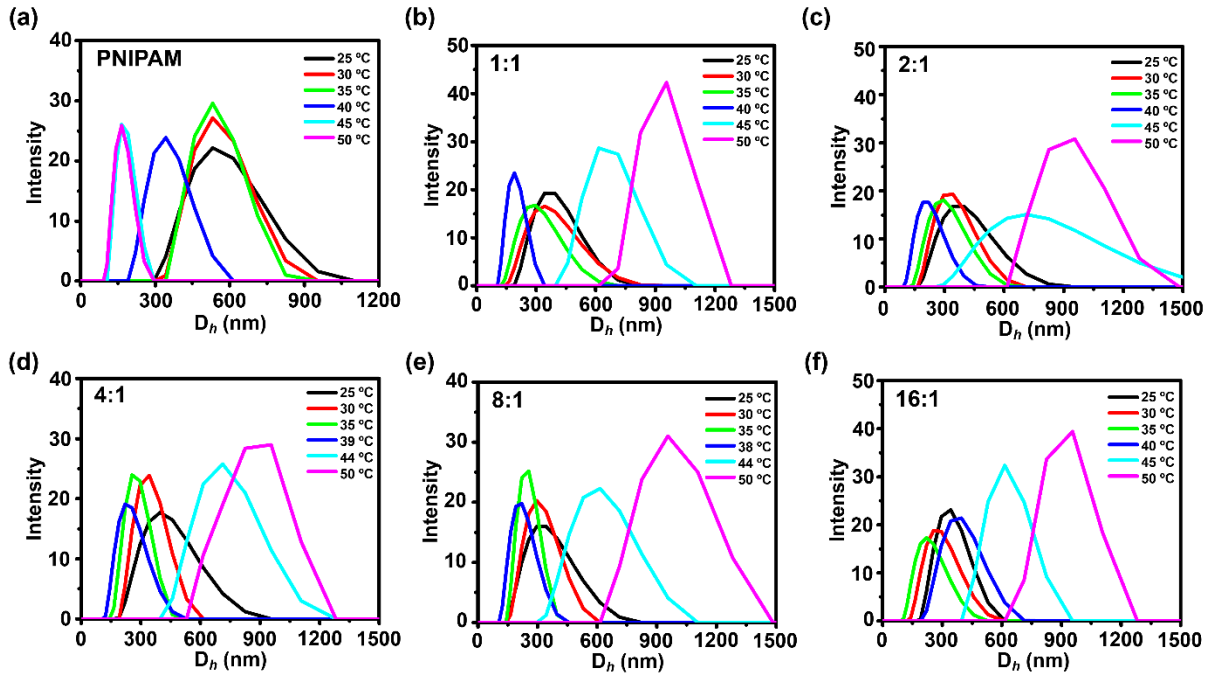

Figure S12. Intensity versus hydrodynamic diameter (D_h) distribution of (a) PNIPAM and (b)-(f) the PNIPAM/Ag nanoprism hybrids with different loadings as the solution is heated from 25 °C to 50 °C. The ratio of the volume of Ag nanoprism and PNIPAM solutions ($V_{Ag\ nanoprism}/V_{PNIPAM}$) used to prepare the hybrids are (b) 1:1, (c) 2:1, (d) 4:1, (e) 8:1, (f) 16:1.

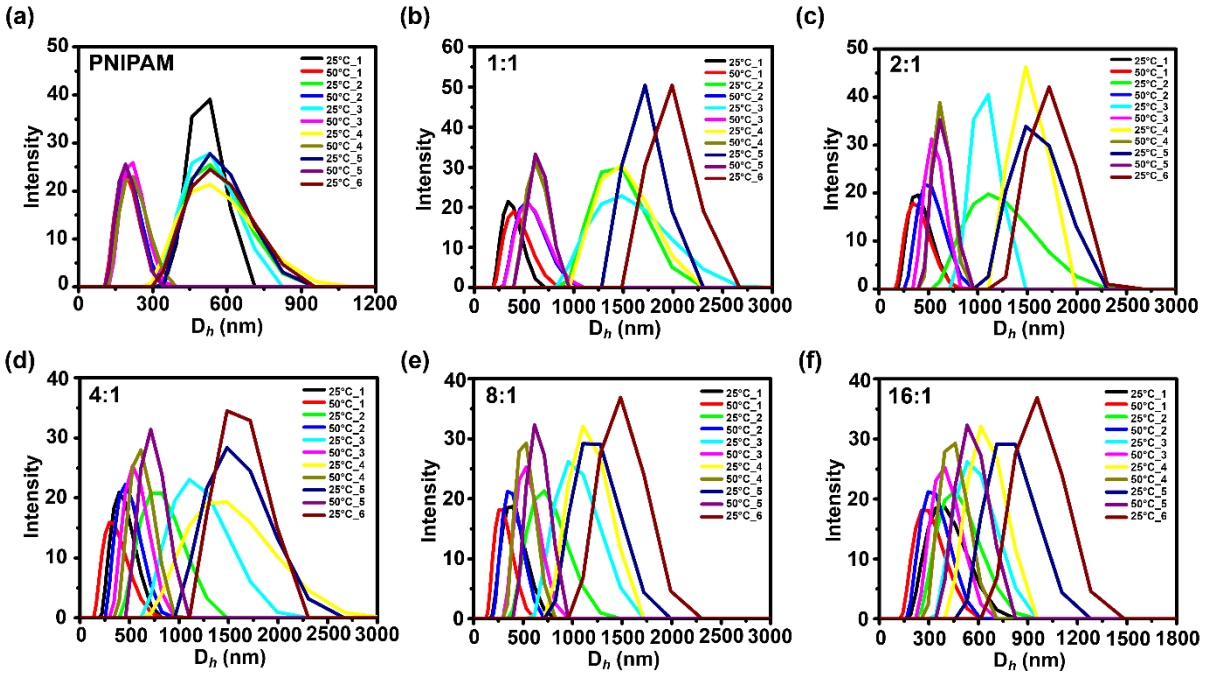

Figure S13. Intensity versus hydrodynamic diameter (D_h) distribution of (a) PNIPAM and (b)-(f) the PNIPAM/Ag nanoprism hybrids with different loadings, as we cycle the solution temperature between 25 °C and 50 °C, repetitively. The ratio of the volume of Ag nanoprism and PNIPAM solutions ($V_{Ag\ nanoprism}/V_{PNIPAM}$) used to prepare the hybrids are (b) 1:1, (c) 2:1, (d) 4:1, (e) 8:1, (f) 16:1.

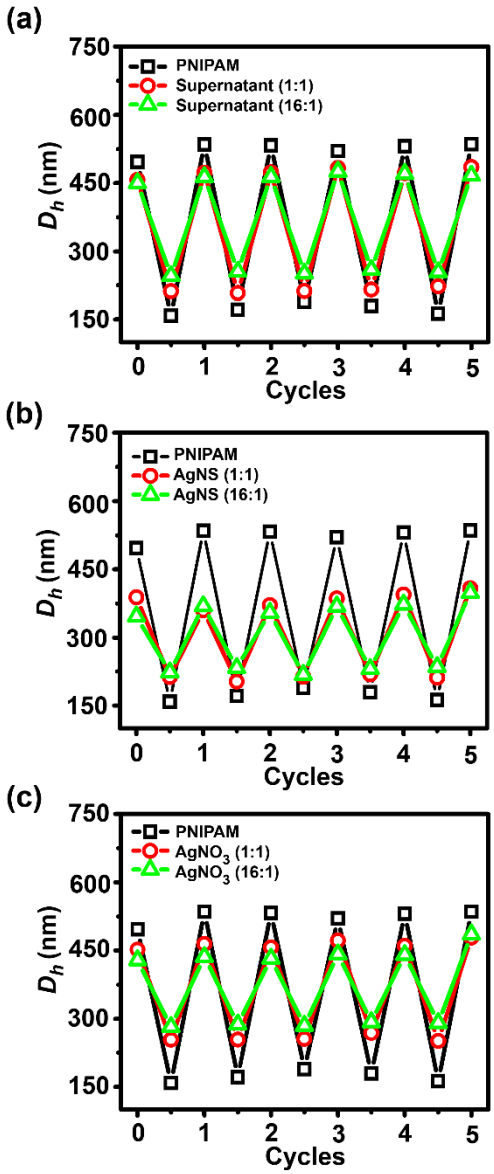

Figure S14. Thermally reversible swelling-deswelling behavior of PNIPAM in presence of (a) supernatant of the silver nanoprism solution, (b) Ag nanospheres (AgNS, 60 nm, Tedpella, Inc.), and (c) 0.2 mM precursor $AgNO_3$ solution, used for nanoprism synthesis. All these reagents were mixed with PNIPAM microgels in 1:1 and 16:1 volume ratios and each of these solutions were thermally cycled between 25 °C and 50 °C for five times. The hydrodynamic diameter and deswelling ratio of PNIPAM are changed in presence of AgNS and $AgNO_3$ because they are able to crosslink the PNIPAM microgels and thus, modify their hydrophobicity/hydrophilicity behavior.[1,2,10]

Supplementary References

(1) Liu, Y. Y.; Liu, X. Y.; Yang, J. M.; Lin, D. L.; Chen, X.; Zha, L. S. Investigation of Ag nanoparticles loading temperature responsive hybrid microgels and their temperature controlled catalytic activity. *Colloids Surf. A -Physicochemical and Engineering Aspects* **2012**, *393*, 105-110.

(2) Pich, A.; Karak, A.; Lu, Y.; Ghosh, A. K.; Adler, H. J. P. Preparation of hybrid microgels functionalized by silver nanoparticles. *Macromol. Rapid Commun.* **2006**, *27*, 344-350.

(3) Ye, J.; Hou, Y.; Zhang, G. Z.; Wu, C. Temperature-induced aggregation of poly(N-isopropylacrylamide)-stabilizecd CdS quantum dots in water. *Langmuir* **2008**, *24*, 2727-2731.

(4) Zhang, Z. Y.; Maji, S.; Antunes, A. B. D.; De Rycke, R.; Zhang, Q. L.; Hoogenboom, R.; De Geest, B. G. Salt Plays a Pivotal Role in the Temperature-Responsive Aggregation and Layer-by-Layer Assembly of Polymer-Decorated Gold Nanoparticles. *Chem. Mater.* **2013**, *25*, 4297-4303.

(5) Jones, S. T.; Walsh-Korb, Z.; Barrow, S. J.; Henderson, S. L.; del Barrio, J.; Scherman, O. A. The Importance of Excess Poly(N-isopropylacrylamide) for the Aggregation of Poly(N-isopropylacrylamide)-Coated Gold Nanoparticles. *ACS Nano* **2016**, *10*, 3158-3165.

(6) Won, S.; Phillips, D. J.; Walker, M.; Gibson, M. I. Co-operative transitions of responsive-polymer coated gold nanoparticles; precision tuning and direct evidence for co-operative aggregation. *J. Mater. Chem. B* **2016**, *4*, 5673-5682.

(7) Zhu, M. Q.; Wang, L. Q.; Exarhos, G. J.; Li, A. D. Q. Thermosensitive gold nanoparticles. *J. Am. Chem. Soc.* **2004**, *126*, 2656-2657.

(8) Gibson, M. I.; O'Reilly, R. K. To aggregate, or not to aggregate? considerations in the design and application of polymeric thermally-responsive nanoparticles. *Chem. Soc. Rev.* **2013**, *42*, 7204-7213.

(9) Ding, Y. W.; Ye, X. D.; Zhang, G. Z. Microcalorimetric investigation on aggregation and dissolution of poly(N-isopropylacrylamide) chains in water. *Macromolecules* **2005**, *38*, 904-908.

(10) Farooqi, Z. H.; Siddiq, M. Temperature-Responsive Poly(N-Isopropylacrylamide-Acrylamide-Phenylboronic Acid) Microgels for Stabilization of Silver Nanoparticles. *J. Dispersion Sci. Technol.* **2015**, *36*, 423-429.

SOUMYADYUTI (SOUMYA) SAMAI

3801 Brooklyn Ave NE
Stevens Court L 410 A
Seattle, WA 98105

979-587-2945
soumyadyutis@gmail.com
www.linkedin.com/in/soumyadyutisamai/

Education

Doctor of Philosophy in Chemistry *Sept 2013–Dec 2017*
University of Washington, Seattle, GPA: 3.88/4

Master of Science, Honors in Chemistry *2011 – 2013*
Indian Institute of Technology (IIT) Kanpur, GPA: 9.8/10

Bachelor of Science, Honors in Chemistry *2008 – 2011*
Presidency College, Kolkata, University of Calcutta

Research Experiences

- **Research Assistant** *2013 – 2017*

Department of Chemistry, University of Washington
Supervisor: David S. Ginger
Thesis: Assembly and Optical Characterization of Reversibly Reconfigurable Plasmonic Nanomaterials

- **Research Assistant** *2012 – 2013*

Department of Chemistry, IIT Kanpur
Supervisor: Nisanth N. Nair
Thesis: Developing effective strategies to inhibit antibiotic resistance of class C β-Lactamase enzymes using computational chemistry

- **Summer Research Fellowships**

Dept. of Structure, Property and Modelization of Solids, Ecole Centrale Paris *2012*
Project: Non-photochemical laser induced nucleation technique on a pharmaceutical molecule (Carbamazepine) under various conditions

Indian Institute of Scientific Education and Research(IISER), Mohali *2011*
- Project: Investigation on protein aggregation kinetics using steady state fluorescence spectroscopy and circular dichroism

Laboratory and Technical Skills

- **Analytical:** Scanning Electron Microscopy (SEM), Dark field optical microscopy and spectroscopy, FTIR, UV-Vis-NIR, and fluorescence spectroscopy, dynamic light scattering (DLS, zeta-sizer)
- **Synthesis:** Synthesis of thermo-responsive polymer microgels, silver and gold nanoparticles of different shapes and sizes, and designing their nanocomposites

Teaching Experience

Teaching Assistant *2013 – 2017*
Department of Chemistry, University of Washington
- Experienced teaching assistant in 100 level series of general and advanced honors chemistry laboratory courses
- Proficient in instructing undergraduate students in synthetic inorganic and organic chemistry laboratories
- Experienced with supervising undergraduate students in 400 level advanced physical chemistry courses and laboratory classes
- Guided undergraduate students in learning proper chemical laboratory techniques, instrumentation and laboratory safety protocols
- Facilitated and designed materials for classroom discussion sections in freshmen to senior level chemistry classes for 40-50 undergraduate students

Outreach Experience

Special Exhibit Volunteer, Pacific Science Center, Seattle *Feb 2016–Nov 2016*

- Interacted with diverse audiences to motivate STEM education
- Provided assistance to the guests to explore the cutting-edge digital and analog interactive experiences offered at the Science Center

Clean Energy Ambassador, University of Washington *Apr 2014–Dec 2017*

- Participated in hands-on activities in several outreach events to promote research on nanoscience and renewable energy

Mentoring Experience

- Supervised research-undergraduate students in synthesizing DNA-nanoparticle conjugates and studying them with optical microscopy and spectroscopy
- Guided the student to use excel-spreadsheets and other software for data analysis
- Assisted with writing project reports, presentations and building good science communication skills

Awards and Academic Highlights

- Alma-mater Travel Award 2016, Department of Chemistry, University of Washington
- Ranked 1st in the Joint Admission Test (JAM) 2011, a national entrance examination for Master's program in Chemistry in Indian Institute of Technology
- Academic Excellence Award 2011 and 2012, Department of Chemistry, IIT Kanpur
- Summer Undergraduate Research Grant for Excellence (SURGE) fellowship 2012, IIT Kanpur
- Summer Research Fellowship 2011 from Indian Academy of Sciences, Bangalore
- The INSPIRE Scholarship from the Department of Science and Technology, Government of India, 2008-2011

Publications

1. **Samai S**., Qian Z., Ling J., Guye K. N., Ginger D. S. Optical Properties of Reconfigurable Polymer/Silver Nanoprism Composites: Tunable Color and High NIR Scattering Contrast. (*manuscript submitted*)
2. **Samai S**, Choi T. L. C, Guye K. N., Yan Y., Ginger D. S. Plasmonic Nanoparticle Dimers with Reversibly Photoswitchable Interparticle Distances Linked by DNA. (*manuscript submitted*)
3. **Samai S**., Bradley D. J., Choi T. L. C., Yan Y., Ginger D. S. Temperature Dependence of Photoisomerization Quantum Yield for Azobenzene-modified DNA. *J. Phys. Chem. C* **2017**, *121*, 6997–7004, DOI: 10.1021/acs.jpcc.6b12241
4. Zhang J., Yan Y., **Samai S**., Ginger D. S. Dynamic Melting Properties of Photoswitch-Modified DNA: Shearing vs. Unzipping. *J. Phys. Chem. B*, **2016**, *120*, 10706–10713, DOI: 10.1021/acs.jpcb.6b08297.
5. Kingsland A., **Samai S**., Yan Y., Ginger D.S., Maibaum L. Local Density Fluctuations Predict Photoisomerization Quantum Yield of Azobenzene-Modified DNA. *J. Phys. Chem. Lett.* **2016**, 7, 3027−3031, DOI: 10.1021/acs.jpclett.6b00956
6. Yan Y., **Samai S**., Bischoff K. L., Zhang J., Ginger D. S., Photocontrolled DNA Hybridization Stringency with Fluorescence Detection in Heterogeneous Assays. *ACS Sens*. **2016**, 1, 566−571, DOI:10.1021/acssensors.5b00233 ***(Selected as the journal cover for the May 2016 issue)***
7. Bhattacharya M., Jain N., Dogra P., **Samai S.** and Mukhopadhyay S., Nanoscopic Amyloid Pores Formed via Stepwise Protein Assembly. *J. Phys. Chem. Lett.* 2013, 4, 480-485. http://dx.doi.org/10.1021/jz3019